

UNIVERSITE PARIS DIDEROT (PARIS 7)
ECOLE DOCTORALE : PARTICULES, NOYAUX,
COSMOS (517)

THESE DE DOCTORAT
EN
PHYSIQUE NUCLEAIRE

KEVIN FRAVAL

Measurement and analysis of the $^{241}\text{Am}(n,\gamma)$ cross section
at the CERN n_TOF facility.

Soutenue le 16/09/2013

JURY

Pr. Philippe SCHWEMLING

Pr. Philippe DESSAGNE, Rapporteur

Dr. Olivier SEROT, Rapporteur

Dr. Peter SCHILLEBEECKX

Pr. Jon BILLOWES

Dr. Frank GUNSING, Directeur de thèse

Remerciements

Alors que l'écriture de ce manuscrit touche (oh joie) à sa fin, je sors la tête des tableaux, figures, légendes, taille des axes et autres profondeurs scientifiques pour me pencher sur ceux et celles qui ont leur part de responsabilité dans cette oeuvre majeure de la science moderne. La politique étant incontestablement un de mes points forts, je m'excuse par avance si quelqu'un se vexe d'apparaître en n-ième position de cette longue liste de remerciements, alors que, clairement, son implication méritait le n-2. Etant donné que ce chapitre est le seul qui sera intensivement lu par un large public, il est majoritairement en français, et d'un style pas toujours impeccablement amphigourique.

Merci à mes parents et à ma grand-mère, dont l'implication s'étend bien plus loin que les trois années de thèse. Ce manuscrit est en quelque sorte l'aboutissement d'une route que vous n'avez ni forcée, ni tacitement préférée à une autre (j'espère quand même que vous m'auriez empêché de faire une business school...), et après tout, les parties d'échecs avec Papa ou les rédactions avec Maman ont, je crois, fait de moi un privilégié, ce dont je suis très conscient aujourd'hui.

Merci à Frank, mon directeur, qui a fait preuve de qualités insoupçonnées chez un scientifique, notamment une patience et une décontraction à TOUTE épreuve, qui m'ont permis d'être un étudiant libre (et donc heureux) de faire les choses que je voulais, quand je voulais. Je n'ai vraiment pas ressenti le stress, ni le rythme ridicule généralement associés à la thèse (et joyeusement contés par les anciens), et il me semble qu'au delà de mes compétences exceptionnelles, c'est plutôt un luxe dû en parti à tes talents d'encadrant. J'ai vraiment apprécié de pouvoir être (parfois longtemps) en désaccord avec tes explications, et prendre le temps d'y réfléchir par moi-même. Même si c'est souvent toi qui avais raison (...), je ne me serais jamais accommodé d'accepter bêtement des choses qui ont pris des décennies aux meilleurs scientifiques de l'Histoire, juste parce que d'autres font effectivement illusion de compréhension.

Merci à Simon, sans qui j'aurais probablement sombré dans les abysses de la violence irrationnelle. La perspective de discuter un peu de Futurama ou de guitare au bureau avec toi m'a vraiment aidé à me lever plus d'une fois. J'espère que la sainte Science ne t'avalera pas complètement ces prochaines années, parce que j'ai prévu le Stade de France en 2018 pour notre groupe. Je savais pas trop comment te l'annoncer, voilà.

Tant qu'on est au labo, merci à Thomas et Alexandre, qui, chacun à leur manière (!), m'ont permis de garder le sens des réalités. Thomas, parce qu'il est un peu l'homme furieux et intègre qu'on aimerait voir plus souvent, et Alexandre parce qu'il n'a pas perdu sa curiosité et son enthousiasme (ce qui arrive en général avant la fin du premier chapitre). A ces égards, vous êtes assez uniques, il faudrait trouver un obscur mélange des deux... Merci également à Angelo, non pas pour l'aide théorique à mon travail, mais pour m'avoir fait découvrir les Thermals.

Merci à Laurence, à qui je dois vraiment d'avoir grandi un peu pendant ces trois ans. J'aurais pu directement associer Laurence et le Motel¹, mais ce sont deux entités distinctes, il faut le rappeler². Je ne sais pas si les autres scientifiques qui lisent ceci se rendent compte à quel point c'est important d'avoir un(e) ami(e) qui soit animé(e) par autre chose, et de partager un peu cela avec lui/elle. Ça change TOUT. Dans la même catégorie, merci à Anna, Stéphanie et Marie, sans qui je serais sûrement encore un peu plus bête aujourd'hui, même si je ne suis pas censé l'admettre.

Merci à l'équipe du lycée: Adrien, pour nos débats métaphysico-videoludico-musicaux au Pantalon³, Sylvain, le seul joueur décent de Top Spin de toute l'Ile de France, Alex, ~~pour les pichets de Pina Colada au Bar à Nenettes~~ qui est maintenant marié et papa donc qui a une vie saine et respectable... Merci également à Camille, Alix, Olga, et Olivier, pour nous avoir adoptés sans protester! Et bien sûr Nico, La Tuile, Camiye, Sandra, et Caro, même si tout ça ne nous rajeunit pas vraiment...

Merci à Clément, Pierre et Barbara qui ont su m'apporter un peu de l'esprit de Grenoble⁴.

Merci à Florian et Benjamin, pour avoir guidé mon âme lors du mariage dudit Benjamin, grâce à qui je sais maintenant que les scouts sont des gens sympas, qui ne dévorent pas les âmes.

Merci à Marine et Sophie pour les excellentes soirées chez vous, notamment Sophie pour avoir redéfini le mot "hipster" pour moi.

Mark, Chris, Toby, Carlos, Esther, sorry if you read that far and felt a little abandoned, no way I could forget to mention you as well! Thanks for the great non-scientific moments we've had, I'm sure the n_TOF meetings would have reached their ultimate goal⁵ had you not been part of the group.

Merci enfin à Cédric, car l'accent belge est plus fort que le shift de 8 heures au CERN, Sandra pour avoir également si gentiment rompu ma solitude au CERN, Béryl pour le café improbable à New York, et tant qu'on y est, merci aux Thermals de m'avoir fait découvrir la guitare pour les nuls.

¹le Motel est un bar.

²Merci donc, également, au Motel.

³et au Piano Vache. N'oublions pas le Piano Vache.

⁴La bière.

⁵Lethal boredom.

Tous ces petits détails totalement non scientifiques ont contribué à l'élaboration de ce manuscrit, qui peut enfin commencer.

-With your help, our scientists are limited only
by their *imagination*.
-And by their *consciences*, surely?
-Let's hope so.

Alan Moore, *Watchmen*.

Contents

1	Introduction	11
1.1	Nuclear technology and radioactive waste	11
1.1.1	History of nuclear technology	11
1.1.2	Functioning of nuclear reactors	12
1.1.3	Nuclear reactions and the production of waste	15
1.2	The impact of actinides and ^{241}Am in the spent fuel	16
1.3	Nuclear data on ^{241}Am	17
1.3.1	Cross sections and resonances	17
1.3.2	Past experiments and status of evaluations	19
2	Theoretical aspects	21
2.1	Resonant or non resonant reactions	21
2.1.1	Potential scattering	22
2.1.2	Resonant reactions: the compound nucleus model	27
2.2	Continuum coupling formalism	28
2.2.1	From the full wave function to the transition amplitude	29
2.2.2	From projection operators to resonances	30
2.3	The R-matrix theory of nuclear reactions	34
2.3.1	Principles of the R-matrix theory	34
2.3.2	The R matrix theory	34
2.3.3	The level matrix formulation	40
2.3.4	Treatment of photon channels	41
2.4	Statistical aspects of the compound nucleus	43
2.4.1	The Porter Thomas distribution	43
2.4.2	The Wigner surmise	45
3	The experimental facility	47
3.1	History of the n_TOF project	47
3.2	The PS proton beam	48
3.3	The spallation target	49
3.4	The tunnel	50
3.5	The experimental area	52

3.5.1	The MicroMegas detectors	52
3.5.2	The silicon monitors (SiMON)	52
3.5.3	The C ₆ D ₆ detectors	52
3.5.4	The TAC	54
3.6	The characteristics of the facility	54
3.6.1	The time of flight technique	54
3.6.2	Data acquisition	56
3.6.3	Extracting the capture yield	56
3.6.4	The neutron energy resolution	57
3.6.5	Multiple scattering	58
4	The analysis	61
4.1	Experimental setup	61
4.2	Sample characteristics	62
4.3	Run selection	64
4.4	Data taken	66
4.5	The weighting function procedure	66
4.6	Amplitude-energy calibration	69
4.7	Event selection and processing	74
4.8	The time-energy calibration	77
4.9	Observations concerning parasitic and dedicated pulses	78
4.9.1	Count rates for both types of pulses	78
4.9.2	Computing the difference	79
4.10	Background components	80
4.10.1	The sample's activity	80
4.10.2	The aluminium canning	81
4.10.3	The Al ₂ O ₃ matrix	82
4.10.4	The neutron filters	83
4.10.5	Final evaluated background	84
4.11	Normalization	86
4.12	Neutron flux	87
4.13	Capture yield	87
5	Results	91
5.1	The R-matrix code SAMMY	91
5.2	The thermal cross section	91
5.3	The resolved resonance region (RRR)	96
5.4	Statistical analysis	107
5.5	The unresolved resonance region (URR)	110
6	Summary and concluding remarks	115

Chapter 1

Introduction

This first chapter will be aimed at providing necessary notions about nuclear reactors, nuclear waste production, and nuclear reactions that are needed to understand the motivation for this work. More specifically, the case of ^{241}Am will be detailed, with its impact on the radio-toxicity of the spent fuel, together with the current status of the nuclear data on this isotope.

1.1 Nuclear technology and radioactive waste

1.1.1 History of nuclear technology

The discovery of the neutron

After the discovery of the atomic nucleus in 1910 by Ernest Rutherford [1], the fundamental particles used to describe matter are essentially the electron, the proton, and the α particle, which has no known structure at this time. Therefore the structure of, say, ^{13}C is three α particles plus a proton and an electron. Nuclear physicists have worked with this picture of the nucleus until 1932, when James Chadwick, starting with earlier observations made by Irene Joliot-Curie, assumes the existence of an unknown particle emitted when α particles collide ^9Be or ^{10}B [2]. Using a rigorous analysis of the data, he must conclude that this new particle has to be neutral, and possess a mass similar to the one of the proton. He calls it the neutron, and gets the Nobel prize in 1935. Right after this striking discovery, many nuclear physics groups in the world start to bombard every available nucleus with neutrons. In 1936, the first neutron resonances are observed [3], and in 1938, nuclear fission is discovered by the joint work of Otto Hahn, Lise Meitner, Fritz Strassmann and Otto Frisch [4, 5].

The Manhattan project

Shortly after, in early August 1939, as Germany prepares the invasion of Poland, Albert Einstein addresses a letter to the United States president Franklin D. Roosevelt [6] to inform him "that it may become possible to set up a nuclear chain reaction in a large mass of uranium, by which vast amounts of power and large quantities of new radium-like elements would be generated", and "that extremely powerful bombs of a new type may thus be constructed". Einstein's recommendations include "securing a supply of uranium ore for the United States" and "to speed up the experimental work" because "in Berlin [...] some of the American work on uranium is now being repeated". Following these recommendations, the Manhattan project starts in 1942, with the primary objective of building a nuclear bomb using a diverging fission chain reaction. One of the designs for the first nuclear bombs was based on the use of ^{239}Pu , which can only be significantly accumulated by neutron irradiation of ^{238}U . To that end, the very first nuclear reactor, the Chicago Pile-1, was built in Chicago under the supervision of Enrico Fermi [7], and sustained the first nuclear fission chain reaction on December, 2nd, 1942. On July, 16th, 1945, the first nuclear device exploded on the Trinity site [8], in New Mexico, using the plutonium accumulated by Chicago Pile-1. On August, 6th and 9th, 1945, the United States dropped nuclear bombs on the cities of Hiroshima and Nagasaki.

The birth of nuclear power plants

The first nuclear reactor to provide electricity for a power grid was started in 1954 in Obninsk, USSR [9]. Also, the first commercial power plant was started in Windscale, England, in 1956 [10]. Although the economic situation before the 1970s' made nuclear power unattractive and its development slow, the oil crisis of 1973 renewed the interest of Japan and western countries in nuclear energy, despite the growth of popular anti-nuclear movements [11].

1.1.2 Functioning of nuclear reactors

Sustaining the fission chain reaction

Nuclear fission occurs in heavy nuclei when the Coulomb repulsion between protons is larger than the binding energy provided by the strong force. The result is a split of the initial nucleus into two fragments (see figure 1.1), each carrying a significant amount of energy (in the form of kinetic and internal excitation). In the case of a nuclear reactor, the required energy to go above the so-called potential fission barrier is brought by an external neutron, which brings his binding and kinetic energies when it is absorbed by the nucleus. For example, the binding energy of a neutron in ^{236}U (which is the compound nucleus $^{235}\text{U}+n$) is 6.545 MeV,

and fission can be induced on ^{235}U using thermal neutrons, *i.e.* neutrons having the kinetic energy of thermal equilibrium, which is 25.3 meV at 300 K.

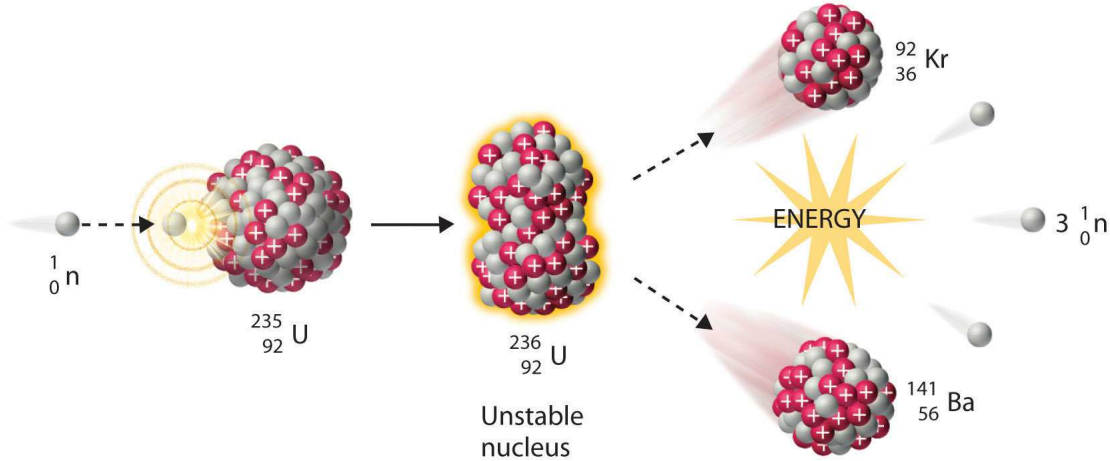


Figure 1.1: A typical example of fission of ^{235}U [12].

Not all heavy nuclei can undergo fission with thermal neutrons, typically the actinides with an odd number of neutrons (like ^{235}U with 92 protons and 143 neutrons) are called fissile isotopes, meaning that the absorption of a thermal neutron will trigger a fission reaction with a large probability. Other heavy nuclei can undergo fission as well, but the missing energy to overcome the fission barrier must be brought in the form of kinetic energy in the collision. One of the major characteristics of the fission reaction is that it usually emits several neutrons (2.4 neutrons on average in the case of ^{235}U), which can in turn induce fission reactions, thus opening the possibility of a self-sustaining process. In the case of a reactor functioning with fissile ^{235}U , two crucial conditions have to be met. First, the neutrons emitted during fission must change their kinetic energy from typically 2 MeV when emitted to the thermal equilibrium, in order to maximize the probability of inducing another fission. Second, one fission reaction must trigger only one subsequent fission. This reproduction factor is usually labeled k , and is the number of fission reactions induced by one initial fission reaction. If k is greater than one, the chain reaction will exponentially diverge, leading to the rapid accumulation of heat, and possibly melting of the reactor core. If k is lower than one, however, the chain reaction will exponentially stop. This points out the need of keeping the value of k oscillating around one for the reactor to function. In a typical Pressurized Water Reactor (PWR), the neutron moderation, *i.e.* slowing down from about 2 MeV to thermal energy is ensured by the presence of pressurized water around the fuel rods. Elastic scattering reactions slowly get the neutrons to thermal equilibrium, and an adjustable concentration of ^{10}B in the water helps controlling the neutron density, hence the value of k . Indeed ^{10}B has a very large neutron capture cross

section (related to the reaction probability, see section 2.1.1 for a rigorous definition of a reaction cross section), thus increasing the boron concentration in the water moderator can help decrease the neutron density in the reactor, and stop the chain reaction if necessary.

Also, it is necessary to have a negative temperature coefficient of reactivity. The reactivity ρ of a reactor is defined by:

$$\rho = \frac{k - 1}{k} \quad (1.1)$$

and the temperature coefficient of reactivity α is the derivative of ρ with respect to temperature:

$$\alpha = \frac{\partial \rho}{\partial T} \quad (1.2)$$

If α is positive, an increase in temperature, caused by an increase of the fission rate, will induce an increase in reactivity (hence an increase of k and the fission rate). This is not a safe functioning condition, since it favors the divergence of the reactor. Current reactors are designed to compulsorily have a clearly negative α coefficient.

One very important final aspect of neutron kinetics in a reactor is the presence of delayed neutrons. They are neutrons emitted a very long time (typically seconds or minutes) after the fission has occurred, because they follow a β^- decay of one of the fission fragments. Although they account for about only 0.7% of the total number of neutrons in a typical PWR reactor, their time of emission is so large that it increases the average time of neutron emission, and thus slows down the increase of k .

From nuclear fission to electricity

The energy available in a nuclear reactor comes from the fission's so-called Q -value, which is the difference in energy between the initial state ($^{235}\text{U}+n$) and the final state (the fission fragments). The Q -value of ^{235}U fission is about 200 MeV, and the majority of this energy is carried by the kinetic energy of the fission fragments. These very energetic nuclei will brutally slow down in the surrounding materials (the fuel rods), and this fast deceleration will induce an increase in temperature. In PWR reactors, the water moderator also acts as a coolant. This primary water circuit transports the heat into a steam generator connected to a secondary water circuit. The steam then feeds a turbine that will convert the mechanical energy of the rotating turbine into electrical energy via magnetic induction. Figure 1.2 shows a schematic view of a PWR reactor.

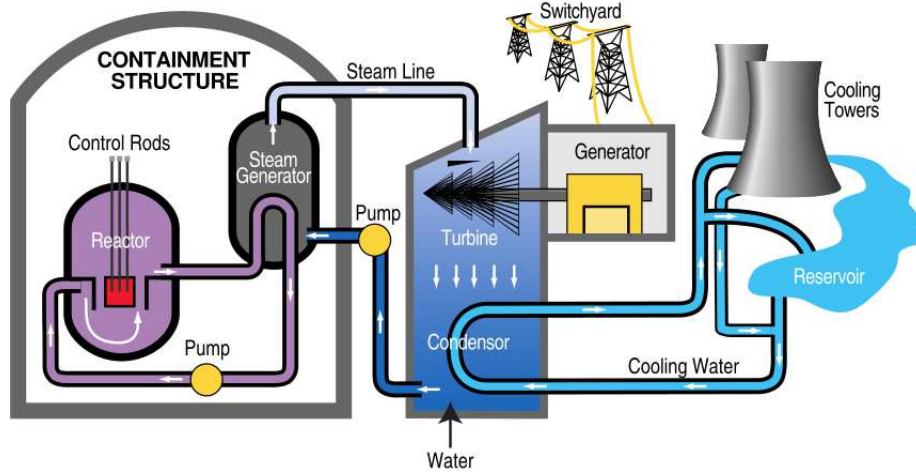


Figure 1.2: A schematic view of a PWR reactor[13].

1.1.3 Nuclear reactions and the production of waste

In a nuclear reactor, neutron induced fission on ^{235}U is not the only nuclear reaction occurring. Four nuclear reactions can be associated with waste production: elastic and inelastic scattering, radiative capture, and fission. Elastic scattering will be detailed from a theoretical perspective in section 2.1.1, but for now let us view it as neutrons bouncing off the very hard core of the atomic nuclei. During the process, some kinetic energy can be exchanged, and this is how neutron moderation works, especially on the protons of the pressurized water, because the energy loss is maximal when scattering on protons. When the relative kinetic energy of the pair is large enough, the target nucleus can also exit the collision in an excited state, this is called inelastic scattering. Also, neutrons can be absorbed by nuclei, which will in turn emit γ radiation to get rid of the excitation energy brought by the binding of the neutron. This process, labeled (n,γ) , is called radiative capture, and can happen on any nucleus.

When radiative capture occurs on a structural material, it generates neutron rich isotopes which are usually unstable, and undergo β^- decays:



This process is called activation, and is responsible of the creation of radioactive waste in materials composing the reactor. Also, radiative capture can occur on uranium isotopes, especially on ^{238}U which represents about 96% of the fuel content in a PWR reactor. As ^{238}U does not have as large a fission cross section as ^{235}U , neutron capture on ^{238}U will often give birth to heavier isotopes of Np, Pu, Am and Cm, by subsequent neutron captures and β^- decays. These nuclei (together with the uranium isotopes), belonging to the actinides, are categorized between major actinides, composed of U and Pu isotopes, and minor actinides, composed

of all other isotopes. Actinides are unstable and usually undergo α decay (the emission of ${}^4_2\text{He}$) as a first step to reach stability. This means that their life time is in general much larger than β^- isotopes. Indeed actinides tend to dominate the radio-toxicity of the spent fuel in the long term (see section 1.2 for more details). Finally, the fission fragments of ${}^{235}\text{U}$ are usually very neutron rich, and thus have to undergo many β^- decays to reach stability. Fission can also occur on fissile actinides, such as ${}^{239}\text{Pu}$. This is the final source of production of radioactive waste. In the end one can categorize the radioactive waste produced by a reactor in the following way:

- Activated structural materials produced by radiative capture.
- Major and minor actinides produced by radiative capture mostly on ${}^{238}\text{U}$.
- Fission products mostly produced by ${}^{235}\text{U}(\text{n},\text{f})$ and ${}^{239}\text{Pu}(\text{n},\text{f})$.

The following sections will specifically address the issue of waste in the spent fuel, namely fission products and actinides.

1.2 The impact of actinides and ${}^{241}\text{Am}$ in the spent fuel

The spent fuel of a Pressurized Water Reactor (PWR) using MOX fuel with 8.2% content of Pu, after a burn-up of 43500 MW.d/t and four years of cooling has a 0.6% mass content of minor actinides, among which 50% of ${}^{241}\text{Am}$ [14]. Am and Np isotopes are responsible for the totality of the radio-toxicity for times greater than 10^5 years [15]. For example, ${}^{241}\text{Am}$ has a half-life of 432 years, ${}^{243}\text{Am}$ a half-life of 7370 years, and ${}^{237}\text{Np}$ a half-life of 2.14×10^6 years. Also, the search for a constant increase of fuel burn-up inevitably leads to the accumulation of more minor actinides.

To this day, two main types of fuel cycles are being used. The first, called "open", for example used by the United States, is technically not a cycle, since the spent fuel is left unprocessed and stored in open-air conditions. This method reduces the proliferation issues, since no separation of fissile isotopes is being done. However from an actual waste management perspective, the closed fuel cycle, for example used in France, performs chemical separation of uranium and plutonium isotopes from the rest of the spent fuel. These major actinides are reprocessed into a Mixed Oxide (MOX) fuel which is re-injected into fresh fuel rods. Concerning the rest of the spent fuel, iodine, technetium and cesium can be chemically separated as well. The retrieved radioactive ${}^{129}\text{I}$ content is then released in the sea, where it is expected that the effect in average radio-toxicity will be minimal. The remaining fission products and minor actinides are nowadays vitrified and stored

underground.

Nevertheless, transmutation or incineration of actinides is still an open possibility, for example thermal neutron transmutation of ^{241}Am , through the path described in figure 1.3 [16, 17]. In this example, ^{242m}Am , ^{239}Pu and ^{245}Cm are long-lived fissile isotopes, and are eventually gotten rid of through thermal neutron induced fission.

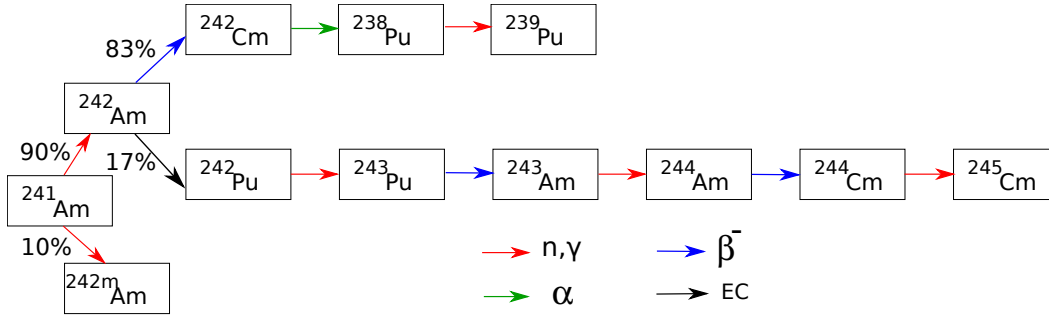


Figure 1.3: The transmutation path of ^{241}Am under thermal neutron irradiation.

1.3 Nuclear data on ^{241}Am

1.3.1 Cross sections and resonances

The interaction of a neutron in a material medium is a probabilistic process, because the uncertainty principle of quantum mechanics prevents one to think of the neutron as a particle moving towards particle-like nuclei. Section 2.1.1 gives a rigorous definition of a reaction cross section in terms of the system's wave function. However one can intuitively define a cross section by assuming the probability of reaction between positions x and $x + dx$ is proportional to dx (with a constant λ). Thus, the probability of survival of a neutron after travelling a distance $x + dx$ can be written as the product of the probability of survival after x and the probability of no reaction between x and $x + dx$:

$$P(x + dx) = P(x) \times (1 - \lambda dx) \quad (1.4)$$

$$\frac{dP}{dx} = -\lambda P(x) \quad (1.5)$$

$$P(x) = e^{-\lambda x} \quad (1.6)$$

assuming $P(0) = 1$. Then one can safely assume that the constant λ is proportional to the target nucleus density N (in m^{-3}).

$$\lambda = N \times \sigma \quad (1.7)$$

with σ being homogeneous to a surface. It is called the reaction cross section. It includes all nuclear properties of the neutron-nucleus pair. In reactor physics, λ is usually called the "macroscopic" cross section, and labeled Σ .

In 1936, the first observations of neutron cross sections showed large fluctuations with neutron kinetic energy [3]. Those peaks, called resonances, were interpreted as the presence of nuclear eigenstates. Indeed it is easily conceivable that the reaction probability between a neutron and a nucleus will be maximal if the available energy is close to the excitation energy of an eigenstate of the compound nucleus (see sections 2.3 and 2.2 for theoretical interpretations of resonant spectra). Figure 1.4 shows a typical resonant cross section of $^{238}\text{U}(n,\gamma)$.

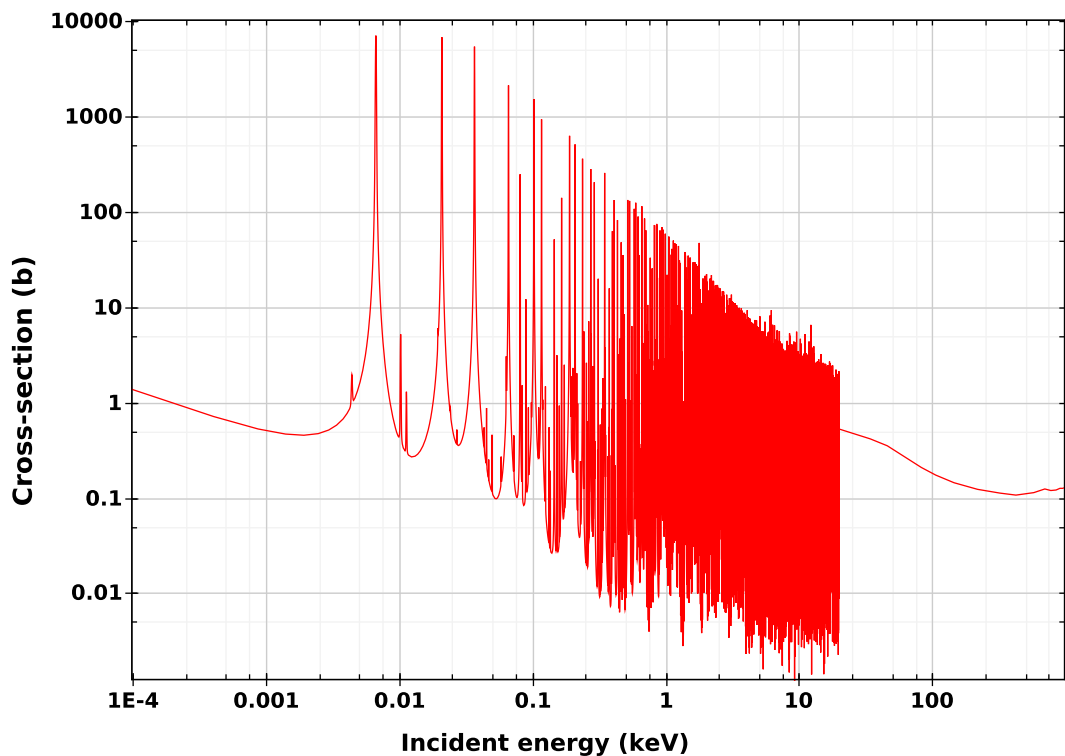


Figure 1.4: The $^{238}\text{U}(n,\gamma)$ cross section at 300 K in the ENDF-B/VII.1 evaluation [18].

The first part of the cross section shows distinct resonances, and is called the Resolved Resonance Region (RRR), whereas the high energy part cannot resolve individual levels in the spectrum and is an average cross section. It is called the Unresolved Resonance Region (URR). Experimental work regarding nuclear data is aimed at evaluating resonance parameters in the RRR, together with estimating the average cross section when the experimental resolution (together with the natural broadening of states with energy) marks the stop of the RRR.

1.3.2 Past experiments and status of evaluations

This work, as a part of the EC-FP7 ANDES project [19], is concerned with the (n,γ) reaction on ^{241}Am , which is on the High Priority List of the Nuclear Energy Agency [20, 21]. Current available experimental data on ^{241}Am neutron cross section include activation and pile oscillation measurements to retrieve the thermal capture cross section, and time-of-flight experiments which allow resonance analysis. The only measurement of the thermal cross section using pile oscillation was performed by Pomerance *et al.* in 1955 [22]. A rather large amount of data obtained by activation technique exists (one can cite the work of Bak [23], Dovbenko [24], Harbour [25], Gavrilov [26], Adamchuk [27], Belanova [28], Wisshak [29], Shinohara [30], Maidana [31], Fioni [16], Nakamura [32], Bringer [33]. Finally, Belgya [34] and Genreith [35] performed measurements using prompt gamma activation analysis, see figure 5.5). It should be noted that the activation technique requires the use of the Wescott convention, which assumes a shape for the neutron flux and energy dependence of the cross section. The presence of large resonances at very low energy in ^{241}Am complicates this analysis step, and corrections are needed. This partly explains the difficulties and discrepancies in the past measurements. Concerning time of flight measurements, the two most recent measurements are the ones of Jandel *et al.*[36] and Lampoudis *et al.*[37]. The work of Jandel was performed in Los Alamos National Laboratory, using the 4π calorimeter of BaF_2 crystals DANCE. The cross section was measured using a target containing $219\ \mu\text{g}$ of ^{241}Am at a 20.2 m distance from the neutron source. The analysis was performed from 0.02 eV to 320 keV, and included resolved resonance shape analysis from 0.02 eV to 12 eV. The work of Lampoudis was performed at the GELINA facility in Geel, Belgium. It used a 325 mg ^{241}Am content and included both transmission and capture measurements. The transmission measurement was performed at a flight path of 26.45 m and the capture experiment used two C_6D_6 detectors with a flight path of 12.5 m. The analysis was performed up to 110 eV, with resonance shape analysis. There also exists a set of transmission data from Derrien and Lucas [38], and Kalebin *et al.* [39]. Concerning evaluations, ENDF/B-VII.1 [18] adopted the resonance parameters evaluated by JENDL-4.0 [40], which took into account the work of Jandel *et al.*[36], whereas the parameters of JEFF-3.1.2 [41] are based on capture data from [42, 43]. Figure 1.5 and table 1.1 show the discrepancies between JEFF-3.1.2 [41] and ENDF/B-VII.1 [18], together with other time of flight experimental data, at low neutron energies.

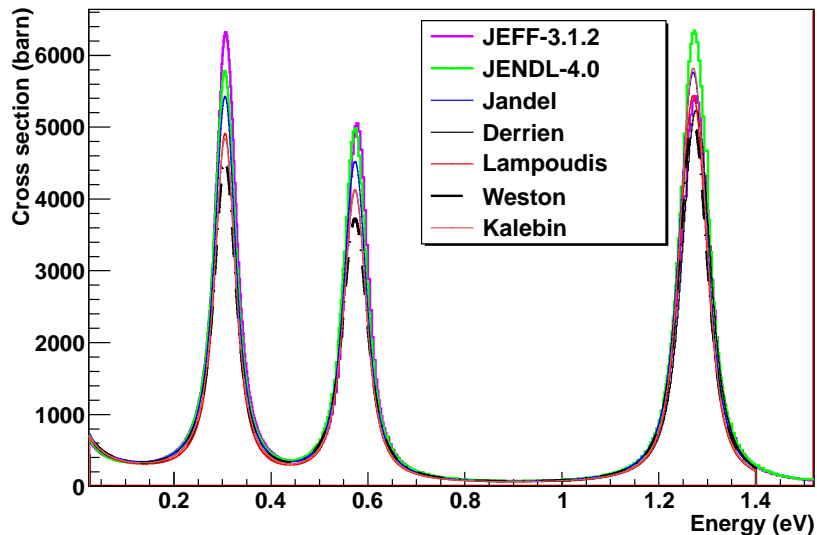


Figure 1.5: The $^{241}\text{Am}(n,\gamma)$ cross section at 300 K in the most recent evaluations and experiments.

Table 1.1: The first three resonances' parameters in previous works and evaluations.

Author	$E_n=0.306$ eV		$E_n=0.573$ eV		$E_n=1.271$ eV	
	$g\Gamma_n$ (meV)	Γ_γ (meV)	$g\Gamma_n$ (meV)	Γ_γ (meV)	$g\Gamma_n$ (meV)	Γ_γ (meV)
Weston [43]	0.027	46.9	0.047	47.3	0.157	49.2
Kalebin [39]	0.0275	45	0.0464	43	0.165	41
Derrien [38]	-	-	-	-	0.161	46.5
Jandel [36]	0.0311	44.4	0.501	43.3	0.173	45.3
Lampoudis [44]	0.0373	41.55	0.0458	42.11	0.218	41.68
JEFF-3.1.2 [41]	0.0356	43.52	0.055	40.67	0.169	48.44
JENDL-4.0 [40]	0.0329	44.4	0.0558	43.3	0.190	45.3

Chapter 2

Theoretical aspects

In this chapter will be reviewed the fundamental knowledge related to neutron physics, useful nuclear reaction formalisms and statistical characteristics of the compound nucleus. The first sections will detail the concepts of potential scattering and compound nucleus formation (resonant scattering). Then nuclear reaction models will be detailed, namely continuum coupling and the R-matrix formalism. Finally, some interesting and useful statistical properties of the compound nucleus will be detailed in section 2.4.

2.1 Resonant or non resonant reactions

Nuclear reactions are usually classified into two major groups, the compound nucleus reactions and the direct reactions. The direct reactions are generally at higher energies than what concerns this work, and include for instance transfer, knock-out reactions or inelastic scattering. The main conceptual difference from a physical point of view is the duration of the interaction. In resonant reactions, the typical times for decay channels to open are much larger than the average nuclear interaction times (*e.g.* one pion exchange with pion mass ≈ 140 MeV: $\tau \approx \frac{\hbar}{\Gamma} \approx 5 \times 10^{-24}$ s.) This means that from a nuclear point of view, a compound nuclear state has a very long life time. At low neutron energies ($E_n \leq 1$ MeV), the only reaction that doesn't involve compound nucleus formation is potential scattering. The interaction time is basically the time needed for the incoming neutron to go past the target nucleus. At 1 eV, with a nucleus of size 1 fm, this time is about $\tau \approx 7 \times 10^{-20}$ s. As will be seen in section 2.1.2, this is still much shorter than the typical life time of a resonant state. The following subsections will give the basis of potential scattering formalism (this will be needed in the R-matrix section) and compound nuclear models, leading to the Breit-Wigner formula for a single isolated resonance.

2.1.1 Potential scattering

This subsection assumes the scattering of spinless particles. For the basics of the quantum formalism or further details, the reader is referred to the standard textbook by Messiah [45], and the nuclear reaction manual by Satchler [46] among many others. First, the wave function of a system composed of two partners (like a neutron and a nucleus) can be expressed as a product of four parts:

$$\Psi = \eta(\vec{R}) \times \chi(\vec{r}) \times \epsilon_1(q_1) \times \epsilon_2(q_2) \quad (2.1)$$

where $\eta(\vec{R})$ stands for the centroid motion of the system at position \vec{R} , $\chi(\vec{r})$ stands for the relative motion in the center of mass of the two bodies with $\vec{r} = \vec{r}_1 - \vec{r}_2$, and $\epsilon_i(q_i)$ is the internal wave function of body i with internal coordinates q_i . The centroid can be ignored if assumed at rest, and the internal wave functions will not be explicitly mentioned if not precised otherwise. Only the relative motion will be of importance during the majority of the chapter.

Scattering in a spherically symmetric potential

We consider two colliding partners or reduced mass μ (they can be particles, atoms, nuclei, or anything that needs to be described as a quantum body) under the action of a *spherically symmetric* potential. Under this condition, it is especially interesting to try and solve the Schrödinger equation for a spherical wave, because it will satisfy the same symmetry as the potential. The most convenient choice is the spherical harmonics, since they form a basis of the Hilbert space, so it will always be possible *a posteriori* to expand any wave function in terms of spherical waves (this is a partial wave expansion). By construction, the spherical harmonics Y_l^m are eigen vectors of the angular momentum operator $\hat{\mathbf{L}}$. Hence:

$$\hat{\mathbf{L}}Y_l^m = mY_l^m \quad (2.2)$$

$$\hat{\mathbf{L}}^2Y_l^m = l(l+1)Y_l^m \quad (2.3)$$

In the situation where the potential only depends on the spherical variable r , the wave function of the relative motion of the system Φ_l can be separated:

$$\Phi_l(r, \theta, \phi) = R_l(r)Y_l^m(\theta, \phi) \quad (2.4)$$

With this representation, the wave function Φ_l carries l units of angular momentum, with projection m along the quantization axis. If one writes the Schrödinger equation in spherical coordinates for the wave function $\Phi_l(r, \theta, \phi)$, the angular components vanish, and it is possible to derive the radial Schrödinger equation satisfied by the radial wave function $u(r) = r \times R(r)$:

$$-\frac{\hbar^2}{2\mu} \left(\frac{d^2u(r)}{dr^2} - \frac{l(l+1)}{r^2}u_l(r) \right) + V(r)u_l(r) = Eu_l(r) \quad (2.5)$$

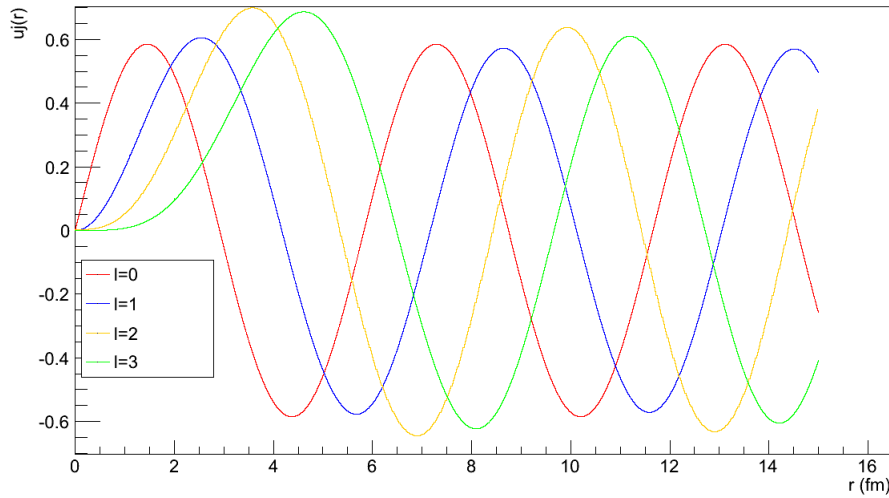


Figure 2.1: Radial wave functions for $V=0$ from $l=0$ to $l=3$, and $E=1$ MeV.

Equation 2.5 is a Schrödinger equation with a modified potential $V_{eff}(r) = V(r) + \frac{\hbar^2 l(l+1)}{2\mu r^2}$. The second term in the potential is called the centrifugal barrier potential. It merely expresses the fact that a large orbital momentum will generate centrifugal force and therefore a repulsion between the two partners of the collision. This is the main argument why the reaction probability with a large angular momentum (practically $l \geq 1$) at low neutron energy is reduced.

For the following it is rather convenient to define $k = \sqrt{\frac{2\mu E}{\hbar^2}}$. In the very important case of $V(r)=0$, the solutions for $u_l(r)$ are:

$$u_l(r) = \rho j_l(\rho) \quad (2.6)$$

with $\rho = kr$ and j_l being the spherical Bessel function of order l (table 2.1).

Spherical Bessel functions	
l	$j_l(\rho)$
0	$\frac{\sin(\rho)}{\rho}$
1	$\frac{\sin(\rho)}{\rho^2} - \frac{\cos(\rho)}{\rho}$
2	$\left(\frac{3}{\rho^2} - 1\right) \frac{\sin(\rho)}{\rho} - \frac{3\cos(\rho)}{\rho^2}$
3	$\left(\frac{15}{\rho^3} - \frac{6}{\rho}\right) \frac{\sin(\rho)}{\rho} - \left(\frac{15}{\rho^2} - 1\right) \frac{\cos(\rho)}{\rho}$

Table 2.1: Spherical Bessel functions.

For solving a practical problem, however, V is not zero in the whole range. The potential used to model the nuclear force has to be short ranged, with a smooth

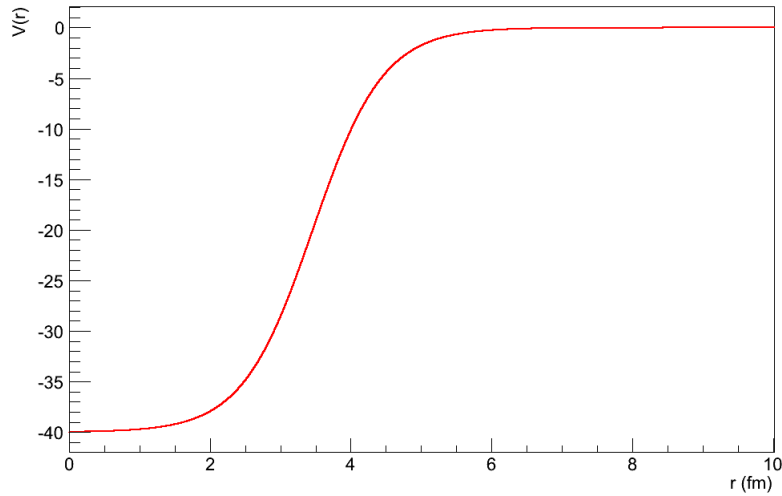


Figure 2.2: The Woods-Saxon potential $V_0=-40$ MeV and $a=0.5$.

transition between a flat deep well and a quickly vanishing part after a certain radius r_0 . One very commonly used parametrization is the Woods-Saxon potential:

$$V(r) = \frac{V_0}{1 + \exp(\frac{r-r_0}{a})} \quad (2.7)$$

with a being the diffuseness of the potential, and V_0 the depth. For a typical nucleus, $V_0 = -40$ MeV and $a=0.5$.

There is no analytical solution for equation 2.5 with a Woods-Saxon potential, but one can solve the problem numerically, see figure 2.3. For this calculation, the reduced nuclear mass was $A=24$, and $r_0=1.2 \times A^{1/3}$ fm.

From the wave function to the cross section

On the other hand, the scattering process can be represented at large distances by an incoming plane wave and a scattered spherical wave.

$$\Psi(\vec{r}) \rightarrow e^{i\vec{k}\vec{r}} + \frac{f(\theta)}{r} e^{ikr} \quad (2.8)$$

with θ being the angle between the incident beam and the scattered particle, and $f(\theta)$ the scattering amplitude. The differential cross section is then defined by the square modulus of the transition amplitude:

$$\frac{d\sigma}{d\Omega} = |f(\theta)|^2 \quad (2.9)$$

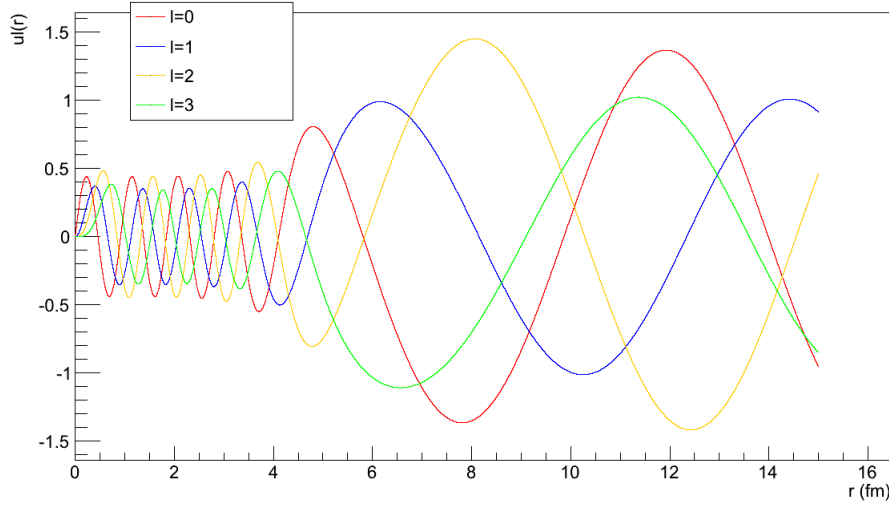


Figure 2.3: Radial wave functions at $E=1$ MeV, for $V_0=-40$ MeV and $a=0.5$.

The next step is to connect the picture of equation 2.8 with a plane wave expansion into spherical waves. Let us define radial *incoming* and *outgoing* wave functions I_l and O_l , that represent a particular set of solutions for the radial Schrödinger equation. In terms of the regular and irregular Coulomb functions F_l and G_l :

$$I_l = G_l - iF_l \quad (2.10)$$

$$= O_l^* \quad (2.11)$$

$$O_l = G_l + iF_l \quad (2.12)$$

When there is no Coulomb field, $F_l(kr) = kr \times j_l(kr)$ and $G_l(kr) = -kr \times n_l(kr)$, with n_l being the Neumann function of order l . If there is no scattering, the wave function is simply:

$$u_l(r) = kr j_l(kr) = \frac{i}{2} (I_l(r) - O_l(r)) \quad (2.13)$$

However when $V \neq 0$, one can introduce the collision (or scattering) matrix element U_l that will affect the outgoing wave function:

$$u_l(r) = \frac{i}{2} (I_l(r) - U_l O_l(r)) \quad (2.14)$$

On the other hand, the total incoming and outgoing wave functions \mathcal{I}_l and \mathcal{O}_l can be expressed just like in equation 2.4:

$$\mathcal{I}_l = \frac{1}{v_l^{1/2}} i^l Y_l^m \frac{I_l}{r} \quad (2.15)$$

$$\mathcal{O}_l = \frac{1}{v_l^{1/2}} i^l Y_l^m \frac{O_l}{r} \quad (2.16)$$

Here the i^l term is for convenience, as it respects the time reversal symmetry for spherical harmonics, and it will be convenient to cancel another i^l term in the spherical waves expansion. Also, a flux normalization $\frac{1}{v_l^{1/2}}$ has been introduced, where v_l stands for the relative speed of the two colliding partners with relative angular momentum l . This term is used as a normalization of the continuum wave function. As it is not a discrete state that is bound in space, the choice for normalization is the flux has to be equal to unity. As the cross section can be expressed as a ratio of fluxes, this normalization will cancel in the observable. Let us now simplify the problem by assuming that the quantization axis is along the propagation axis, so that $m = 0$. Then a very useful identity is to be used: $Y_l^0 = \sqrt{\frac{2l+1}{4\pi}} P_l(\cos \theta)$, with P_l being the Legendre polynomial. The total wave functions now become:

$$\mathcal{I}_l = \frac{1}{v_l^{1/2}} i^l \frac{(2l+1)^{1/2}}{2\pi^{1/2}} P_l(\cos \theta) \frac{I_l}{r} \quad (2.17)$$

$$\mathcal{O}_l = \frac{1}{v_l^{1/2}} i^l \frac{(2l+1)^{1/2}}{2\pi^{1/2}} P_l(\cos \theta) \frac{O_l}{r} \quad (2.18)$$

Therefore the radial wave function 2.14 can be expressed in terms of the total wave functions:

$$u_l(r) = \frac{i}{2} (I_l(r) - U_l O_l(r)) \quad (2.19)$$

$$= \frac{i}{2} \frac{2\pi^{1/2} r}{i^l (2l+1)^{1/2} P_l(\cos \theta)} (\mathcal{I}_l - U_l \mathcal{O}_l) \quad (2.20)$$

This expression can be substituted in a spherical wave expansion of the total wave function Ψ :

$$\Psi = \frac{1}{kr} \sum_{l=0}^{\infty} (2l+1) i^l P_l(\cos \theta) u_l(r) \quad (2.21)$$

$$= \frac{i}{2} k^{-1} 2\pi^{1/2} \sum_{l=0}^{\infty} (2l+1)^{1/2} (\mathcal{I}_l - U_l \mathcal{O}_l) \quad (2.22)$$

This particular form for Ψ is to be identified to equation 2.8. When doing so (a common strategy is to add and subtract a plane wave expressed as a spherical wave expansion), the total wave functions exhibits the scattering amplitude:

$$\Psi \rightarrow e^{i\vec{k}\vec{r}} + \frac{i}{2} k^{-1} \sum_{l=0}^{\infty} (2l+1) P_l(\cos \theta) (1 - U_l) \frac{e^{ikr}}{r} \quad (2.23)$$

$$\rightarrow e^{i\vec{k}\vec{r}} + f(\theta) \frac{e^{ikr}}{r} \quad (2.24)$$

where one has carefully isolated the amplitude:

$$f(\theta) = \frac{i}{2}k^{-1} \sum_{l=0}^{\infty} (2l+1)P_l(\cos\theta)(1-U_l) \quad (2.25)$$

So the cross section for elastic scattering is now:

$$\sigma = \int |f(\theta)|^2 d\Omega \quad (2.26)$$

$$= \frac{\pi}{k^2} \sum_{l=0}^{\infty} (2l+1)|1-U_l|^2 \quad (2.27)$$

where the orthogonality of Legendre polynomials has been used (*i.e.* $\int P_m P_n = \frac{2}{2n+1}\delta_{mn}$). Equation 2.27 is a sum over every possible channel, only represented here by orbital momentum l .

Very similarly, the cross section for any reaction from channel c to channel c' will be:

$$\sigma_{cc'} = \frac{\pi}{k^2} \times g_J \times |\delta_{cc'} - U_{cc'}|^2 \quad (2.28)$$

with g_J being the statistical spin factor (the probability for spin coupling to match the final state spin). With J the spin of the final state, s the spin of the neutron ($s=1/2$) and I the spin of the target nucleus:

$$g_J = \frac{2J+1}{(2s+1)(2I+1)} \quad (2.29)$$

2.1.2 Resonant reactions: the compound nucleus model

In 1936, the first neutron resonances are observed [3]. The existence of very narrow states reached by neutron capture gives Niels Bohr the idea of compound nucleus formation. In terms of the uncertainty principle, a very narrow energy width means a very long lifetime:

$$\Gamma \times \tau \approx \hbar \quad (2.30)$$

with Γ being the energy width of the state, and τ its lifetime. A quick order of magnitude calculation for a resonant state with $\Gamma=1$ eV gives $\tau=6.6 \times 10^{-16}$ s. This duration is to be compared with the typical times of nuclear interaction of less than 10^{-20} s. Therefore the resonant state lives for an extremely long time compared to the nuclear times. Such a long lifetime is explained by the great complexity of the wave function of the nuclear state. The exit channel wave functions are so different from the initial state that it takes a very long time before a decay is possible. In order to explain this complex wave function, Bohr has the idea of the compound nucleus. When a neutron interacts with a nucleus in a non potential manner (because the potential is intrinsically different from a central mean field, the nuclear structure also has to be taken into account), it can share its energy with all

the nucleons. Therefore, many degrees of freedom can be excited, and the many body wave function is then much more difficult to describe than a simple creation operator on a empty shell of the ground state. The particularity of such long lived states is that it is now relevant to assume that the decay channel is independent of the entrance (or formation) channel. This leads to the Breit-Wigner formula for a single level resonant state. Let σ_{ab} be the cross section from entrance channel a to exit channel b . Let the partial widths for compound nucleus formation through channels a and b be Γ_a and Γ_b respectively (see the following sections for a more rigorous definitions of partial widths). The total width of the state is a sum of partial widths for every channel c .

$$\Gamma = \sum_c \Gamma_c \quad (2.31)$$

Then the decay probability through channel b is given by $\frac{\Gamma_b}{\Gamma}$. The cross section for $a \rightarrow b$ reaction can then be written:

$$\sigma_{ab} = \underbrace{\frac{\pi}{k^2} \times g_J \times \Gamma_a}_{\text{Formation through channel } a} \times \underbrace{P(E - E_\lambda)}_{\text{Uncertainty on eigen energy}} \times \underbrace{\frac{\Gamma_b}{\Gamma}}_{\text{Exit channel}} \quad (2.32)$$

Finally, $P(E - E_\lambda)$ is the probability density to form an eigen state with energy E_λ even though the available energy in the reaction is E . This term can be obtained using once again the uncertainty principle. Indeed it is the Fourier transform of the probability for a state to live for a time t , knowing its lifetime τ , with τ and Γ being related by equation 2.30. Here the key assumption is to assume an exponential dependence of the survival probability of the resonant state. Then one can easily calculate:

$$P(E - E_\lambda) = \text{FT} \left(e^{-t/2\tau} \right) \quad (2.33)$$

$$= \int_{-\infty}^{\infty} e^{-\Gamma t/2\hbar} \times e^{-i\omega t} \quad (2.34)$$

$$= \int_{-\infty}^{\infty} e^{-\Gamma t/2\hbar} \times e^{-i|E - E_\lambda|t/\hbar} \quad (2.35)$$

$$= \frac{\Gamma}{\frac{\Gamma^2}{4} + (E - E_\lambda)^2} \quad (2.36)$$

Substituting $P(E - E_\lambda)$ in equation 2.32 yields the well known single level Breit-Wigner formula:

$$\sigma_{ab} = \frac{\pi}{k^2} \times g_J \times \frac{\Gamma_a \Gamma_b}{\frac{\Gamma^2}{4} + (E - E_\lambda)^2} \quad (2.37)$$

2.2 Continuum coupling formalism

Historically, the prescription for the exponential form in the derivation of $P(E - E_\lambda)$ in equation 2.32 was a rather *ad hoc* step. It was derived in the case of atomic

resonances using perturbation theory together with the argument of a weak electromagnetic coupling, but it is evident that nuclear forces should not be treated as perturbations. The exponential term is above all justified by the long lived character of the state, and does not come from a more general theory of reactions. In order to give more physical meaning to the parameters of the cross section, a formal reaction theory is needed. It should be applicable to any type of reaction (direct or through compound nucleus formation) and explicitly show the link between the Hamiltonian and the cross section. Physically, the occurrence of a resonance in the cross section denotes the presence of a nuclear eigenstate. Therefore it should be present in the nuclear Hamiltonian. This section gives a brief description of a reaction formalism that explicitly links the nuclear Hamiltonian and the cross section. This is a continuum coupling using Feshbach projection operators [47]. An interesting declination of this theory is the continuum shell model [48, 49]. It has recently been used for light exotic nuclei and compared to R-matrix results (see the work on ${}^8\text{B}$ by J.P. Mitchell et al. [50]). Although one of its main advantages is the possibility of cross section calculation starting from a structure Hamiltonian, it will not be used or presented for that in this work, but from a formal perspective. First, the poor knowledge of nuclear interactions in heavy mass nuclei at high excitation energies prevents any accurate cross section prediction; but above all, it is of great pedagogical interest to present both the continuum coupling method and the R-matrix, and underline similarities and differences. Indeed these are two major theoretical reaction formalisms, and any relevant comment on the use of one or the other should be fully informed.

2.2.1 From the full wave function to the transition amplitude

In equation 2.8, the asymptotic wave function was connected to the transition amplitude. In this section is derived a formal link between the transition amplitude, the interaction potential, and the full wave function in the incoming channel. Let $\Psi(\vec{r}, q)$ be a full wave function of a colliding system. Let us remember that for an external-like wave function, *i.e.* for $r \rightarrow \infty$, $\Psi(\vec{r}, q) = \chi(\vec{r})\epsilon(q)$, with χ including the radial and angular components, and ϵ being the internal degrees of freedom wave function. The full Hamiltonian H_b in any reaction channel b is defined as:

$$H_b = H_b^0 + T_b + V_b \quad (2.38)$$

where H_b^0 gives the internal energies of the partners, T_b is the relative kinetic energy operator, and V_b is the interaction potential between the pair. Note that V_b depends on both q and \vec{r} . Let us denote by E_b the total relative energy: $E_b = H_b - H_b^0$. Therefore the Schrödinger equation is:

$$(E_b - T_b)\Psi(\vec{r}, q) = V_b(\vec{r}, q)\Psi(\vec{r}, q) \quad (2.39)$$

One can multiply this equation by $\epsilon_b^*(q)$ and integrate over all possible q .

$$(E_b - T_b)\chi(\vec{r}) = \int \epsilon_b^*(q)V_b(\vec{r}, q)\Psi(\vec{r}, q)dq \quad (2.40)$$

and solve this equation for $\chi(\vec{r})$ using Green propagator techniques (see [46] for more details). Asymptotically it yields:

$$\chi(\vec{r}) \rightarrow e^{i\vec{k}_b\vec{r}} - \frac{\mu_b}{2\pi\hbar^2} \frac{e^{ik_b r}}{r} \int \int e^{-i\vec{k}_b\vec{r}'} \epsilon_b^*(q)V_b(\vec{r}', q)\Psi(\vec{r}', q)d\vec{r}'dq \quad (2.41)$$

Finally, one can identify the transition amplitude in the second term, generalizing for any $a \rightarrow b$ transition:

$$f_{ab} = -\frac{\mu_b}{2\pi\hbar^2} \langle e^{i\vec{k}_b\vec{r}} | V_b | \Psi_a \rangle \quad (2.42)$$

It is usually more convenient to work with the transition matrix:

$$\mathcal{T}_{ab} = \langle e^{i\vec{k}_b\vec{r}} | V_b | \Psi_a \rangle \quad (2.43)$$

In the following is introduced a powerful formalism, based on projection operators, in order to reach resonance formulas from equation 2.43.

2.2.2 From projection operators to resonances

The total wave function of the many body problem is assumed to be spanned over two orthogonal spaces \mathcal{P} and \mathcal{Q} . The \mathcal{P} space is composed of pure continuum (or scattering) wave functions, which are the solutions of the Schrödinger equation with positive energy and no nuclear potential. The states are not normalized like a standard Hilbert space state, for they belong in the continuum. The \mathcal{Q} space denotes internal "bound" states (*i.e.* with no particle in the continuum, hence it includes compound nuclear states). The use of quotation marks for the bound character of these states is due to its ambiguity. The states in \mathcal{Q} space are normalized states, in the sens of Hilbert space normalization. The bound character is expressed through the fact that the presence probability of a nucleon vanishes quickly as one goes away from the nucleus. Moreover, these states can have significant life times (see the discussion on the compound nucleus in section 2.1.2). However, decay channels are open, since the total energy of the system can be positive (and it is in the case of scattering). This decomposition means that any state $|\Psi\rangle$ can be split into its two projections over \mathcal{P} and \mathcal{Q} :

$$|\Psi\rangle = P|\Psi\rangle + Q|\Psi\rangle \quad (2.44)$$

$$= |\Psi_P\rangle + |\Psi_Q\rangle \quad (2.45)$$

with P and Q denoting projection operators on \mathcal{P} and \mathcal{Q} respectively. They must verify the following properties:

$$P^2 = P \quad (2.46)$$

$$Q^2 = Q \quad (2.47)$$

$$P + Q = 1 \quad (2.48)$$

$$PQ = QP = 0 \quad (2.49)$$

which also implies that \mathcal{P} and \mathcal{Q} form an orthonormal basis of the full Hilbert space. Therefore, the full hamiltonian H can also be projected onto \mathcal{P} and \mathcal{Q} :

$$H = PHP + PHQ + QHP + QHQ \quad (2.50)$$

$$= H_{PP} + H_{PQ} + H_{QP} + H_{QQ} \quad (2.51)$$

And the Schrödinger equation is:

$$H|\Psi\rangle = E|\Psi\rangle \quad (2.52)$$

$$= H_{PP}|\Psi_P\rangle + H_{QP}|\Psi_P\rangle + H_{PQ}|\Psi_Q\rangle + H_{QQ}|\Psi_Q\rangle \quad (2.53)$$

It can be difficult to connect all projections of H to a physical picture, but if one tries to identify the Hamiltonian of equation 2.53 to the one of equation 2.38, a few comments can be made. First, H_{QQ} must only act on purely bound states, and give their excitation spectrum. Hence it can be identified to H_b^0 , the internal Hamiltonian of equation 2.38. Then, H_{PP} must act only on scattering states, and give the energy of the system, without consideration of any internal degree of freedom (which would be in the \mathcal{Q} space). Therefore H_{PP} must contain the relative kinetic energy operator T . It will also contain V_{PP} . Then, it is natural to conclude the analysis with $H_{PQ} = V_{PQ}$ and $H_{QP} = V_{QP}$ (which is recommended by Feshbach [47]).

$$H = \underbrace{H_{QQ}}_{H_0} + \underbrace{H_{PP}}_{T+V_{PP}} + \underbrace{H_{PQ}}_{V_{PQ}} + \underbrace{H_{QP}}_{V_{QP}} \quad (2.54)$$

Physically, V_{PQ} and V_{QP} couple scattering states and bound states, they are responsible for the presence of scattering resonances. Projecting equation 2.53 on both \mathcal{P} and \mathcal{Q} yields:

$$(E - H_{PP})|\Psi_P\rangle = H_{PQ}|\Psi_Q\rangle \quad (2.55)$$

$$(E - H_{QQ})|\Psi_Q\rangle = H_{QP}|\Psi_P\rangle \quad (2.56)$$

One can use Green propagators to formally solve for $|\Psi_P\rangle$ and $|\Psi_Q\rangle$, with the choice that no incoming wave is present in \mathcal{Q} space, but that there is one in \mathcal{P} space. Physically, this means that the system is initially in a pure \mathcal{P} state (scattering),

and the interaction will couple \mathcal{P} and \mathcal{Q} , giving a chance for the system to be observed in a \mathcal{Q} state.

$$|\Psi_P\rangle = |\chi_a\rangle + \frac{1}{E - H_{PP}} H_{PQ} |\Psi_Q\rangle \quad (2.57)$$

$$|\Psi_Q\rangle = \frac{1}{E - H_{QQ}} H_{QP} |\Psi_P\rangle \quad (2.58)$$

with $|\chi_a\rangle$ being an incident plane wave in channel a . Details on reaction channels will be given in section 2.3, so far let us assume that every information on the scattering pair is included in a . Now if one substitutes equation 2.57 in equation 2.56, one finds a very useful expression for $|\Psi_Q\rangle$:

$$(E - H_{QQ})|\Psi_Q\rangle = H_{QP}|\chi_a\rangle + H_{QP}\frac{1}{E - H_{PP}}H_{PQ}|\Psi_Q\rangle \quad (2.59)$$

$$|\Psi_Q\rangle = \frac{1}{E - H_{QQ} - W_{QQ}} H_{QP} |\chi_a\rangle \quad (2.60)$$

$$\text{with } W_{QQ} = H_{QP} \frac{1}{E - H_{PP}} H_{PQ} \quad (2.61)$$

This expression for $|\Psi_Q\rangle$ can be used together with the \mathcal{P} and \mathcal{Q} decomposition of $|\Psi_a\rangle$ in equation 2.43 giving the transition matrix.

$$\mathcal{T}_{ab} = \langle \chi_b | V_b | \Psi_a \rangle \quad (2.62)$$

$$= \langle \chi_b | V_b | |\Psi_P\rangle + |\Psi_Q\rangle \rangle \quad (2.63)$$

$$= \langle \chi_b | V_b | \Psi_P \rangle + \langle \chi_b | V_b \frac{1}{E - H_{QQ} - W_{QQ}} H_{QP} |\chi_a \rangle \quad (2.64)$$

The first term is to be seen as a "prompt" scattering process, acting only in the \mathcal{P} subspace. This can well account for potential scattering contribution in the cross section. In the second term, a resonance-like formula arises. It can be written as $\langle \chi_b | V_b | \Psi_Q \rangle$. Remembering that $|\chi_b\rangle$ is a \mathcal{P} state the term does not change if P and Q projections are added in the following manner:

$$\langle \chi_b | V_b | \Psi_Q \rangle = \langle \chi_b | P V_b Q | \Psi_Q \rangle \quad (2.65)$$

Therefore V_b can be replaced by V_{PQ} (and eventually by H_{PQ}) in the second term:

$$\mathcal{T}_{ab} = \mathcal{T}_{ab}^{(P)} + \langle \chi_b | V_{PQ} \frac{1}{E - H_{QQ} - W_{QQ}} H_{QP} |\chi_a \rangle \quad (2.66)$$

$$= \mathcal{T}_{ab}^{(P)} + \langle \chi_b | H_{PQ} \frac{1}{E - H_{QQ} - W_{QQ}} H_{QP} |\chi_a \rangle \quad (2.67)$$

The second term in the last formula accounts for resonant scattering from channel a to channel b . It represents the coupling from the pure continuum state $|\chi_a\rangle$

to a \mathcal{P} and \mathcal{Q} mixed state, then propagation in \mathcal{Q} space through the effective Hamiltonian $H_{QQ} + W_{QQ}$, and finally re-emission into \mathcal{P} space through the action of H_{PQ} . The effective Hamiltonian $H_{QQ} + W_{QQ}$ has the characteristics of being non hermitian and depending on the total reaction energy E (because of W_{QQ}). Its eigenvalues are the pole of the \mathcal{T} matrix, and therefore the resonances in the spectrum. They can be expressed as:

$$\mathcal{E}_\lambda(E) = E_\lambda + \Delta_\lambda(E) - \frac{i}{2}\Gamma_\lambda(E) \quad (2.68)$$

with E_λ being the eigenvalues of H_{QQ} , Δ_λ being an energy shift due to the coupling of \mathcal{Q} into \mathcal{P} , and Γ_λ being the resonance width. In the case of a single resonant state $|\Phi_s\rangle$ (*i.e.* a single \mathcal{Q} space state), equation 2.67 reduces to:

$$\mathcal{T}_{ab} = \mathcal{T}_{ab}^{(P)} + \frac{\langle\chi_b|H_{PQ}|\Phi_s\rangle\langle\Phi_s|H_{QP}|\chi_a\rangle}{E - E_s - \langle\Phi_s|W_{QQ}|\Phi_s\rangle} \quad (2.69)$$

where naturally:

$$\langle\Phi_s|W_{QQ}|\Phi_s\rangle = \Delta_s(E) - \frac{i}{2}\Gamma_s(E) \quad (2.70)$$

In addition, in the case of a single resonance, the total width of the state Γ_s is a sum over every channel partial width:

$$\Gamma_s(E) = 2\pi \sum_c |\langle\Phi_s|H_{QP}|\chi_c\rangle|^2 \quad (2.71)$$

$$= \sum_c \Gamma_{sc}(E) \quad (2.72)$$

However, it should be stressed that in the more general case of many eigenstates in \mathcal{Q} space, the eigenvectors of $H_{QQ} + W_{QQ}$, denoted by $|\Omega_\mu\rangle$, are linear combinations of the $|\Phi_s\rangle$ states.

$$|\Omega_\mu\rangle = \sum_s \langle\Phi_s|\Omega_\mu\rangle |\Phi_s\rangle \quad (2.73)$$

and the transition matrix element can only be expanded in terms of the basis $\{\Omega_\mu\}$.

$$\mathcal{T}_{ab} = \mathcal{T}_{ab}^{(P)} + \sum_\mu \frac{\langle\chi_b|H_{PQ}|\Omega_\mu\rangle\langle\Omega_\mu|H_{QP}|\chi_a\rangle}{E - \mathcal{E}_\mu} \quad (2.74)$$

Thus the only remaining relation between the widths ($\Gamma_\mu = -2\text{Im}(\mathcal{E}_\mu)$) and the W_{QQ} matrix is:

$$\sum_\mu \text{Im}(\mathcal{E}_\mu) = \sum_s \text{Im}(\langle\Phi_s|W_{QQ}|\Phi_s\rangle) \quad (2.75)$$

Therefore it is not possible anymore to perform the analysis of the width in terms of partial contributions from every channel. It is also composed of contributions for every level.

2.3 The R-matrix theory of nuclear reactions

The R-matrix formalism for nuclear reactions was first inspired by the work of Kapur and Peierls in 1938 [51], but the current R-matrix theory was designed by Wigner and Eisenbud in 1947 [52]. A complete description of the theory is given in the Lane and Thomas review of 1958 [53]. A more concise explanation can be found in Lynn's manual on neutron resonance theory [54] and the Nuclear energy agency report on nuclear evaluation [55]. Also, a recent and thorough presentation of the theory can be found in a review by P. Descouvemont [56].

2.3.1 Principles of the R-matrix theory

The whole idea of the R-matrix theory is governed by the practical impossibility of solving the Schrödinger equation in the compound nucleus. This assumption is still valid today, and makes this approach the best tool for describing resonances. On the other hand, when the two colliding partners (for example a neutron and a nucleus) are far enough from each other, the nuclear forces are essentially equal to zero and the problem becomes a standard scattering problem (like in section 2.1.1). It is then natural to split the wave function into two parts.

- An internal part that is not to be solved and represents the rigorous wave function of the compound nucleus.
- An external part which is valid after a certain interaction radius a_c , with radial wave functions equal to spherical Bessel functions (in the case of neutron reaction, *i.e.* no Coulomb interaction).

The major argument to use is then that the wave function and its derivative have to be continuous at $r = a_c$. From this matching will follow a link between the collision matrix \mathbf{U} and a reaction matrix \mathbf{R} , defined through resonance energies and reduced widths. The reduced widths will be expressed as surface overlaps of internal wave functions. Then the link between the collision matrix and the cross section will use equation 2.27. The first subsection will give a short derivation of the fundamental R-matrix relations that are broadly used in calculation codes (or their approximations), then the level matrix formulation will be given, and finally the photon channels will be included, with the commonly used Reich-Moore approximation.

2.3.2 The R matrix theory

A reaction channel will be denoted by c , and includes both the colliding partners α_1 and α_2 , with their spins I_1 and I_2 and projections on a quantization axis i_1 and i_2 . It also contains the channel spin s and projection v , obtained by coupling the

spins of the pair. Finally, one must not forget the relative angular momentum l . The full channel wave function of the system in the external region is:

$$\Psi_c = i^l Y_l^m \psi_c \frac{u_c(r)}{r} \quad (2.76)$$

where ψ_c is the channel spin wave function, *i.e.* a linear combination of internal functions of the pair that match the total channel spin s and projection v .

$$\psi_c = \sum_{i_1+i_2=v} (I_1 I_2 i_1 i_2 | s v) \psi_{\alpha_1 I_1 i_1} \psi_{\alpha_2 I_2 i_2} \quad (2.77)$$

with $(I_1 I_2 i_1 i_2 | s v)$ being the Clebsh-Gordan coefficient for spin coupling. It is convenient to define a surface function φ_c so that:

$$\varphi_c = \frac{\psi_c i^l Y_l^m}{r} \quad (2.78)$$

$$\text{Hence } \Psi_c = \varphi_c u_c(r) \quad (2.79)$$

These surface functions are assumed to be a full set of ortho-normalized functions, so that on the nuclear surface \mathcal{S} at $r = a_c$ (with the nuclear volume differential $d\tau = d\mathcal{S}dr$):

$$\Psi = \sum_c \left(\int_{\mathcal{S}} \varphi_c^* \Psi d\mathcal{S} \right) \varphi_c \quad (2.80)$$

$$= \sum_c u_c(a_c) \varphi_c(a_c) \quad (2.81)$$

The coordinates included in the surface \mathcal{S} are the spherical angles θ , ϕ of the relative motion and the internal coordinates of the channel spin wave function. Basically the following derivation makes a full use of the two possible expansions for Ψ on \mathcal{S} , respectively the channel expansion and the eigen vector expansion:

$$\Psi = \sum_c \varphi_c u_c \quad (2.82)$$

$$= \sum_{\lambda} \langle \Psi_{\lambda} | \Psi \rangle \Psi_{\lambda} \quad (2.83)$$

Here the continuity argument is already used, since the channel expansion concerns the external region (where the system is considered an unbound pair), and the eigenstate expansion concerns the internal region (where the system is a superposition of normalized nuclear eigenstates). One also notices a conceptual difference with the continuum coupling scheme. Indeed, the internal wave function in section 2.2 is a sum of a continuum wave function $|\Psi_P\rangle$ and a superposition of "bound" states $|\Psi_Q\rangle$, whereas in the R-matrix theory the internal state is only composed of \mathcal{Q} states (equation 2.83). This difference is practically seen in the

interpretation of potential scattering in the R-matrix cross section. The phase shift extracted from the R-matrix theory naturally presents with a *hard-sphere* scattering phase shift (see equation 2.104). It can be interpreted as potential scattering, but it lacks physical justification, particularly since no explicit connection to the interaction between the pair has been made. Continuum coupling includes this feature more naturally, stressing the fact that the \mathcal{P} and \mathcal{Q} spaces are not to be exactly identified with the internal and external regions of the R-matrix. In principle, one could define P and Q projections to be the geometrical separation of the R-matrix, and the interaction would then contain surface terms (V_{PQ} and V_{QP}) ensuring the continuity of the full wave function on the nuclear surface. In this sense, the matching of internal and external wave functions is analogous to a certain \mathcal{P} and \mathcal{Q} decomposition, but is not the one detailed in the previous section, where the full wave function is always coupled to the continuum.

The whole idea leading the derivation lies in the eigenstate expansion 2.83. The overlaps $\langle \Psi_\lambda | \Psi \rangle$ are unknown, and will be derived on the nuclear surface using the Schrödinger equation. Contributions coming from the eigenstates $|\Psi_\lambda\rangle$ on \mathcal{S} will be expressed as surface overlaps, and become parameters of the theory. Finally, this expansion of the internal state will be set equal to the external state at $r = a_c$, expressed with the collision matrix \mathbf{U} , thus providing a full link between surface overlaps (to be fitted to data) and the cross section.

Let us start by writing the Schrödinger equation for two states Ψ_λ and Ψ on the nuclear surface \mathcal{S} , the subscript λ denoting the eigenstate.

$$\frac{-\hbar^2}{2\mu} \Delta \Psi + V \Psi = E \Psi \quad (2.84)$$

$$\frac{-\hbar^2}{2\mu} \Delta \Psi_\lambda + V \Psi_\lambda = E_\lambda \Psi_\lambda \quad (2.85)$$

Let us stress once more that the continuity on \mathcal{S} is a requirement here, since the operator $\Delta = \nabla^2$ here refers to the spatial derivative of the relative motion, thus this Schrödinger equation has to be applied to an external-like wave function, of the form of equation 2.76. Hence the full kinetic energy operator is applied to the unbound pair of reduced mass μ , and has nothing to do with the internal structure of the system. It is a key assumption that the internal wave function, although not at all expressible as a pair in a certain channel, can yet take this form only at $r = a_c$.

Then one can multiply the first equation by Ψ_λ^* and the complex conjugate of the

second by Ψ :

$$\frac{-\hbar^2}{2\mu} \Psi_\lambda^* \Delta \Psi + \Psi_\lambda^* V \Psi = E \Psi_\lambda^* \Psi \quad (2.86)$$

$$\frac{-\hbar^2}{2\mu} \Delta \Psi_\lambda^* \Psi + V^* \Psi_\lambda^* \Psi = E_\lambda \Psi_\lambda^* \Psi \quad (2.87)$$

$$(2.88)$$

Then subtract the two, assuming that V (with the centrifugal part included) is hermitian, *i.e.* $V^* = V$:

$$\frac{-\hbar^2}{2\mu} [\Psi_\lambda^* \Delta \Psi - \Delta \Psi_\lambda^* \Psi] = (E - E_\lambda) \Psi_\lambda^* \Psi \quad (2.89)$$

and integrate over the nuclear volume τ using Green's theorem and the fact that the volume differential $d\tau = d\mathcal{S}dr$:

$$\frac{-\hbar^2}{2\mu} \left(\left[\int_{\mathcal{S}} \Psi_\lambda^* \nabla \Psi d\mathcal{S} \right]_{r=0}^{r=a_c} - \left[\int_{\mathcal{S}} \nabla \Psi_\lambda^* \Psi d\mathcal{S} \right]_{r=0}^{r=a_c} \right) = (E - E_\lambda) \langle \Psi_\lambda | \Psi \rangle \quad (2.90)$$

The terms containing the products $\nabla \Psi_\lambda^* \nabla \Psi$ canceled each other. The terms for $r = 0$ vanish due to the regularity of the radial part of the solution $\frac{u_c}{r}$ at $r = 0$. Let us now use the channel expansion of equation 2.82:

$$\frac{\hbar^2}{2\mu} \left(\sum_c \left(\frac{du_c}{dr} \right)_{r=a_c} \underbrace{\int_{\mathcal{S}} \Psi_\lambda^* \varphi_c d\mathcal{S}}_{u_{\lambda c}^*(a_c)} - \sum_c u_c(a_c) \underbrace{\int_{\mathcal{S}} \nabla \Psi_\lambda^* \varphi_c d\mathcal{S}}_{\frac{d}{dr} u_{\lambda c}^*(r=a_c)} \right) = (E_\lambda - E) \langle \Psi_\lambda | \Psi \rangle \quad (2.91)$$

Let us define the reduced width amplitude:

$$\gamma_{\lambda c} = \sqrt{\frac{\hbar^2}{2\mu a_c}} u_{\lambda c}^*(a_c) = \sqrt{\frac{\hbar^2}{2\mu a_c}} \int_{\mathcal{S}} \varphi_c \Psi_\lambda^* d\mathcal{S} \quad (2.92)$$

Hence equation 2.91 becomes:

$$\sum_c \left(\frac{\hbar^2}{2\mu a_c} \right)^{1/2} \gamma_{\lambda c} \left[a_c \left(\frac{du_c}{dr} \right)_{r=a_c} - u_c(a_c) \frac{a_c \frac{d}{dr} u_{\lambda c}^*(a_c)}{u_{\lambda c}^*(a_c)} \right] = (E_\lambda - E) \langle \Psi_\lambda | \Psi \rangle \quad (2.93)$$

The boundary condition for the eigen wave function can be written:

$$B_c = a_c \frac{\frac{d}{dr} u_{\lambda c}^*(a_c)}{u_{\lambda c}^*(a_c)} \quad (2.94)$$

and assumed to be independent of λ . Then:

$$\langle \Psi_\lambda | \Psi \rangle = (E_\lambda - E)^{-1} \sum_c \left(\frac{\hbar^2}{2\mu a_c} \right)^{1/2} \gamma_{\lambda c} \left[\left(a_c \frac{du_c}{dr} \right)_{r=a_c} - u_c(a_c) B_c \right] \quad (2.95)$$

And now the eigenstate expansion 2.83 can be used:

$$\Psi = \sum_\lambda \sum_c \left(\frac{\hbar^2}{2\mu a_c} \right)^{1/2} \frac{\gamma_{\lambda c}}{E_\lambda - E} \left[\left(a_c \frac{du_c}{dr} \right)_{r=a_c} - u_c(a_c) B_c \right] \Psi_\lambda \quad (2.96)$$

Projecting on $\langle \psi'_c |$ and using the definition of reduced widths (equation 2.92) leads to what is referred to as the fundamental R-matrix relation in the Lane and Thomas review (although with different notations):

$$\left(\frac{\hbar^2}{2\mu a_{c'}} \right)^{1/2} u_{c'} = \sum_c \left(\frac{\hbar^2}{2\mu a_c} \right)^{1/2} R_{cc'} \left[\left(a_c \frac{du_c}{dr} \right)_{r=a_c} - u_c(a_c) B_c \right] \quad (2.97)$$

with the R-matrix elements defined as:

$$R_{cc'} = \sum_\lambda \frac{\gamma_{\lambda c} \gamma_{\lambda c}^*}{E_\lambda - E} \quad (2.98)$$

For matching the external and the internal region, one replaces the radial wave functions in equation 2.97 by their external region normalized expression using the \mathbf{U} matrix:

$$u_c = \frac{1}{v^{1/2}} \left(I_c - \sum_{c'} U_{cc'} O_c \right) \quad (2.99)$$

Using the fact that $\hbar k = \mu v$ and $\rho_c = k a_c$, and understanding the bold characters as matrices (with one channel c per dimension) and the prime in I'_c and O'_c as derivative with respect to ρ , equation 2.97 becomes:

$$\boldsymbol{\rho}^{-1/2} (\mathbf{I} - \mathbf{U}\mathbf{O}) = \mathbf{R}\boldsymbol{\rho}^{-1/2} [(\boldsymbol{\rho}\mathbf{I}' - \boldsymbol{\rho}\mathbf{U}\mathbf{O}') - \mathbf{B}(\mathbf{I} - \mathbf{U}\mathbf{O})] \quad (2.100)$$

where $\boldsymbol{\rho}$, \mathbf{I} , \mathbf{O} and \mathbf{B} are taken as diagonal matrices with elements ρ_c , I_c , O_c , and B_c .

Finally it is necessary to define the \mathbf{L} and \mathbf{L}^* matrices:

$$\mathbf{L} = \boldsymbol{\rho}\mathbf{O}'\mathbf{O}^{-1} = \mathbf{S} + i\mathbf{P} \quad (2.101)$$

$$\mathbf{L}^* = \boldsymbol{\rho}\mathbf{I}'\mathbf{I}^{-1} = \mathbf{S} - i\mathbf{P} \quad (2.102)$$

with \mathbf{S} and \mathbf{P} being called respectively the shift and penetration factor matrices, a denomination that will become clear in the next section. So far, they are just the real and imaginary parts of the logarithmic derivative of the outgoing scattering

wave function, with diagonal matrix elements S_c and P_c . One can now get the final relation between \mathbf{U} and \mathbf{R} matrices:

$$\mathbf{U} = \boldsymbol{\rho}^{1/2} \mathbf{O}^{-1} (\mathbf{1} - \mathbf{R}\mathbf{L})^{-1} (\mathbf{1} - \mathbf{R}\mathbf{L}^*) \mathbf{I} \boldsymbol{\rho}^{-1/2} \quad (2.103)$$

Before moving on, it is meaningful to mention the boundary condition matrix \mathbf{B} and the interaction radius a_c . At first sight, they seem to be free parameters of the theory, and yet, it makes no physical sense that the observables may depend on either of them. The only requirement concerning a_c is that it has to be greater than the range of the nuclear interaction. Apart from this constraint, any choice for \mathbf{B} or a_c is supposed to give the same observable result, because their dependence compensates each other, although not in a very straightforward manner. The interested reader is referred to Lane and Thomas [53] for a few more details on that matter. A common choice in calculation codes is to set a_c equal to the scattering radius of the nucleus. Concerning the boundary conditions B_c , they are usually set equal to the shift factors S_c (see the following sections), since it makes the formulas as close as possible to the one level approximation, which can be useful for interpretation purposes. Indeed if $B_c = S_c$, then the shift factor corrected for the boundary condition is equal to zero. This is a practical way of nullifying the effect of other levels on the energy shift, just like if there was only one level. As discussed in section 2.2, the validity of this approximation allows one to identify clear channel partial widths, and more generally to easily connect the properties of the eigenstate to the compound nucleus decay, since this interpretation is highly non trivial for a general many-level spectrum (see Lane and Thomas [53] for more details on the one-level approximation and its interpretations).

A useful formulation for the following section is found by defining $\boldsymbol{\Omega}$ matrix:

$$\Omega_c = \left(\frac{I_c(a_c)}{O_c(a_c)} \right)^{1/2} = e^{-i\phi_c} \quad (2.104)$$

with the hard-sphere scattering phase shift:

$$\phi_c = \tan^{-1} \left(\frac{\text{Im}(O_c)}{\text{Re}(O_c)} \right)_{r=a_c} \quad (2.105)$$

and by noticing the following useful property of Coulomb functions:

$$P_c = \left(\frac{\rho_c}{I_c O_c} \right) \quad (2.106)$$

Hence:

$$\mathbf{U} = \boldsymbol{\Omega} \mathbf{W} \boldsymbol{\Omega} \quad (2.107)$$

with $\mathbf{W} = \mathbf{P}^{1/2} (\mathbf{1} - \mathbf{R}(\mathbf{L} - \mathbf{B}))^{-1} (\mathbf{1} - \mathbf{R}(\mathbf{L} - \mathbf{B})) \mathbf{P}^{-1/2}$.

Together with equation 2.28, the connection between parameters of the resonant states (contained in the \mathbf{R} matrix) and the cross section has been made.

2.3.3 The level matrix formulation

The main problematic term in equation 2.103 is the inverse matrix $(\mathbf{1} - \mathbf{R}\mathbf{L})^{-1}$. Let us define $\mathbf{L}^0 = \mathbf{L} - \mathbf{B}$. In order not to perform this possibly cumbersome inversion, one can assume this term is composed of a contribution from each eigenstate in the following way:

$$(\mathbf{1} - \mathbf{R}\mathbf{L}^0)^{-1} = \mathbf{1} + \sum_{\mu\nu} (\gamma_\mu (\mathbf{L}\gamma_\nu)^\dagger) A_{\mu\nu} \quad (2.108)$$

with the $\gamma_{\mu,\nu}$ being channel vectors. The \mathbf{L}^0 matrix can be taken as a sum of a real part and an imaginary one, assuming \mathbf{B} is a real matrix:

$$\mathbf{L}^0 = \mathbf{S} - \mathbf{B} + i\mathbf{P} \quad (2.109)$$

$$= \mathbf{S}^0 + i\mathbf{P} \quad (2.110)$$

The \mathbf{S}^0 and \mathbf{P} matrices are diagonal and filled with shift factors S_c^0 and penetration factors P_c . This denomination becomes clearer if ones derives the \mathbf{A} matrix terms starting from equation 2.108:

$$\mathbf{A} = (\mathbf{e} - \mathbf{E} - \boldsymbol{\xi})^{-1} \quad (2.111)$$

with \mathbf{e} and \mathbf{E} level matrices being diagonally filled respectively with eigen energies E_λ and relative kinetic energy E . The last term $\boldsymbol{\xi}$ is given by:

$$\xi_{\lambda\mu} = \mathbf{L}\gamma_\lambda \cdot \gamma_\mu \quad (2.112)$$

$$= -\Delta_{\lambda\mu} + \frac{i}{2}\Gamma_{\lambda\mu} \quad (2.113)$$

The product $\mathbf{L}^0\gamma_\lambda \cdot \gamma_\mu$ is to be understood as a scalar product over channels. The term ξ denotes a shift of the poles of the level matrix by $-\Delta$ on the real axis. Indeed the $\Delta_{\lambda\mu}$ are closely related to the so-called shift factors of equation 2.110:

$$\Delta_{\lambda\mu} = \sum_c \Delta_{\lambda\mu c} \quad (2.114)$$

$$= \sum_c -S_c^0 \gamma_{\lambda c} \gamma_{\mu c} \quad (2.115)$$

The $\Gamma_{\lambda\mu}$ are energy widths (as the notation suggests), and are related to the reduced widths and to the penetration factors P_c , which merely quantify the centrifugal barrier penetrability.

$$\Gamma_{\lambda\mu} = \sum_c \Gamma_{\lambda\mu c} \quad (2.116)$$

$$= \sum_c 2P_c \gamma_{\lambda c} \gamma_{\mu c} \quad (2.117)$$

Although partial widths contributions $\Gamma_{\lambda\mu c}$ can be identified in this formalism, connecting the $\Gamma_{\lambda\mu}$ matrix elements to the actual width of the state is not straightforward if the \mathbf{A} matrix is not diagonal. Again, in the general case the resonance width is both a contribution from every channel (called partial width), but also a contribution from every level, included in the \mathbf{A} matrix (or in the W_{QQ} matrix elements in section 2.2).

Substituting the \mathbf{A} matrix expression into equation 2.107 gives a very interesting and useful expression for the collision matrix \mathbf{U} :

$$U_{cc'} = e^{-i(\phi_c + \phi_{c'})} \left(\delta_{cc'} + i \sum_{\lambda\mu} \Gamma_{\lambda c}^{1/2} A_{\lambda\mu} \Gamma_{\mu c}^{1/2} \right) \quad (2.118)$$

At this stage the similarity between the R-matrix formalism and continuum coupling can be seen in the structure of the \mathbf{A} matrix, and in comparing equations 2.118 and 2.74, although the connection between the full Hamiltonian and the resonant states is not as explicit in the R-matrix scheme. One other crucial difference is that the shift and penetration factors defined in the \mathbf{A} matrix are practically taken to be independent of the reaction energy when fitted to data, although they formally include an energy dependence. This possibility of neglecting energy dependence might not be so easy to do with a practical implementation of continuum coupling theory. Although this could lead to interpretation issues in the case of very large resonances, where the width varies significantly along the resonance, it is a major advantage in terms of parametrization for phenomenological purposes.

2.3.4 Treatment of photon channels

Including photons into the formalism

As it has been presented so far, the R-matrix theory is not applicable to photon channels, since the non massive character of photons prevents one from writing the Schrödinger equation just like for massive particles, and deriving expressions for widths and cross sections. However it is possible to treat the electromagnetic transitions in the compound nucleus as first order perturbations, so that the transition amplitudes can be written:

$$M_{fi} = \langle \Psi_f | H_{\text{EM}} | \Psi_i \rangle \quad (2.119)$$

with the interaction hamiltonian H_{EM} being derived using the charge current \mathbf{j} and magnetic moment $\boldsymbol{\mu}$ of the nucleus, and the vector potential \mathbf{A} and magnetic field $\mathbf{B} = \nabla \times \mathbf{A}$ of the photon perturbation:

$$H_{\text{EM}} = -(\mathbf{j} \cdot \mathbf{A} + \boldsymbol{\mu} \cdot \mathbf{B}) \quad (2.120)$$

This interaction hamiltonian can be expressed as a multipole expansion so that the final transition amplitude is expressed a sum of all EL and ML contributions.

With the transition amplitude being defined in this way, the Fermi golden rule of perturbation theory gives an expression for the half-life of the process:

$$\lambda = \tau^{-1} = \frac{2\pi}{\hbar} \rho M_{fi}^2 \quad (2.121)$$

with ρ being the energy density of photon states. Then the energy width for the gamma decay can be found by applying the uncertainty principle:

$$\Gamma_p \times \tau = \hbar \quad (2.122)$$

$$\Gamma_p = \hbar \times \lambda \quad (2.123)$$

$$= 2\pi\rho | \langle \Psi_f | H_{EM} | \Psi_i \rangle |^2 \quad (2.124)$$

If one treats this radiation width on the same foot as a particle width, the collision matrix expression with the level matrix still holds for the case of, say, (c, γ) reactions (c being any entrance channel):

$$U_{c,\gamma} = ie^{-i\phi_c} \sum_{\lambda\mu} \Gamma_c^{1/2} A_{\lambda\mu} \Gamma_\gamma^{1/2} \quad (2.125)$$

where the phase factor for photon channels has been included into the gamma width.

The Reich-Moore approximation

In the case of a gamma cascade from a resonant state to the ground state, not only several one photon transitions are necessary (the high level density at these excitation energies and the selection rules generally prohibit one photon transition from the compound nucleus to the ground state), but also the number of different possible gamma cascades is in general very large (once again due to the high level density). All these one photon transitions involved in the total gamma channel have comparable magnitudes, but random signs. Hence in the scalar product over channels of equation 2.112 (for getting the $A_{\lambda\mu}$ matrix elements), if $\lambda \neq \mu$, a large number of terms with random signs and comparable magnitudes will be summed, leading to a result normally distributed with zero mean. If $\lambda = \mu$ however, the gamma channels will effectively contribute to the \mathbf{A} matrix diagonal elements with a non-zero term. The idea of the Reich-Moore approximation is then simply to neglect all non diagonal contributions from photons channels in the \mathbf{A} matrix. This “channel elimination” method leads to a reduced R-matrix problem, restricted to the non photonic channels:

$$R_{cc'} = \sum_{\lambda} \frac{\gamma_{\lambda c} \gamma_{\lambda c'}^*}{E_{\lambda} - E - i\Gamma_{\lambda\gamma}/2} \quad (2.126)$$

The c and c' channels belong only to a non photonic channels subspace, and the only remaining contribution from photon channels is in the $\Gamma_{\lambda\gamma}$ term in the

denominator, being a sum over all possible gamma cascades. If α denotes a gamma cascade (including initial and final spins, parity, and all subsequent one photon steps p with given energy and multipolarity):

$$\Gamma_{\lambda\gamma} = \sum_{\alpha} \sum_{p \in \alpha} \Gamma_p \quad (2.127)$$

If the transition amplitudes are normally distributed with zero mean, then the Γ_p follow a χ^2 distribution with one degree of freedom, and therefore $\Gamma_{\lambda\gamma}$ follows a χ^2 distribution with as many degrees of freedom as the number of terms in the sum 2.127. Practically, if the sum runs over a very large number of terms, the distribution for $\Gamma_{\lambda\gamma}$ is approximately constant (*i.e.* a χ^2 distribution with an infinite number of degrees of freedom).

2.4 Statistical aspects of the compound nucleus

The previous paragraph stresses for the first time the fact that a highly excited nuclear state can be understood as a statistical system. The main assumption is that compound nuclear wave functions behave chaotically, in other words, electromagnetic matrix elements, or surface overlaps between resonant states and channel wave functions (*i.e.* reduced width amplitudes) are normally distributed with zero mean. This leads to the Porter-Thomas distributions for reaction widths [57]. This chaoticity of the wave functions comes from the random-like character in the Hamiltonian matrix elements. Assuming a gaussian-like distribution for nuclear Hamiltonians, it is possible to derive the distribution of level spacings, this is the Wigner surmise [58, 59].

2.4.1 The Porter Thomas distribution

At high excitation energies, a compound nuclear system has many excited degrees of freedom. Shell effects can couple to collective effects such as vibrational or rotational bands, nucleon pairs can be broken and even higher order correlations can come into play. With such complexity in mind, there is no reason why two successive states in the energy spectrum should have any similarity. This has a direct impact on the statistical properties of channel widths. Let us recall the expression of the reduced width amplitudes for particle and gamma channels:

$$\gamma_{\lambda c} = \sqrt{\frac{\hbar^2}{2\mu a_c}} \int_S \varphi_c \Psi_{\lambda}^* d\mathcal{S} \quad (2.128)$$

$$\gamma_{\lambda\gamma} = \sqrt{2\pi\rho} \langle \Psi_f | H_{EM} | \Psi_i \rangle \quad (2.129)$$

Given the complexity of $|\Psi_{\lambda}\rangle$, if one assumes that the surface overlap in equation 2.128 or the electromagnetic transition amplitude in 2.129 are normally distributed

with zero mean, then the reduced width $\gamma_{\lambda_c}^2$ exhibits a χ^2 distribution. Let us not be confused by the vocabulary, and remember that the reduced width amplitude is γ_{λ_c} , the reduced width for particle channels is $\Gamma_{\lambda_c}^0 = \gamma_{\lambda_c}^2$, and the observed width has to be corrected for penetrability: $\Gamma_{\lambda_c} = 2P_c\gamma_{\lambda_c}^2$. For gamma channels, the observed width is simply the square of the amplitude 2.129. For neutron channels, there is only one amplitude squared in the expression of the reduced width, therefore the χ^2 distribution has only one degree of freedom.

$$p(\gamma_{\lambda_n}^2 | \langle \gamma_{\lambda_n}^2 \rangle) d\gamma_{\lambda_n}^2 = \frac{e^{-y}}{\sqrt{\pi y}} dy \quad (2.130)$$

$$\text{with } y = \frac{\gamma_{\lambda_n}^2}{2\langle \gamma_{\lambda_n}^2 \rangle} \quad (2.131)$$

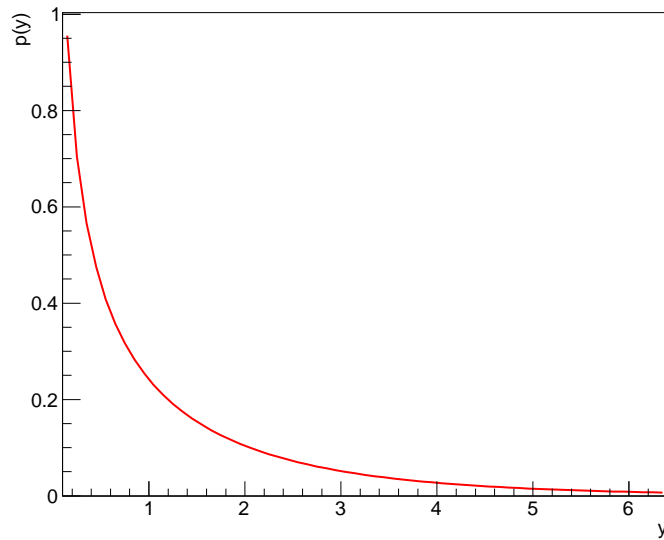


Figure 2.4: The χ^2 probability density function with one degree of freedom.

This points out the interesting fact that the more probable states in the excitation spectrum have the lowest neutron widths (figure 2.4), therefore they may be too narrow to be seen experimentally, and this must lead any statistical analysis of a resonant spectrum to a missing level correction, based on the assumed Porter-Thomas distribution. On the other hand, as already stated, for the electromagnetic cascade, usually a very large number of transitions amplitudes enter the sum, and a χ^2 distribution with a approximately infinite number of degrees of freedom is close to a constant distribution. Therefore, apart from the very large resonances where one can be sensitive to small variations of Γ_γ , resonance fits of (n,γ) reactions will assume a constant Γ_γ . This will lead to less correlations between the parameters

of the fit, given that the energy of the resonance is typically uncorrelated with the neutron width.

2.4.2 The Wigner surmise

The resonant states wave functions are eigenvectors of Hamiltonian operators. Therefore, the chaoticity in the wave functions must also be seen in the Hamiltonian matrix elements. If one chooses independent gaussian distributions for the matrix elements of the Hamiltonian, it generates a matrix ensemble know as the Gaussian Orthogonal Ensemble (GOE). In the case of a 2×2 matrix, the result for the level spacing distribution is exactly what had been hypothesised by Wigner in the 1950s' [60]. This Wigner "surmise" is derived assuming that the probability of finding a level spacing between D and $D + dD$ is proportionnal to dD , and hence totally independent of the previous levels in the spectrum. This leads to the distribution:

$$p(D | \langle D \rangle) dD = \exp \left(-\frac{\pi}{2\langle D \rangle^2} \int_0^D D' dD' \right) \frac{\pi}{2\langle D \rangle^2} D dD \quad (2.132)$$

$$= \frac{\pi}{2\langle D \rangle^2} e^{-\pi D^2 / \langle D \rangle^2} D dD \quad (2.133)$$

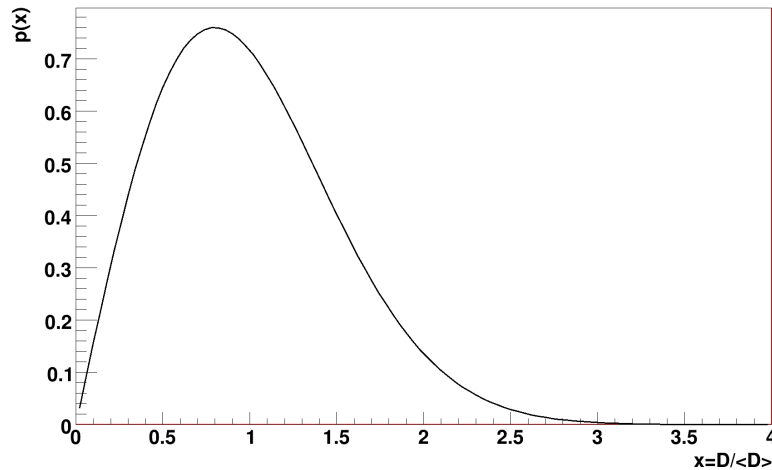


Figure 2.5: The Wigner surmise distribution.

This Wigner surmise is to be used for practical calculations and comparisons to experimental data, since it is extremely close to the actual GOE distribution, even for very large matrix dimensions.

Chapter 3

The experimental facility

This part is aimed at describing the n_TOF facility at CERN. First the PS proton beam characteristics will be reviewed, followed by a description of the spallation target and the moderator, acting as the neutron source. The experimental area will come next, with the detectors used. Finally, some experimental issues like the resolution function and multiple scattering will be mentioned. More details concerning the facility can be found in references [61] and [62].

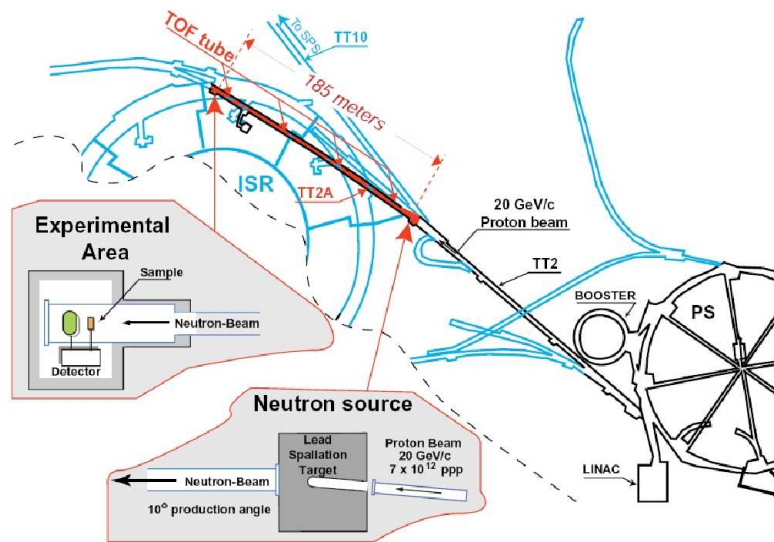


Figure 3.1: The n_TOF facility.

3.1 History of the n_TOF project

The main motivation for the n_TOF project is following Carlo Rubbia's idea of the energy amplifier [63] (from which derived the general concept of the ADS - Ac-

celerator Driven System). It is composed of a neutron source driven by a particle accelerator, feeding a sub-critical reactor. The energy provided by the accelerator is therefore amplified by the reactor, sustaining a fission chain reaction. One of the great advantages of this system is the intrinsic safety granted by the sub-critical system. Indeed if the accelerator is shut down, the reactor will come back to its primeval sub-critical state, which has no possibility of diverging. Also, the potentialities for nuclear waste transmutation and nuclear fuel regeneration (especially with the thorium-uranium fuel cycle) of this device seemed promising, but one major limitation for practical application was the poor status of nuclear data, especially in the actinide region. Also, attention was drawn at nuclear waste disposal through transmutation and incineration, for example the TARC (Transmutation by Adiabatic Resonance Crossing) project [64], but it required better accuracy on nuclear cross section data. To this end the n_TOF collaboration was born at CERN in 2000. The characteristics of the facility attracted not only nuclear reactor related studies, but also astrophysical motivations (especially nucleosynthesis processes driven by neutron capture in stars). Some fundamental aspects of nuclei can also be investigated using neutron capture, such as tests for statistical models or nuclear structure insights using gamma cascade observations from a highly excited state.

3.2 The PS proton beam

The CERN facility provides the n_TOF collaboration with bunched proton pulses thanks to the Proton Synchrotron (PS) accelerator [61]. These protons are extracted from a hydrogen source, first accelerated into a LINAC (linear accelerator) stage, up to an energy of 50 MeV, then into a four rings booster, before being injected into the PS at 1.4 GeV/ c momentum. They are then accelerated up to a momentum of 20 GeV/ c , which is the maximum reachable by the 1.2 s PS magnetic cycle. These bunches have a 7 ns r.m.s width and contain up to 8.5×10^{12} protons. The PS super-cycle of 48 s cannot contain more than 5 dedicated bunches for n_TOF, due to heat dissipation on the spallation target as well as radiation safety.

There is also a parasitic mode in which the protons are retrieved from the 24 GeV/ c bunches originally dedicated to the East Hall experimental area. These bunches have about 4×10^{12} protons. They are very useful for getting more statistics in a smaller amount of time when East Hall is not in need of protons, and their lower intensity can reduce the dead time correction factor for large resonances.



Figure 3.2: The proton beam line before the spallation target.

3.3 The spallation target

The lead spallation target used at n_TOF is cylindrical and has a 40 cm length and 60 cm diameter (see figure 3.3). It was designed for optimizing several parameters:

- Neutron flux intensity
- Energy resolution
- Size and quality of the beam in the experimental area

The target can generate up to 10 kW of heat when the maximal repetition rate is reached, and therefore has to be cooled down. This is ensured by a constant 1 cm thick water flow, at about 6 liters per second at 30 °C, so the target stays at 50 °C, without ever going above 140 °C (knowing that the melting point of lead is 330 °C). Also, the target is followed by 4 cm of borated water. The presence of boric acid in water inhibits neutron capture on hydrogen (since the capture cross section is several orders of magnitude larger for ^{10}B than for hydrogen), and therefore the gamma rays emitted from this neutron capture have a much lower energy. Indeed the neutron capture on ^{10}B gives (with a probability of 0.94):



whereas neutron capture on hydrogen will give a 2.2 MeV gamma ray. In the experimental area, this will help reduce the background induced by these in-beam

photons. The very energetic neutrons escaping the spallation target are moderated by the surrounding water, providing a neutron fluence in the experimental area that ranges from thermal energy (0.0253 eV) to several GeV.

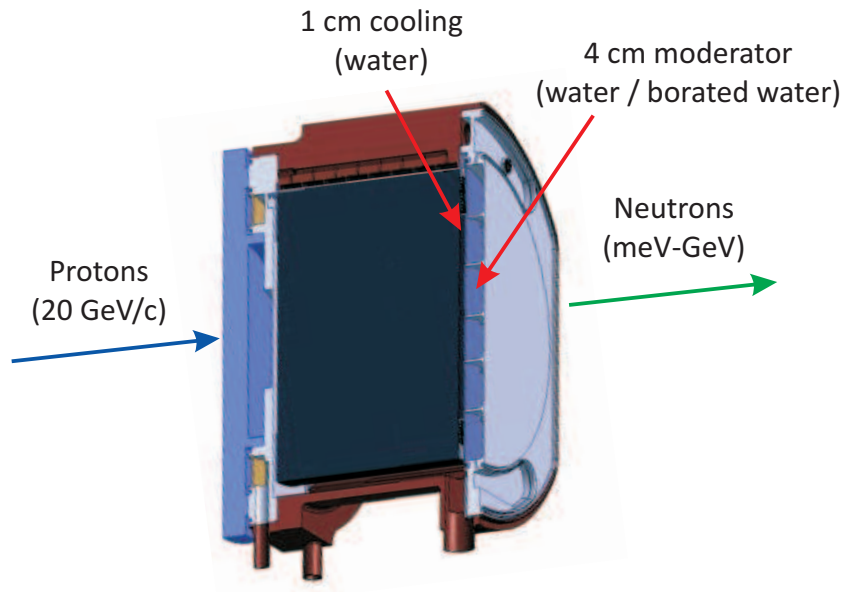


Figure 3.3: The spallation target of n_TOF[62].

3.4 The tunnel

The tunnel is 182.3 m long from the spallation target to the experimental area. Including the escape line, it is 200 m long in total, and is made up of three sections:

- The first one is 70 m long and has a 80 cm diameter.
- The second one is 68.4 m long and has a 60 cm diameter.
- The last one is 61.4 m long and has a 40 cm diameter.

There is a first collimator (2 m long and 5.5 cm radius) which is 136.7 m away from the spallation target. It is called “Source Screening Collimator” (SSC), and acts as a shield against the neutron source. It effectively reduces the radial spread of the beam and the number of neutrons hitting the second collimator. It is composed of both metal and concrete for an efficient scattering of the intercepted neutrons. Another collimator at 178 m (2.5 m long, 0.9 to 4 cm radius) is called “Beam Shaping Collimator”. As its name suggests, it is for the most part responsible for the overall shape of the neutron beam. For capture experiments it has a 0.9 cm

radius, whereas for fission measurements the radius is usually increased up to 4 cm, so that more neutrons can reach the sample. Indeed, the fission dedicated samples are often very thin in order to let the fission fragments escape more easily. In order to avoid any background, it is composed of 0.5 m of borated polyethylene that will absorb slow neutrons, then 2.25 m of metal to scatter and slow down the fast neutrons. Finally, another layer of 0.75 m of borated polyethylene absorbs the moderated neutrons.

At 145.4 m, a dipole magnet is in charge of deviating any charged particle in the beam coming from the spallation (especially protons and pions).

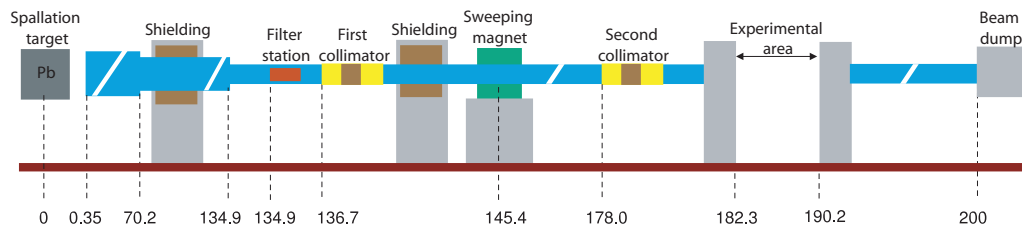


Figure 3.4: The n_TOF beam-line[62].

Each reduction of the tunnel diameter is shielded by iron, while 3 m wide concrete walls are placed behind the collimators. Finally, 3 m of iron just after the magnet shield the experimental area from muon induced background.



Figure 3.5: The dipole magnet sweeps the charged particles off the beam.

3.5 The experimental area

In the experimental area, neutron monitors (silicon detectors and MicroMegas chambers) are used to obtain the incoming flux on the sample, and in the case of capture experiments, scintillating systems are used for gamma detection.

3.5.1 The MicroMegas detectors

Two micro-bulk MicroMegas detectors [65] are used as neutron monitors in the n_TOF experimental area. The principle is simple. Neutron induced nuclear reactions on a converter emit charged particles that ionize the gas in the chamber. The electrons are accelerated, multiplied and collected to give a pulse. In the case of n_TOF, the two converters used are ^{235}U (with the fission reaction) and ^{10}B (with (n, α) reaction). The use of several converters is compulsory since no reaction cross section is standard on the whole energy range (from 0.0253 eV to a few hundreds MeV). Typically, the ^{235}U converter is not used at intermediate energies (between 1 eV and 3 keV) because of the presence of resonances that increase the uncertainty on the reaction rate.

3.5.2 The silicon monitors (SiMON)

An assembly of four silicon detectors [66] is also used for neutron counting. It is placed off beam and detects the α and ^3H particles emitted by the $^6\text{Li}(n,\alpha)$ reaction on a LiF deposit. The deposit is placed on a 3 μm mylar layer (6 cm diameter) in the beam. The combination of all the monitors gives a rather accurate evaluation of the neutron spectrum from the thermal point to about 1 GeV.

3.5.3 The C_6D_6 detectors

In order to detect the gamma rays emitted after neutron capture, several criteria have to be met.

- The detector has to be fast, *i.e.* the mean time between two events must be much larger than the duration of the detector's response.
- It has to be as insensitive to neutrons as possible, for an optimal background reduction.
- It must also recover fast from the gamma flash created in the spallation process.

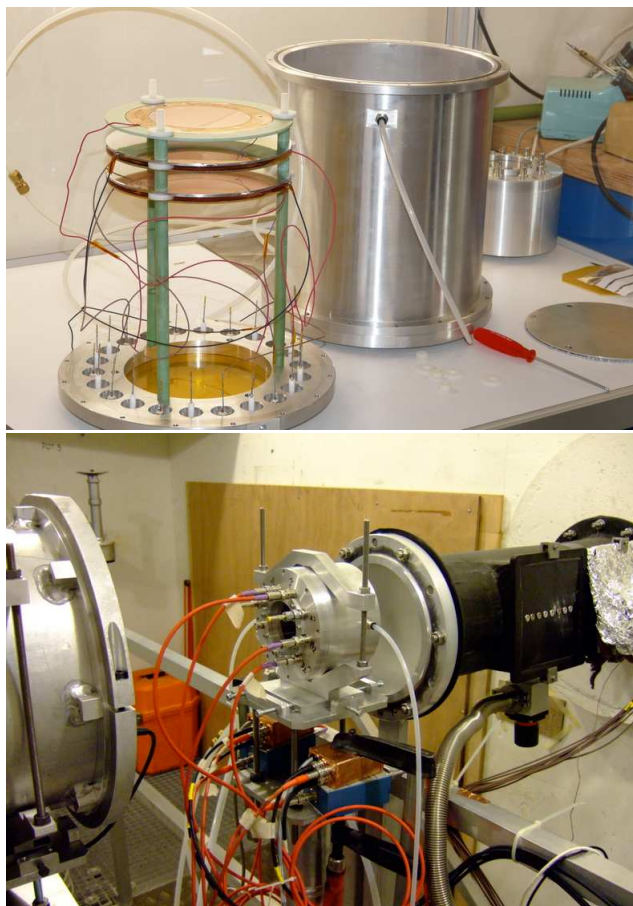


Figure 3.6: The Micromegas detector. Top: disassembled. Bottom: in the beam.

- The energy resolution has to be good enough for a proper calibration.

The rapidity of the response is best for scintillating detectors, and the C_6D_6 liquid ensures a very low neutron sensitivity. Indeed the neutron capture on deuterium is much lower than on hydrogen, but the scintillating properties of methane are conserved. The photons produced during the scintillation process go through several stages of photo-multiplication before the charge created by a photo-cathode is collected. The full width at half maximum of a pulse is 10 nanoseconds. In n_TOF, a pair of C_6D_6 detectors is used, to ensure minimal neutron sensitivity. However obtaining the detection efficiency of one gamma cascade is not straightforward, since the efficiency to a single gamma ray is very low. See section 4.5 for details on the pulse height weighting procedure.

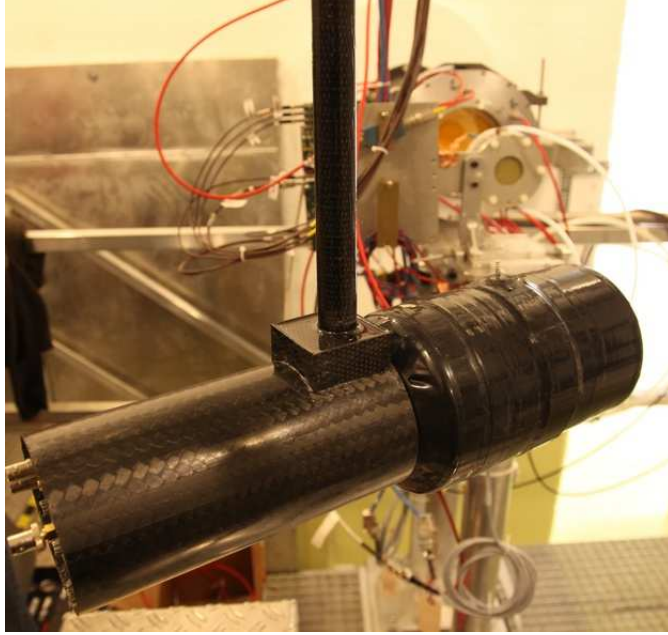


Figure 3.7: A C₆D₆ detector.

3.5.4 The TAC

Another scintillating system used at n_TOF is the Total Absorption Calorimeter (TAC) [67]. It is made up of 40 BaF₂ scintillating crystals, arranged in a spherical geometry, so that 4π of solid angle are covered. Unlike the C₆D₆, this detector is quite sensitive to neutrons and to the gamma flash. The latter prohibits the analysis of time of flight data after approximately 30 keV. However, it has a much better energy resolution and a high efficiency to gamma rays. Finally, the 4π geometry allows one to investigate other observables, such as the photon multiplicity.

3.6 The characteristics of the facility

3.6.1 The time of flight technique

The principle of time of flight spectrometry is rather simple. A neutron is created in the spallation target at time t_s , and captured in the sample at time t_n . One can assume that the time between neutron capture and gamma detection is negligible, since the lifetime of a compound nuclear state is of the order of 10^{-15} s, and the detectors are placed less than one nanosecond away from the sample (at the speed of light). Hence the time of flight T is defined by:

$$T = t_n - t_s \quad (3.2)$$

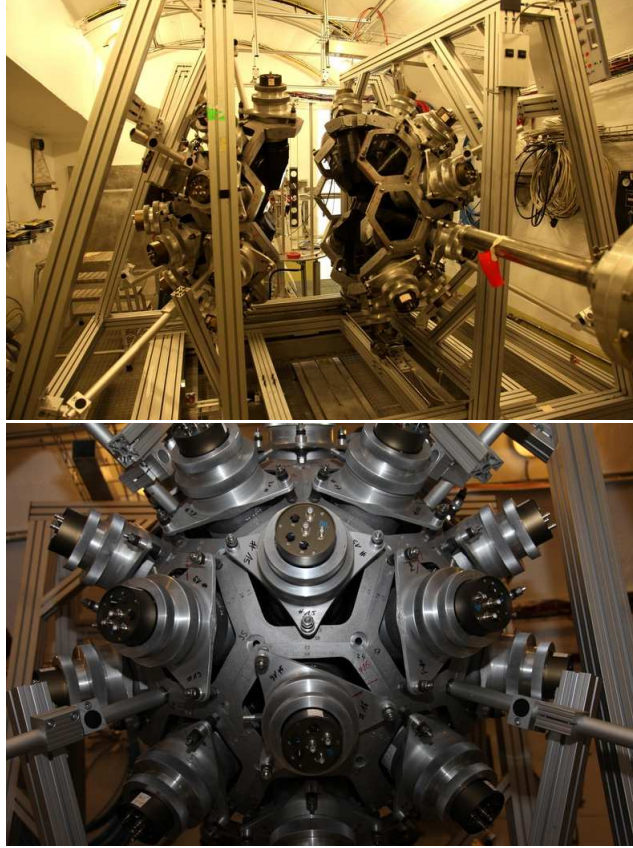


Figure 3.8: At the top, the TAC is opened for sample replacement. In the bottom, it is in a closed configuration.

Then the neutron kinetic energy E_n is given by:

$$E_n = (\gamma - 1)m_0c^2 \quad (3.3)$$

with γ being the relativistic Lorentz factor ($\gamma = \frac{1}{\sqrt{1-v^2/c^2}}$), and m_0 the rest mass of the neutron ($m_0c^2 = 939.565$ MeV). Although t_n is immediately given by the time of gamma detection, t_s is less straightforward to obtain. A more robust way than relying on the proton pickup is to wait for the so-called gamma flash to reach the experimental area. Indeed, the spallation produces many more particles than simply neutrons. Gamma rays and heavy charged and neutral particles are also created. Although the charged particles are gotten rid of thanks to the sweeping magnet, the gamma rays still reach the experimental area much faster than the neutrons. This is easily detected by the scintillators at a very early time of flight, and constitutes a calibration point. Let t_γ be the time of detection of the gamma flash. Then:

$$t_s + \frac{L}{c} = t_\gamma \quad (3.4)$$

with L being the flight path between the spallation target and the detectors. Finally, assuming a very low neutron kinetic energy relative to its mass (typically below 1 MeV):

$$E_n = \frac{1}{2} \times m_0 \times \left(\frac{L}{t_n - t_\gamma + \frac{L}{c}} \right)^2 \quad (3.5)$$

3.6.2 Data acquisition

The electronics setup is based on flash ADC (Analog to Digital Converter), with Acqiris digitizer cards. The signal amplitude coming from the detectors is coded with 8 bits, giving 256 possible values. For every acquisition window (*i.e.* every proton pulse), 48 MBytes of data is received, with a sampling frequency of 500 MHz, hence one point every 2 ns. When the beam is on, the acquisition is triggered by the PS, whereas a separate triggering mode is used for calibration runs (*i.e.* with no beam). Each acquisition window lasts for:

$$\frac{48 \text{ MSamples}}{500 \text{ MHz}} = 96 \text{ ms} \quad (3.6)$$

corresponding an equivalent neutron energy of 0.019 eV. An amplitude threshold of -13.8 mV was used, together with a "zero suppression" technique. Every recorded signal below the threshold is fitted to a reference shape in order to extract the amplitude and time of flight, which are stored in DST (Data Summary Type) files. These data files are later converted into ROOT trees for the analysis. More details concerning the DAQ can be found in [68].

3.6.3 Extracting the capture yield

For each neutron at energy E_n reaching the target, there is a certain probability $Y(E_n)$ for a (n,γ) reaction. This probability is expressed by the ratio of the (n,γ) reaction rate $C(E_n)$ and the neutron flux on the target $\phi(E_n)$.

$$Y(E_n) = \frac{C(E_n)}{\phi(E_n)} \quad (3.7)$$

In practice, however, the number of (n,γ) observed reactions $C_{\text{obs}}(E_n)$ contains some background $B(E_n)$ that needs to be subtracted. Also, the detection efficiency to gamma rays $\epsilon(E_n)$ of the gamma cascade needs to be corrected for. Assuming it is only depending on the neutron energy (see sections 4.5 and 4.11 for details on the data processing using a weighting function and final normalization), the capture yield becomes:

$$Y(E_n) = \frac{C_{\text{obs}} - B(E_n)}{\phi(E_n) \times \epsilon(E_n) \times N} \quad (3.8)$$

with absolute normalization constant N . Also, the neutron fluence on the target is never measured directly, one only has access to the total fluence in the beam going through the silicon and MicroMegas detectors. Hence it has to be renormalized to take into account the beam interception factor, labeled $I(E_n)$.

$$Y(E_n) = \frac{C_{\text{obs}} - B(E_n)}{I(E_n) \times \phi_{\text{obs}}(E_n) \times \epsilon(E_n) \times N} \quad (3.9)$$

Finally, if one neglects multiple scattering effects, this capture yield is related to the reaction cross sections through the following formula:

$$Y(E_n) = \left(1 - e^{n\sigma_t(E_n)}\right) \times \frac{\sigma_{n,\gamma}(E_n)}{\sigma_t(E_n)} \quad (3.10)$$

where n stands for target nucleus density (in atoms per barn), and σ_t , $\sigma_{n,\gamma}$ the cross sections for total and (n,γ) reactions respectively. The first term in equation 3.10 is called self-shielding, and gives the probability for any reaction to occur in the target, whereas the second term is the probability of a (n,γ) reaction being measured, given a reaction has occurred.

3.6.4 The neutron energy resolution

The first correction to apply to the capture yield obtained in equation 3.9 is related to the uncertainty on the measured neutron energies. Indeed, due to scattering in the thick spallation target and the moderator, or proton pulse width, two neutrons with the same energy may arrive in the experimental area with different times of flight. The main sources of uncertainty are:

- The width of the proton bunch (≈ 7 ns).
- The uncertainty on the flight path L :
 - Uncertainty on the distance between the spallation target and the sample.
 - Uncertainty on the moderation distance as a function of neutron energy.
- The duration of the detector's response.

The uncertainty on the distance between the neutron source and the sample will be given by a fit of a standard resonance on ^{197}Au (see section 4.8), and will be found to be less than 10 cm. The main objects of concern for resolution broadening are the proton pulse width, the moderation distance, and Doppler broadening, which merely expresses the fact that the target nuclei have a certain distribution of kinetic energies at thermal equilibrium, which adds to the uncertainty of reaction relative kinetic energy, and will broaden the widths of the resonances. Figure 3.9 shows

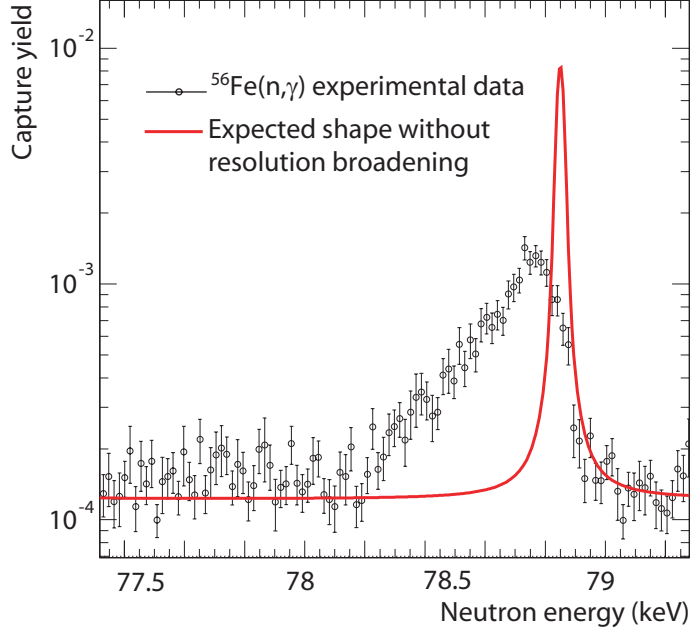


Figure 3.9: The effect of the resolution function [62]. The red line is the expected Doppler broadened resonance.

the effect of the resolution on a ^{56}Fe resonance.

One can easily notice that the broadening is asymmetric, which changes not only the shape, but also the peak position. During n_TOF's so-called phase I, an analytic form of the resolution function was adjusted to MCNP [69] and FLUKA [70] simulations, and is now implemented in the SAMMY R-matrix code [71]:

$$\text{RF}(t) = A_0 \frac{(t + \tau)^2}{2\Lambda^3} + A_0 A_1 \left(A_2 e^{-A_3(t+t_0)\sqrt{E}} + A_4 e^{A_4(t+t_0)\sqrt{E}} \right) \quad (3.11)$$

Figure 3.10 shows the contributions of every component (proton pulse width, Doppler broadening, and moderation length broadening), superimposed with observed ^{241}Am resonances, and average s -wave level spacing.

However since the replacement of the spallation target and the beginning of Phase II, the resolution has worsened, especially due to the presence of aluminium windows between the cooling and moderator circuits. Although the parameterization of equation 3.11 is still a relatively good approximation, it is now possible to include a numerical resolution function in SAMMY.

3.6.5 Multiple scattering

Another important experimental effect is the multiple scattering in the sample. In addition to the self-shielding effect, which expresses the attenuation of the neutron

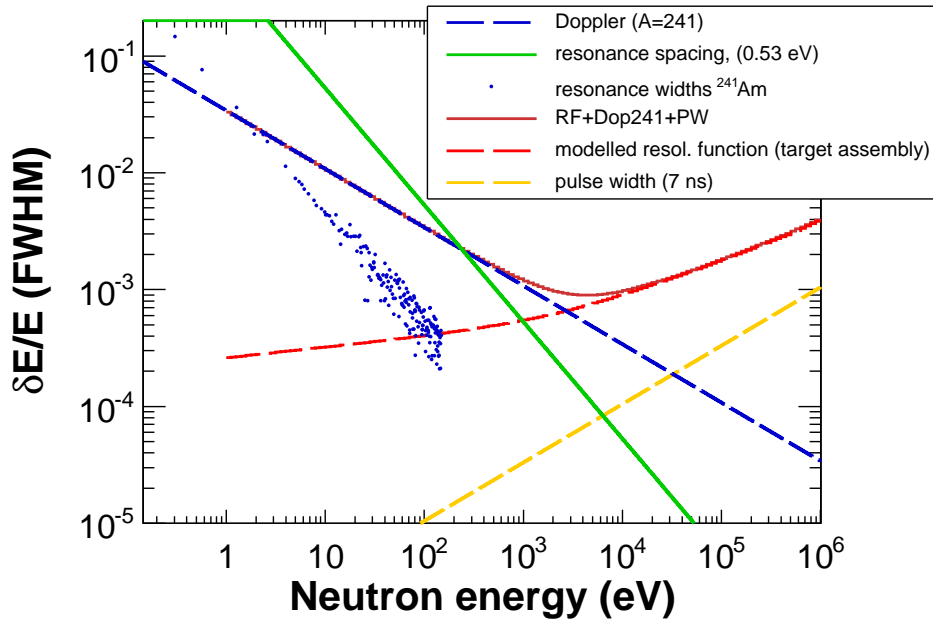


Figure 3.10: Decomposition of the total broadening into proton pulse width, Doppler broadening and moderation length distribution.

density with the distance in the sample, neutrons can also scatter once or more in the sample before they get captured. This will have the major effect of increasing the capture yield, and generally change the shape of the resonance peak. A multiple scattering correction is included in SAMMY, however it does not take into account the presence of aluminium canning (say) around the sample, since this is going to be a subtracted background. Therefore any scattering from the Am sample to the canning (and vice-versa) will not be taken into account properly. Figure 3.11 shows the capture yield measured at n_TOF of the 4.9 eV resonance on ^{197}Au , which is also calculated by SAMMY with and without multiple scattering, on a 250 μm thick sample.

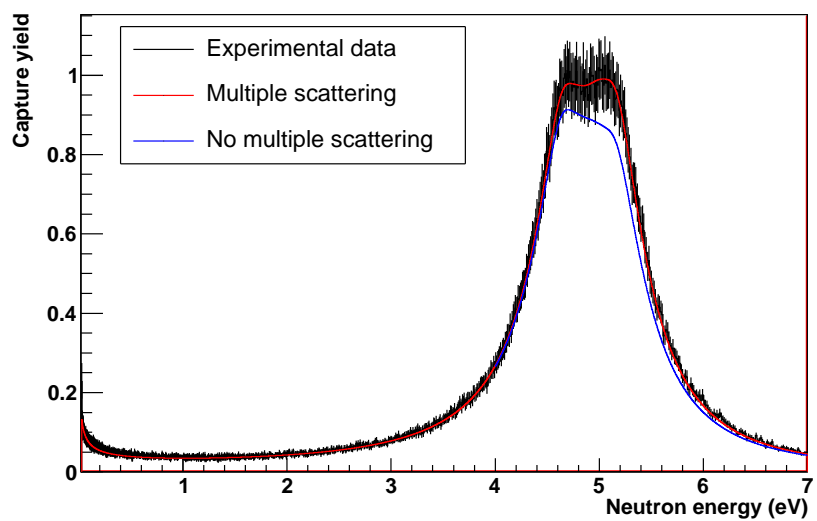


Figure 3.11: The effect of multiple scattering on the capture yield of ^{197}Au at 4.9 eV.

Chapter 4

The analysis

4.1 Experimental setup

For the ^{241}Am measurements campaign, the TAC as well as two C_6D_6 detectors were used, however this analysis will be restricted to the C_6D_6 data. Figure 4.1 shows a sketch of the experimental setup implemented in MCNP.

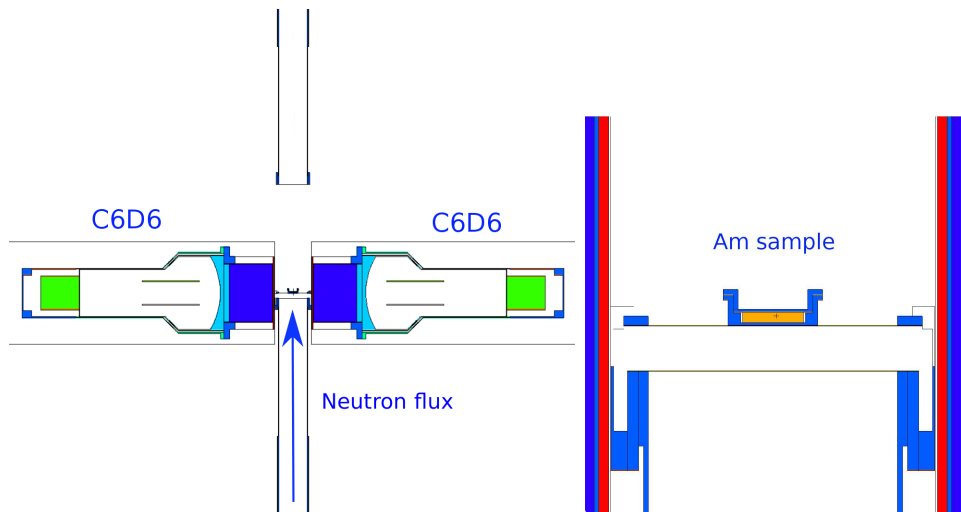


Figure 4.1: MCNP implementation of the setup at the end of the flight path. Left panel: overall view. Right panel: zoom on the sample.

4.2 Sample characteristics

The sample is made of a 342 mg Al_2O_3 matrix mixed with 32.2 ± 0.7 mg of AmO_2 [72]. It has a 1.226 cm diameter and is canned in aluminium [73][74] (figure 4.2). It has a total density of 8.59×10^{-3} at/barn, and a ^{241}Am density of 6.81×10^{-5} at/barn.

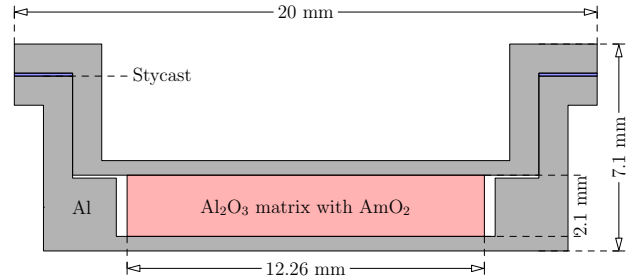


Figure 4.2: The Am sample.

Table 4.2 gives an overview of all the other samples used during this measurement.

Table 4.1: Characteristics of the sample.

	Mass (g)	Density (at/b)
Al (Al_2O_3)	0.159	3.02×10^{-3}
O (Al_2O_3)	0.142	4.53×10^{-3}
Am (AmO_2)	32.2×10^{-3}	6.81×10^{-5}
O (AmO_2)	4.28×10^{-3}	1.36×10^{-4}

Figure 4.3 shows an x-ray picture of the Am and dummy sample, which is intended to be the same sample without the Am content.

Also, a very noticeable aspect of the sample is its activity. It's responsible for approximately 3.8 GBq with an equivalent dose of 2.3 mSv/h at 10 cm distance. It caused trouble to the C_6D_6 response, and it will be detailed in section 4.3. Figure 4.4 shows two gamma spectroscopic analyses performed on a 40 mg AmO_2 sample dispersed in a Al_2O_3 matrix, performed by high precision Ge detectors [75]. In particular, the very intense 2235 keV peak is caused by the decay of ^{30}Si formed by (α, p) reaction on ^{27}Al present in the canning, and will be responsible for a lot of background. Below 400 keV, the gamma rays are due to the decay of ^{233}Pa , a daughter nucleus of ^{237}Np , the main impurity present in the sample (which is itself the daughter nucleus of the ^{241}Am through α decay). Higher energy gamma rays are mostly produced through α induced reactions on ^{27}Al . Also, some ^{240}Pu is present in the sample, as seen on figure 5.1 where the 1.05 eV resonance is clearly

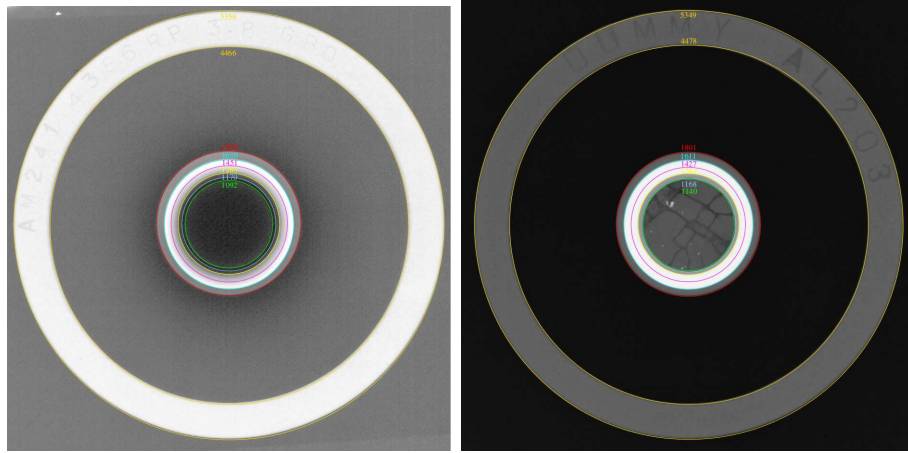


Figure 4.3: The Am sample (left) and the dummy sample (right).

Table 4.2: Samples used for the ^{241}Am measurement

Element	Sample Id	Mass (mg)	Thickness (μm)	Diameter (mm)
$^{241}\text{Am} + \text{Al}_2\text{O}_3$	116	342	2100	12.26
^{197}Au	117	114.16	50	12.20
^{197}Au thick	118	568.7	250	12.20
^{197}Au large	121	1561	50	45
Pb	119	2288	2000	12.20
Dummy	115	301	2100	12.26

visible on the capture yield. Its density was estimated to be about 7×10^{-6} of the ^{241}Am density. Note that this is only an estimation fitted on the 1.05 eV resonance, however it does not contribute enough to the capture yield to extract a precise density.

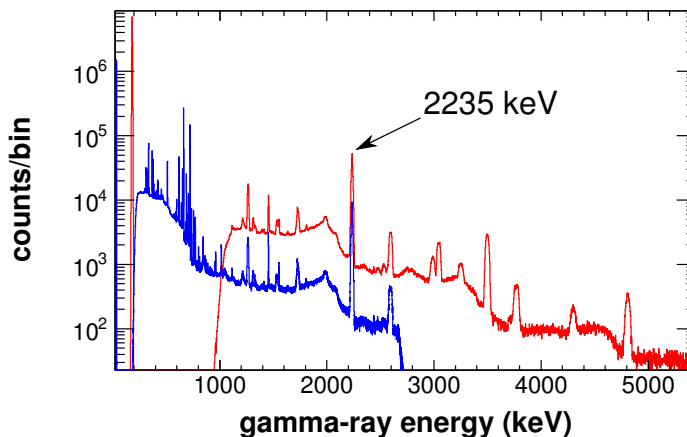


Figure 4.4: Spectroscopic analyses of the sample [75]. The two plots were obtained with different setups for exploring the full energy range from 0 to 5.5 MeV.

4.3 Run selection

Only a few days after the beginning of the acquisition, the detectors started showing significant changes in their amplitude response (see figure 4.5).

This was interpreted as a consequence of the too high counting rate induced by the 3.8 GBq activity, which caused the photo-multipliers' response to fail. This interpretation was validated by the observation of the detectors' output signal during one acquisition window ($\approx 10^8$ ns). It revealed lots of “dead” time intervals in which the baseline was not even fluctuating anymore (see figure 4.6). In these time intervals, it was assumed no event was possibly detected, and therefore it severely compromised the usability of these data.

The decision was then made to put in place a 2 mm thick lead shielding in front of the C_6D_6 detectors, to cut most of the 60 keV gamma rays responsible for the biggest part of the sample's activity. A MCNP simulation of the efficiency of the C_6D_6 (with and without lead) to the 60 keV gamma rays was performed. It turned out that the efficiency without lead shielding is 1.7×10^{-3} and 3.33×10^{-6} with it. At 3.8 GBq activity, it gives an equivalent mean time between two events of respectively 155 ns and 80 μs . Even without shielding, the typical duration of a pulse (≈ 20 ns) is much lower than the expected count rate due to activity (1 count every 155 ns). It points out that the problem observed (figure 4.6) certainly does not come from the acquisition itself, but perhaps from the current supply from the voltage divider.

The shielding had the major effect to stop the behaviour observed in figure 4.6. Its overall effect is mostly understandable with figure 4.7. It displays, on the left

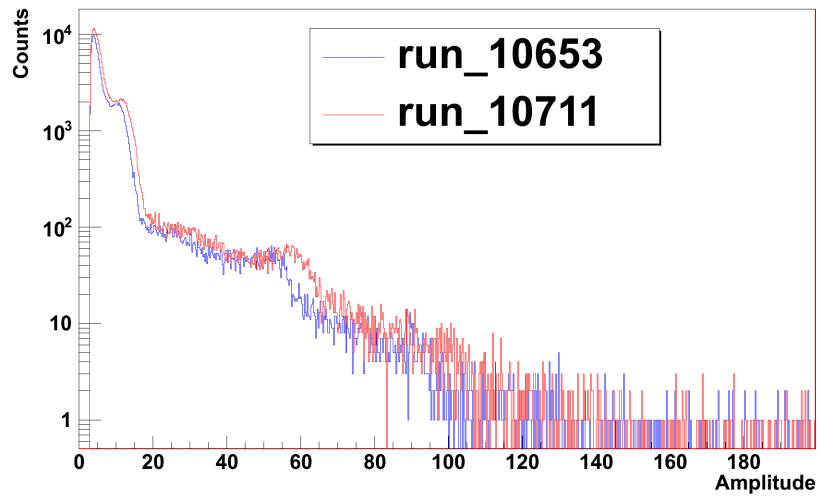


Figure 4.5: The amplitude spectra for the first and last run of the campaign.

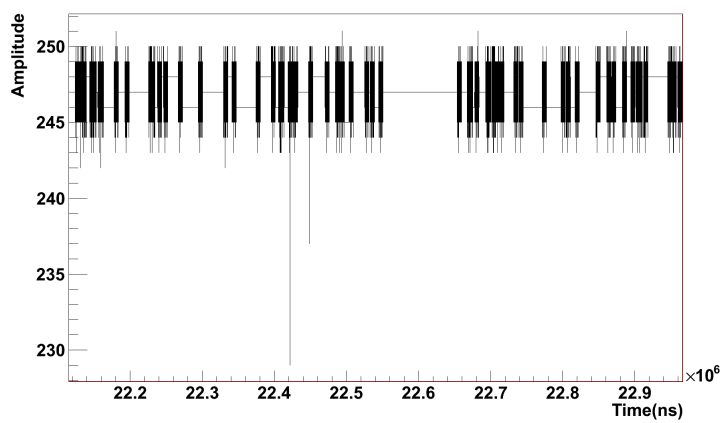


Figure 4.6: The amplitude response of the detectors with time.

hand side, the evolution of the ratio $R_{mon} = V_{mon}/I_{mon}$ with the run number (i.e. with time), where V_{mon} and I_{mon} stand for the voltage and current delivered by the photo-multipliers. The right part of the figure sketches the evolution of the current delivered by the photo-multipliers versus the assigned voltage. When the 2 mm shielding is in position, the equivalent resistance is stable, and the current fluctuations stop. That is yet another argument against the use of the data without lead.

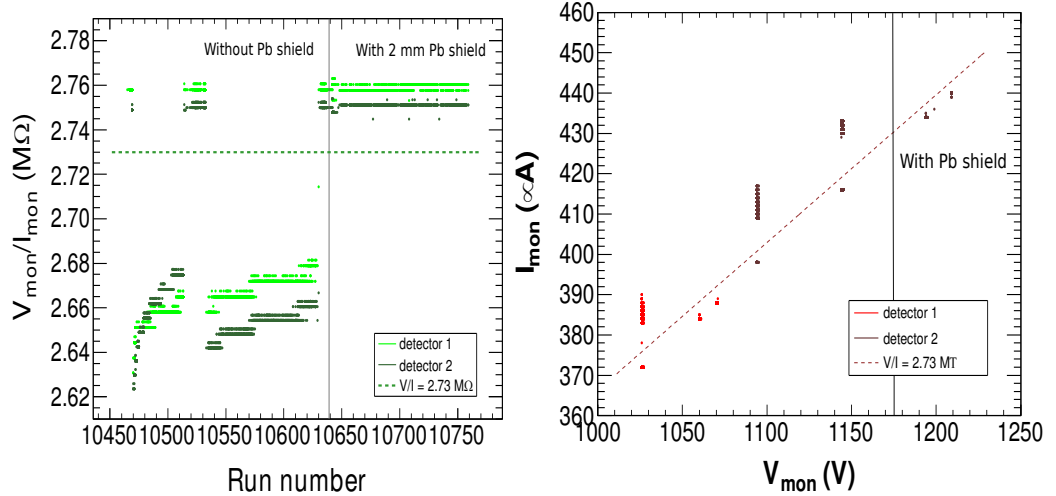


Figure 4.7: The behaviour of the detectors with and without the lead plates.

The final decision concerning the analysis was not to include the data without the lead shielding.

4.4 Data taken

In the end, 1.4×10^{18} protons were allocated for this measurement with the lead shielding. The details are given in table 4.3 [76]. 87 runs without the shielding had to be discarded.

4.5 The weighting function procedure

Recalling equation 3.9, arises the question of determining the detection efficiency $\epsilon(E_n)$. Although this notation seems to imply that it is only depending on the neutron energy, it is in general not the case. Indeed many different gamma cascades can be taken to reach the ground state (or the first isomeric state) of ^{242}Am , and for each distribution of gamma energies, there is a different total efficiency for detecting the cascade. The efficiency for detecting a gamma cascade can be

Table 4.3: Number of allocated protons for the ^{241}Am measurement and associated runs.

Sample/ Source	Beam filters	Protons ($\times 10^{16}$)	Runs						
^{241}Am	-	39.7	10653	10654	10657	10658	10659	10660	
			10662	10671	10672	10673	10674	10675	
			10701	10702	10703	10704	10705	10706	
			10707	10708	10709	10710	10711		
^{241}Am	Al, Co, W, Mo	15.0	10663	10664	10665	10666	10667	10668	
			10669	10670					
^{241}Am	Co	8.65	10727	10728	10730	10731	10732		
Au-thick	-	15.0	10679	10740	10741	10743	10744	10746	
			10747	10753	10754	10755	10748		
Au	Al, Co, W, Mo	4.87	10745	10751	10752				
Au	Co	3.37	10739	10749	10750				
Au-nocan	-	0.37	10756						
Au-thin	-	8.66	10651						
Au-45 mm	-	0.54	10757						
Pb	-	5.26	10718	10719	10720	10721			
Dummy	-	14.2	10690	10691	10692	10693	10694	10723	
			10724	10725					
Dummy	Al, Co, W, Mo	7.74	10695	10696	10697				
Empty	-	5.44	10680	10681	10682				
Canning	-	10.7	10683	10684	10685	10686	10687		
Canning	Al, Co, W, Mo	2.51	10718	10719	10720	10721			
^{88}Y	-	-	10648	10677	10699	10715	10733	10734	
			10758						
^{137}Cs	-	-	10649	10676	10698	10716	10735	10759	
Am-Be	-	-	10650	10678	10717	10736	10737	10738	
^{241}Am	-	-	10652	10661	10700	10729			
ambient	-	-	10712	10713	10714				

written as the complementary probability of missing every single photon of the de-excitation.

$$\epsilon(E_n) = 1 - \prod_{i=1}^n (1 - \epsilon_i) \quad (4.1)$$

with ϵ_i being the detection efficiency for the i -th photon of the gamma cascade. However, since the C_6D_6 detectors have low efficiency, one can expand equation 4.1 to first order:

$$\epsilon(E_n) = 1 - \prod_{i=1}^n (1 - \epsilon_i) \approx \sum_i \epsilon_i \quad (4.2)$$

The idea to simplify the problem is to make the efficiencies ϵ_i proportional to the gamma energy E_i , *i.e.* $\epsilon_i = k \times E_i$. Then:

$$\epsilon(E_n) = \sum_i \epsilon_i = k \times \sum_i E_i = k \times (S_n + E_n) \quad (4.3)$$

with S_n being the neutron separation energy in the compound nucleus. In this particular case the detection efficiency is only depending on the neutron energy. Nevertheless the relation $\epsilon_i = k \times E_i$ is not valid at all in the case of the C_6D_6 detectors. But one can express the detection efficiency to one gamma ray at energy E by the equation:

$$\epsilon(E_i) = \int_0^\infty R_i(E) dE \quad (4.4)$$

with R_i being the response function of the detector, *i.e.* the probability density of energy deposition. The idea is to find a function W verifying the relation:

$$\forall i, \int_0^\infty W(E) R_i(E) dE = k \times E_i \quad (4.5)$$

In order to accomplish that, the integral is substituted by a sum (to make it numerically accessible), and a χ^2 value is defined:

$$\chi^2 = \sum_i \frac{(\sum_j W(E_j) R(E_j) - k \times E_i)^2}{\sigma_i^2} \quad (4.6)$$

with $R(E_j)$ coming from a MCNP simulation, and σ_i being the associated numerical weight. By minimizing the χ^2 value a suitable W function is found for the analysis. In this work the function is a 4th order polynoma (fig.4.8):

$$W(E) = \sum_{i=0}^4 a_i E^i \quad (4.7)$$

where the a_i are specified in table 4.4 with a gamma energy threshold at 300 keV. The effective threshold used for event selection was taken into account in the

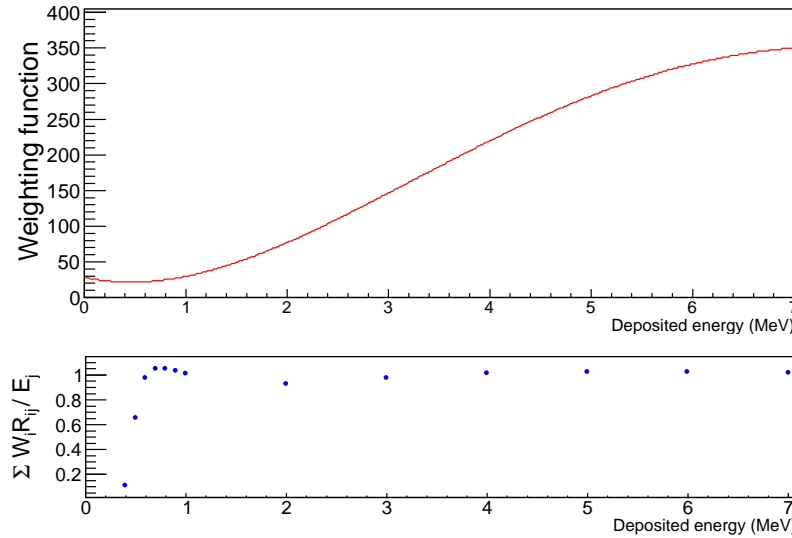


Figure 4.8: The weighting function for the Am sample with a 300 keV threshold calculated by χ^2 minimization.

weighting function calculation by setting the detectors' response to zero below the chosen threshold. Also, no negative powers were used in the polynomial.

One has to note that for the gold thick sample, an exponential attenuation of the photon source distribution was used, in order to mimic the neutron attenuation in the sample at the energy of interest (which is the 4.9 eV resonance, see section 4.11). Figure 4.9 shows the effect of an exponential attenuation of photons in the weighting function calculation on the capture yield of ^{197}Au at the 4.9 eV resonance. The difference of normalization between the two procedures is 2%.

4.6 Amplitude-energy calibration

After it was decided to keep only the data taken with the lead plates, the channel-energy calibration was simpler since the behaviour of figure 4.6 was canceled. However the amplitude spectra were still unstable over time, as shown on figure 4.5. The main effect of an incorrect calibration will be seen when the weighting function is applied, especially if the weights for certain gamma energies are large. In order to dynamically adjust the calibration, the 2235 keV photon present in the sample's background was used and tracked over time. First the traditional calibration sources (^{137}Cs , ^{88}Y and Am-Be) were used to get a resolution and calibration function for each detector. The resolution function consists of a Gaussian broadening, with the width being a second order polynoma. Figure 4.10 shows the matching of the calibration function on the four calibration gamma rays, together

Table 4.4: The weighting functions used in the analysis.

	a_0	$a_1(\text{MeV}^{-1})$	$a_2(\text{MeV}^{-2})$	$a_3(\text{MeV}^{-3})$	$a_4(\text{MeV}^{-4})$
Threshold=200 keV					
Am	11.43	-3.24	20.49	-2.81	0.11
Au (250 μm)	20.14	-21.22	34.20	-4.75	0.19
Threshold=300 keV					
Am	18.07	-12.20	24.07	-3.31	0.13
Au (250 μm)	30.66	-35.35	39.51	-5.44	0.21
Threshold=400 keV					
Am	26.77	-22.79	28.09	-3.84	0.15
Au (250 μm)	42.33	-46.56	42.68	-5.75	0.22
Threshold=500 keV					
Am	37.63	-34.68	32.13	-4.35	0.17
Au (250 μm)	56.69	-57.51	44.65	-5.82	0.22

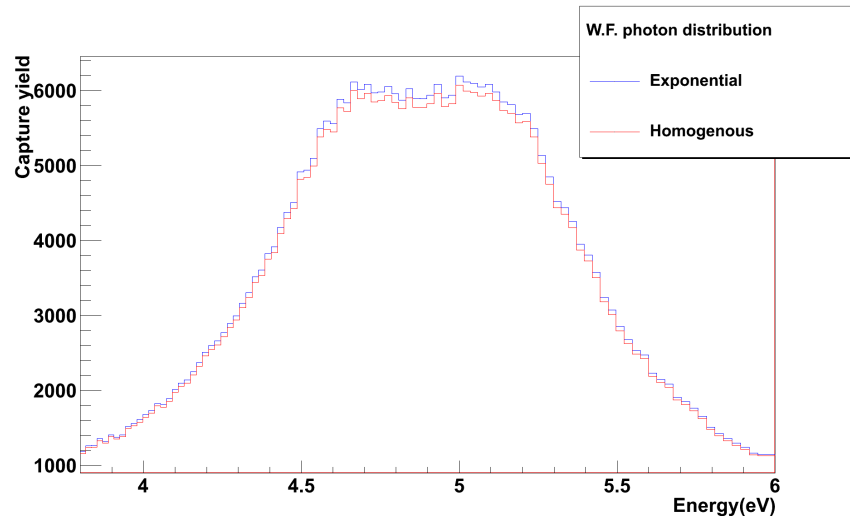


Figure 4.9: The effect of the exponential attenuation in the (unnormalized) gold capture yield.

with the 2235 keV used for dynamical adjustment.

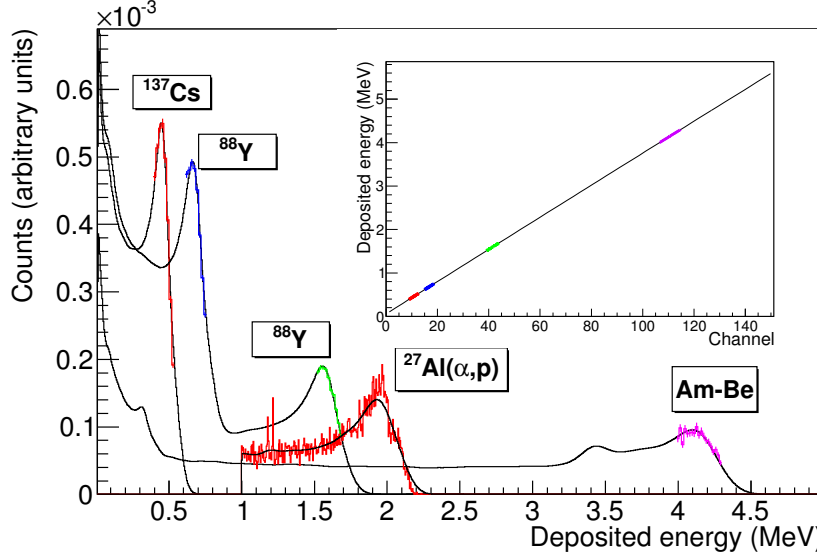


Figure 4.10: An example of calibration using the sources.

The widths found for the two detectors are:

$$\sigma_1 = 1.0376 \times 10^{-3} \times E + 7.3174 \times 10^{-4} \times E^2 \quad (4.8)$$

$$\sigma_2 = 1.6689 \times 10^{-3} \times E + 1.0005 \times 10^{-4} \times E^2 \quad (4.9)$$

with both σ and E in MeV. The calibration functions found for the two detectors are:

$$E_1 \text{ (keV)} = 57.76 + 37.19 \times A - 0.0187 \times A^2 \quad (4.10)$$

$$E_2 \text{ (keV)} = 44.66 + 35.63 \times A - 0.0179 \times A^2 \quad (4.11)$$

Then the step in the amplitude spectra around channel 60 in figure 4.5 (which is caused by the 2235 keV photon coming from the sample) was recorded over time, and the calibration was scaled accordingly for this step to match its position at the time of the calibration. Figure 4.11 compares the beam on and beam off amplitude spectra with the Am sample (where one can easily notice the 2235 keV photon Compton edge), and the beam-on spectrum with the 250 μm thick gold sample. It is worth noting that the upper deposited energy cut was applied at 6.5 MeV for the gold sample runs and 5.5 MeV for the Am sample runs, corresponding to their respective neutron separation energies. This choice for energy cuts reduces a lot the background at larger gamma energies, which is clearly visible in figure 4.11.

This work required the simulation of the deposited energy by the 2235 keV gamma

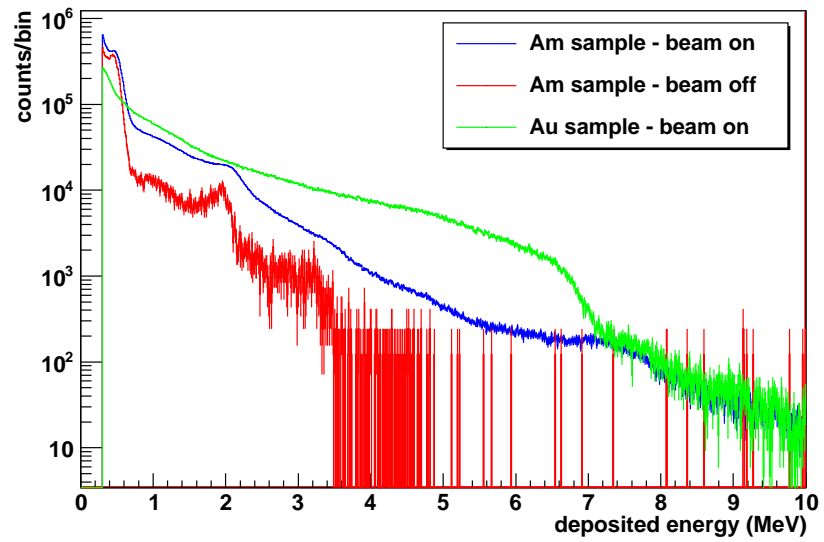


Figure 4.11: The amplitude spectra for beam on and beam off runs.

ray, similar to the simulation used for the calibration sources, and this step is shown in figure 4.10. The effect of such a scaling is shown in figures 4.12 and 4.13.

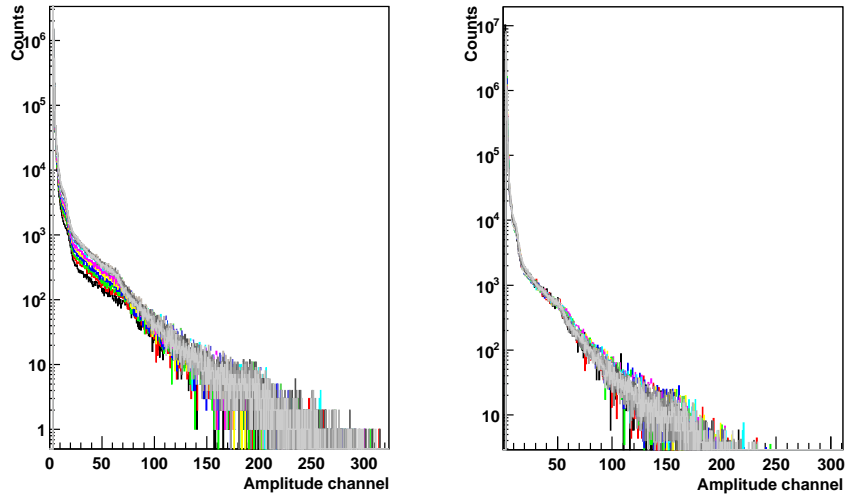


Figure 4.12: The amplitude spectra for every run (including runs without lead shielding) with and without scaling.

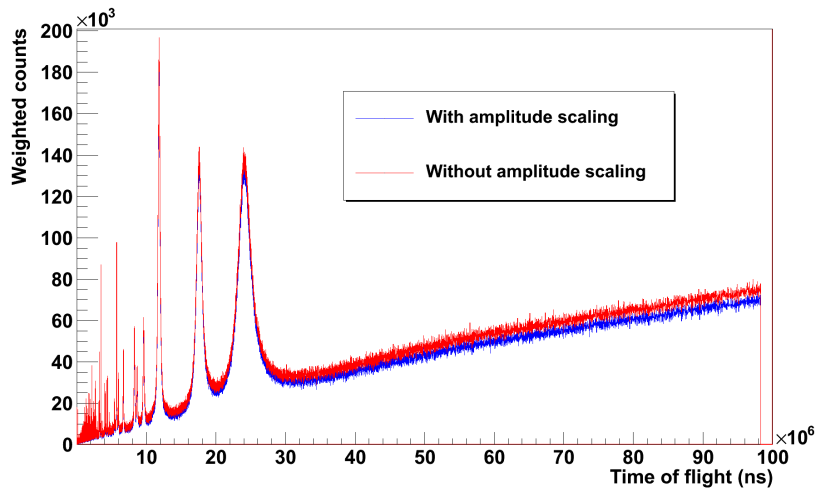


Figure 4.13: The weighted counts with and without amplitude scaling.

4.7 Event selection and processing

Although the lead plates act as a relatively effective shield against the sample's gamma rays, lots of them still reach the sample. Hence an effective threshold of 300 keV was used for event selection. However, pile-up effects can cause several 60 keV photons to be detected (i.e. triggering an event of $E > 300$ keV) if they arrive in a very short time interval. For every event above that threshold, two pieces of information are stored : the time of flight at which this event occurred, and the channel position for the energy deposition in the C_6D_6 detector. The way the counting rate histograms are filled is the following:

1. The channel position is turned into an energy deposition thanks to the calibration functions.
2. At this particular energy E , the weighting factor $W(E)$ is computed.
3. The counting rate histogram is filled at time of flight T with $W(E)$ counts.

When the whole histogram is filled, deadtime correction can be applied. The deadtime is assumed to be non extending, meaning that if every event induces a deadtime τ , a second event occurring less than τ ns after a first one will not trigger another deadtime. After the processing of the raw binary data, one can plot the time distribution between two consecutive events. It starts going down at around 20 ns (figure 4.14). Thus a fixed deadtime of 30 ns was chosen for the analysis, in order to chose events in the right hand part of the distribution, and then correct the count rate for deadtime.

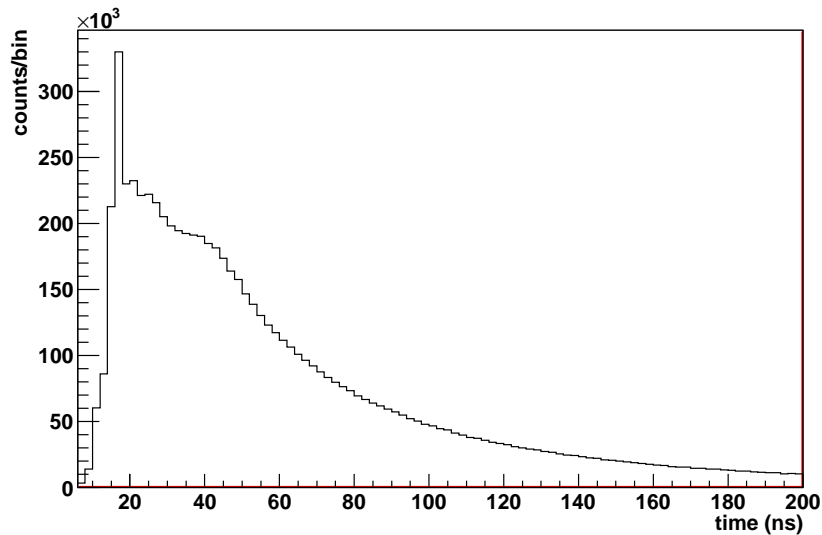


Figure 4.14: The time distribution between consecutive events.

Let us assume that the events are distributed according to a Poissonian law with a parameter λ within a time window of duration $\tau=30$ ns. The parameter λ is connected to τ through the average frequency of events f :

$$\lambda = f \times \tau \quad (4.12)$$

Then the probability for at least one event to occur within $\tau=30$ ns is given by:

$$P(\lambda) = 1 - e^{-\lambda} \approx \lambda \quad (4.13)$$

The last approximation is valid provided that $f \times \tau$ is small (*i.e.* small deadtime window and low event frequency). Furthermore, the probability of detecting an event at time T is given by the probability of the event happening times the probability of no event occurring between $T - 30$ ns and T .

$$N_{\text{obs}}(T) = N_{\text{real}}(T) \times (1 - \lambda(T)) \quad (4.14)$$

$$= N_{\text{real}}(T) \times (1 - f \times \tau) \quad (4.15)$$

Finally, if the $\tau=30$ ns window is split into bins of width dt with different values of f (and thus λ), the relation between the observed number events and the actual one is:

$$N_{\text{obs}}(T) = N_{\text{real}}(T) \times \left(1 - \sum_{t=T-\tau}^T \lambda(t) \right) \quad (4.16)$$

$$= N_{\text{real}}(T) \times \left(1 - \sum_{t=T-\tau}^T f(t)dt \right) \quad (4.17)$$

$$= N_{\text{real}}(T) \times \left(1 - \frac{1}{T_0} \sum_{t=T-\tau}^T N(t) \right) \quad (4.18)$$

where T_0 stands for the number of acquisition windows that were opened to record $N(t)$ events (with no threshold) at time t . Finally, one can wonder whether the assumption of non extending deadtime is justified. In order to check the validity of the procedure, counting rate histograms corrected for respectively 30 ns and 1000 ns deadtime were extracted. In the case of $\tau=1000$ ns (*i.e.* τ being much larger than the expected deadtime, even if extending), the extending part of the deadtime will be negligible, and it is supported by figure 4.14. Figure 4.15 shows the ratio of the corrected histograms for 30 ns and 1000 ns deadtime. Apart from statistical fluctuations, the mean value (better observed at large times of flight) stays very close to unity, and perhaps more importantly no structure coming from the resonances (where the counting rate is higher) are present. This confirms that the extending part of the deadtime correction is not relevant in this analysis. Figure 4.16 shows an example of a histogram filled with deadtime corrections with lead shielding.

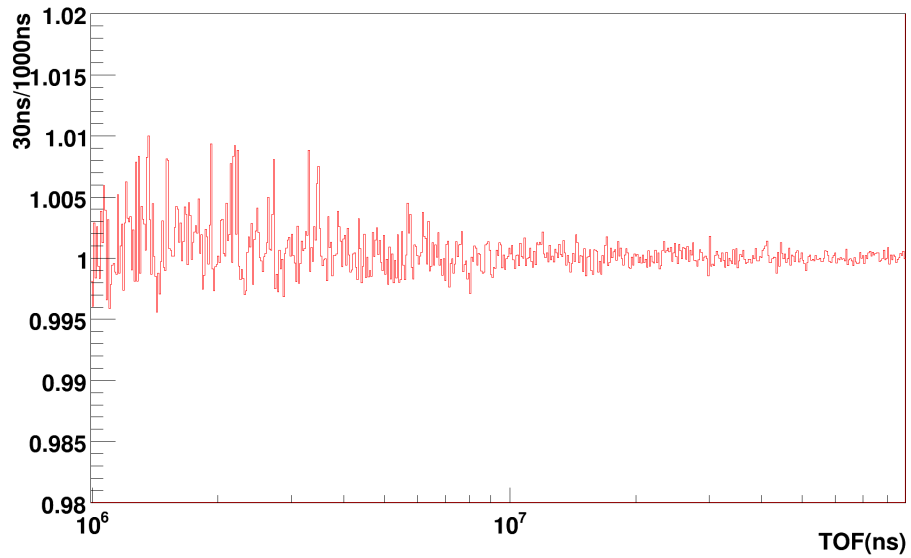


Figure 4.15: The ratio of the histograms corrected for 30 ns and 1000 ns deadtime.

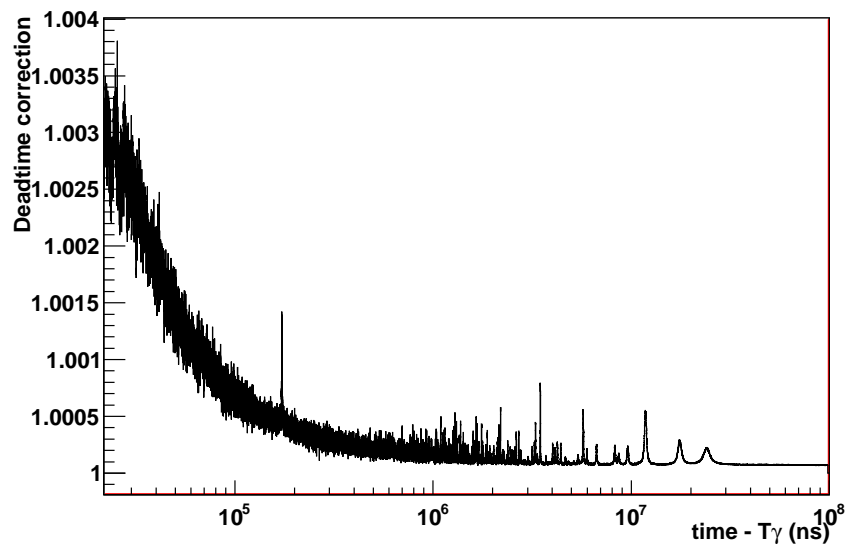


Figure 4.16: The deadtime correction for all Am runs with 30 ns deadtime.

4.8 The time-energy calibration

The time-energy relation is simply given by:

$$E_n = (\gamma - 1)m_0c^2 = \left(\frac{1}{\sqrt{1 - \frac{L^2/T^2}{c^2}}} - 1 \right) m_0c^2 \quad (4.19)$$

with L being the distance between the spallation target and the sample, and T the time of flight. However a very accurate value is needed for L , which is very difficult to get by a straightforward distance measurement. Therefore the standard resonance at 4.9 eV in ^{197}Au was used and the flight length was fitted for the measured capture yield to match a calculation.

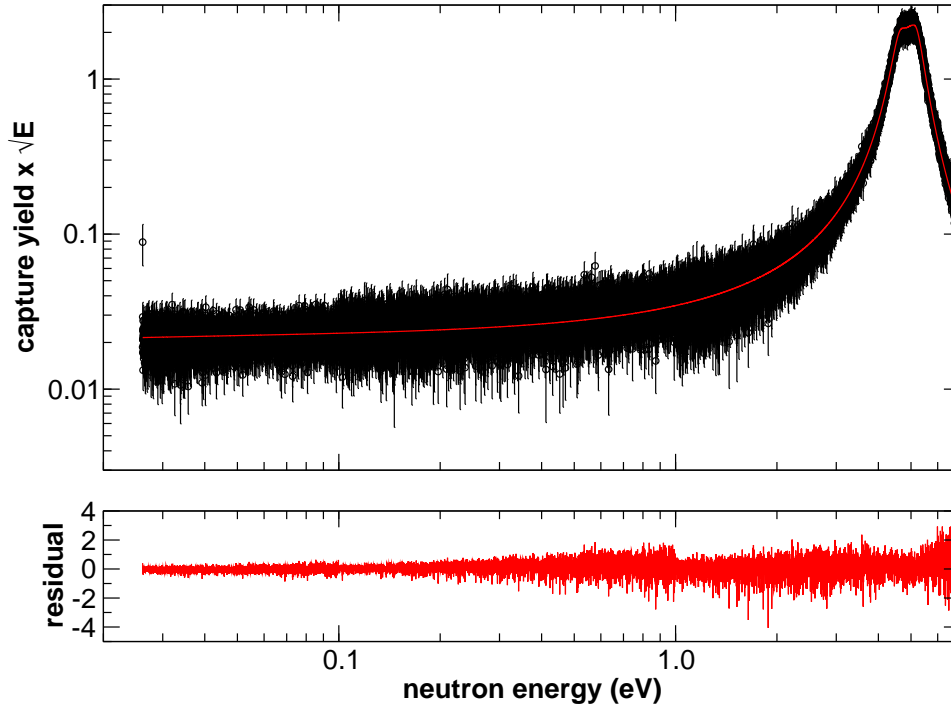


Figure 4.17: The SAMMY fit of the 4.9 eV resonance in ^{197}Au . The y axis has been multiplied by \sqrt{E} for a better observation of the low energy region. The residual is defined as the difference of the experimental data point and the fit, divided by the uncorrelated uncertainty of the data points, ignoring the uncertainty on the normalization. The uncertainties on the data points correspond to counting statistics scaled by the weighting function.

The gold capture yield was obtained on that resonance using the thick sample of gold (sample 118 in table 4.2), with the same diameter as the Am sample. This setup was preferred because of the better statistics and target thickness.

Indeed even if some uncertainty is present in the resonance parameters, using a well saturated resonance allows one to be less sensitive to the partial widths, and focus the fit procedure on the edges of the resonances, where the time to energy calibration is crucial. The SAMMY R-matrix code [71] was used to calculate the capture yield, and fit the experimental one given as an input, with only the energy position of the resonance as a free parameter. Indeed one can connect a discrepancy in energy to a correction in flight length the following way:

$$\frac{\Delta E}{E} \approx 2 \frac{\Delta L}{L} \quad (4.20)$$

if only L presents an uncertainty. The result of the fit is shown in figure 4.17 and the distance found is $L=184.21\pm 0.06$ m. The resonance parameters for the gold resonance were taken from [77]. This fit is also used to extract a normalization factor for the capture yield at 4.9 eV. This number includes both beam interception and absolute efficiency normalization. More details are given in section 4.11, especially concerning the uncertainty on the normalization factor and cross checking at thermal energy.

4.9 Observations concerning parasitic and dedicated pulses

During the measurement, many parasitic pulses were used to accumulate statistics. Although these bunches have the same energy as the dedicated ones, it is interesting to look into the details and check for any systematic difference induced by the pulse type.

4.9.1 Count rates for both types of pulses

After a separate extraction, the dedicated and parasitic count rates are plotted on figure 4.18. Everything has been normalized to its number of neutrons. It's important to stress out at this stage that a difference of about 2% in the neutron to proton ratio was observed. Table 4.5 gives the number of protons and integrated number of events in the silicon detectors, for times of flight between 10^4 and 10^8 ns, and amplitude channels between 50 and 250 (in order to restrict the analysis to the α and 3H peaks of deposited energy), for the runs with the Am sample and no filters in the beam. A minor difference in the pulse time or space distribution could account for a slightly larger neutron loss in the dedicated case on the way to the sample.

One immediately notices that the parasitic count rate is larger than the dedicated one. It is caused by the activity of the Am sample. Indeed, the activity is proportional to the number of bunches (or acquisition time), and one naturally gets more

Table 4.5: Numbers of protons received and integrated counts in the silicon detectors.

	Protons	SILI events	ratio
Dedicated	3.22×10^{17}	1.22×10^6	0.379
Parasitic	7.46×10^{16}	2.86×10^5	0.383

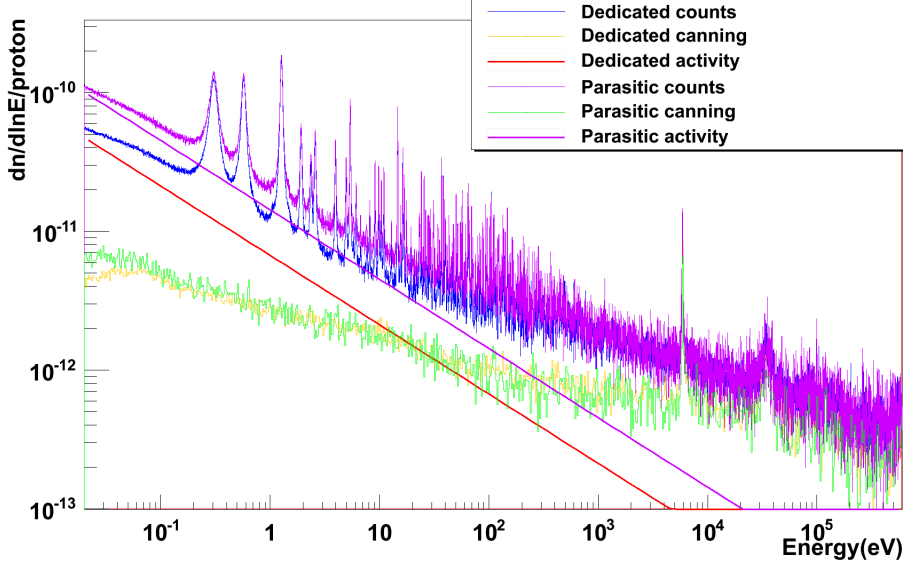


Figure 4.18: The two count rates normalized to their number of neutrons.

bunches per neutron in the parasitic case, since the intensity is lower. Therefore, the activity normalized to the number of neutrons is larger in the parasitic case. Moreover, the canning counts show a small discrepancy as well. It can be explained by the difference in ambient background normalization, since it is a contribution which is proportional to the acquisition time, just like the activity.

4.9.2 Computing the difference

Once this has been pointed out, one can try to subtract the two signals. If there is any residual and pulse-dependent background, the difference will be different from zero. In order to make the count rates per neutron comparable, one has to take into account the activity difference due to the difference in pulse intensity (figure 4.18). Let $\frac{C_i}{N_i}$ be the number of total counts per neutron for pulse type i and $\frac{C_i^{\text{Act}}}{N_i}$ the activity measured for runs of pulse type i , normalized to the number of neutrons of same type. Then, if one assumes that all captures components are proportional to the number of neutrons, they will vanish in the difference, and all

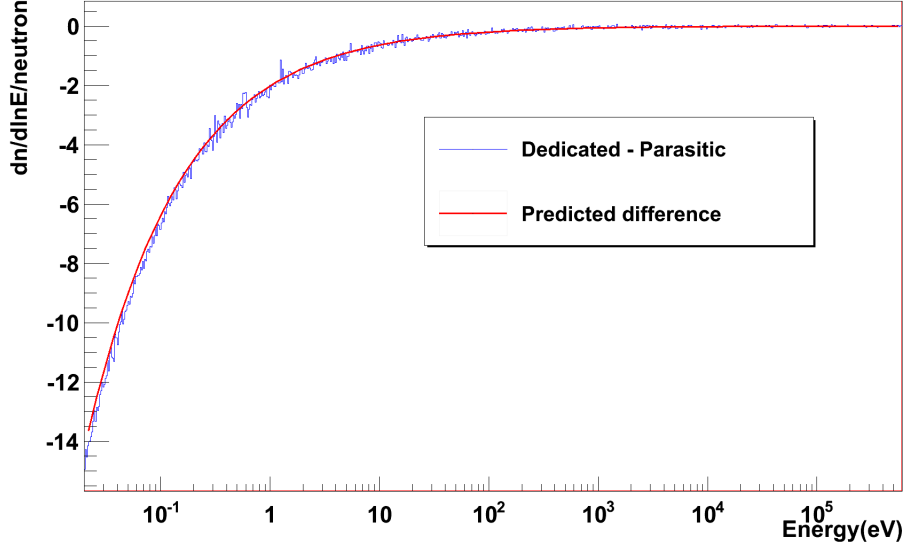


Figure 4.19: The hypothesis of equation 4.22 is tested.

that will remain is the activity difference:

$$\frac{C_{\text{dedi}}}{N_{\text{dedi}}} - \frac{C_{\text{para}}}{N_{\text{para}}} = \frac{C_{\text{dedi}}^{\text{Act}}}{N_{\text{dedi}}} - \frac{C_{\text{para}}^{\text{Act}}}{N_{\text{para}}} \quad (4.21)$$

$$= \frac{C_{\text{dedi}}^{\text{Act}}}{N_{\text{dedi}}} \left(1 - \frac{N_{\text{dedi}} \times T_{\text{para}}}{N_{\text{para}} \times T_{\text{dedi}}} \right) \quad (4.22)$$

$$\text{since } C_{\text{para}}^{\text{Act}} = C_{\text{dedi}}^{\text{Act}} \times \frac{T_{\text{para}}}{T_{\text{dedi}}} \quad (4.23)$$

where T_i stands for the number of bunches of type i . Therefore, one has to compare the right hand term of equation 4.22 to $\frac{C_{\text{dedi}}}{N_{\text{dedi}}} - \frac{C_{\text{para}}}{N_{\text{para}}}$ in order to properly comment on the difference in pulse intensity in the activity counts.

The result of such a comparison is shown in figure 4.19, where the red line is the fitted activity normalized like in equation 4.22.

The prediction almost perfectly fits the observed difference. For the following it will be assumed that no significant pulse dependent signal exists.

4.10 Background components

4.10.1 The sample's activity

A short run was performed with only the sample in front of the detectors, and no neutrons. The activity can be expected to give a constant count rate in time,

since the half-life of ^{241}Am is ≈ 432 years (i.e. very long compared to the duration of the measurement). However it will show considerable fluctuations because of the short time given for acquisition. Then it has to be fitted in order to wash out all the experimental fluctuations. Figure 4.20 shows the fit with the experimental count rate normalized to the difference of logarithmic bin limits (the fluctuations are not seen here, the spectrum was rebinned for greater clarity, which does not change the result of the fit). Then the constant C_{act} in time becomes:

$$C(E) = C_{act} \times E^{-1/2} \quad (4.24)$$

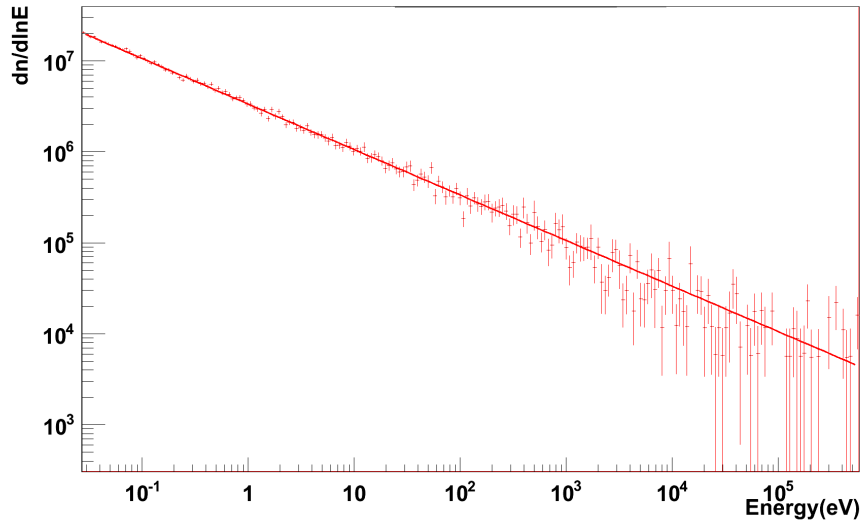


Figure 4.20: The sample's activity is fitted to wash out the experimental fluctuations.

Of course, this spectrum has to be normalized to the measurement duration. If it has to be compared to a count rate C_{Am} measured during T_{Am} , and if the duration of the activity run is labeled T_{act} , then the count rate C_{act}^N to be subtracted is:

$$C_{act}^N = \frac{T_{Am}}{T_{act}} \times C_{act} \times E^{-1/2} \quad (4.25)$$

Practically, the T_i are taken to be the number of proton bunches, each corresponding to a certain fixed time window for acquisition.

4.10.2 The aluminium canning

Neutrons can be captured inside the aluminium canning in which the sample was put. Several runs were performed with only the canning in the beam, and the

result has to be normalized to the number of neutrons received by the sample, and corrected for ambient background. The count rate C_{can}^N to be subtracted is:

$$C_{can}^N = (C_{can} - C_{amb} \times \frac{T_{can}}{T_{amb}}) \times \frac{N_{Am}}{N_{can}} \quad (4.26)$$

with N_i and T_i being respectively the number of neutrons received and number of acquisition windows open for the sample i .

4.10.3 The Al_2O_3 matrix

Neutron capture can also occur in the Al_2O_3 matrix holding the sample together. Traditionally, one uses a dummy sample made only from Al_2O_3 (and no Am) to get this contribution experimentally. This time it was tried as well but the dummy sample was contaminated with Sm isotopes, which were identified thanks to their huge resonances at low energy (see figure 4.21).

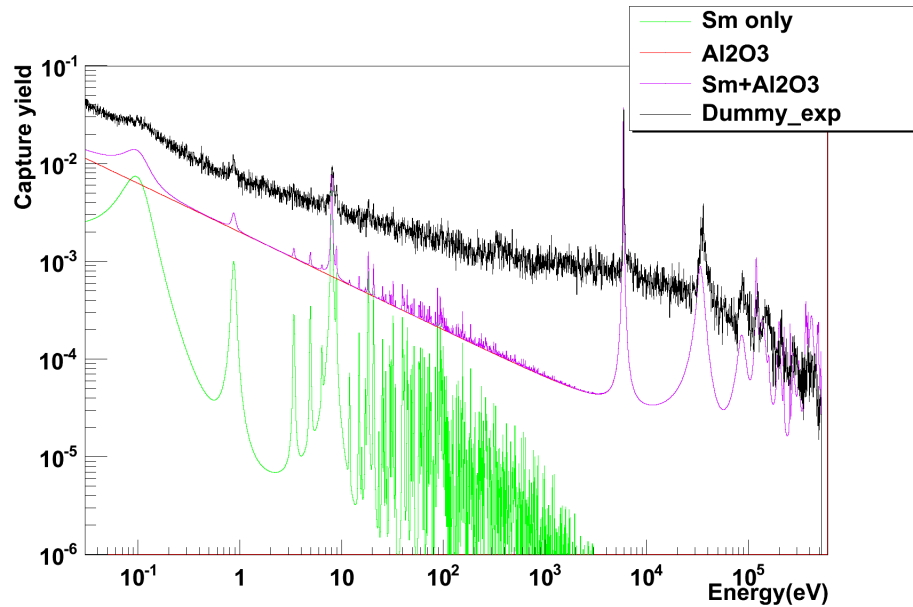


Figure 4.21: The capture yield on the dummy sample together with the expected contributions from the Al_2O_3 matrix and the Sm isotopes.

The origin of these isotopes probably comes from the stycast glue which was used to put the sample back together after it was broken. Another argument sustaining this hypothesis can be that the Sm resonances are not seen at all in the Am sample. At first it was tried to get the Sm density inside the sample by fitting the corresponding capture yield, but it was not straightforward at all due to uncertainties on resonance parameters. After noticing that the Sm contribution was

significant only below a few hundreds of eV (which is in this work the limit for the resolved resonance range), the easiest solution was to forget about this experimental information and calculate the capture yield on Al_2O_3 for the resolved resonance range analysis. It was made possible thanks to the volume and mass information available on the sample. The calculation was made with the SAMMY code [71] and resonance parameters from ENDF/B-VII.1 [18]. The uncertainty on the nuclear data on O and Al isotopes was neglected. In the unresolved range, the full experimental information provided by the dummy sample was used.

4.10.4 The neutron filters

The different neutron filters placed in the beam carry information on any residual background. The isotopes present in the filters are the natural isotopes of W, Al, Co and Mo. Table 4.6 lists the black resonances energies and filter thicknesses for each isotope.

Table 4.6: The black resonance energies and thicknesses of the filters placed in the beam.

Isotope	Thickness (mm)	Resonance energy (eV)
^{182}W	0.8	4.18
^{182}W	0.8	18.83
^{59}Co	0.25	132.0
^{27}Al	30.0	34.8×10^3

Indeed at black resonance energies, the transmission is zero and no neutrons reach the sample. Thus the only events to be detected come from other sources. Figure 4.22 shows the superposition of the counts and background with filters, with labels on each black resonance. The contribution from any remaining background seems negligible. However, a possible contribution from neutron sensitivity could still be present, assuming the scattering, moderation and capture processes happen in a very short time compared to the bin width. Thus, such background would not be visible in the filter's resonance energy.

Special care has to be taken when estimating background in the unresolved region (starting at 320 eV in this work). Indeed, although in the RRR one fits the resonance parameters on the resonance peaks, where background is usually small, in the URR, one loses the resonant structure, and thus the background level becomes a dominant source of uncertainty when averaging the spectrum. Again, the filters can be used to get an instructive insight on the possible uncertainty in background estimation. The black resonance of the ^{27}Al filter at 34.8 keV was used for this analysis, and figure 4.23 shows the spectrum with the Am sample and estimated

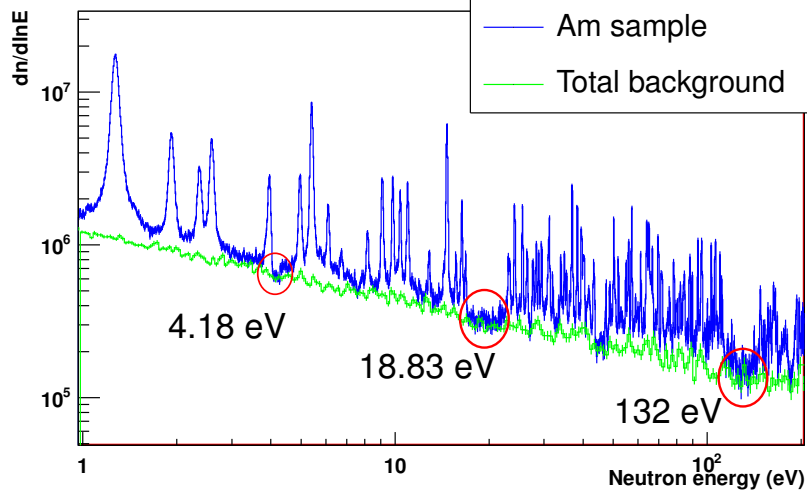


Figure 4.22: The background at every neutron filter’s black resonance in the RRR.

backgrounds in the URR with filters.

At 34.8 keV, the estimated total background is compatible with the total signal, which strengthens the analysis procedure. However, counting statistics and normalization mark the limit of this agreement.

4.10.5 Final evaluated background

All the evaluated components are shown in figure 4.24, and table 4.7 shows the normalization constants used in equation 4.27. The net capture count rate on ^{241}Am is obtained in the following way:

$$C_{\text{Am}} = C_{\text{tot}} - \left(C_{\text{can}} - C_{\text{amb}} \times \frac{T_{\text{can}}}{T_{\text{amb}}} \right) \times \frac{N_{\text{Am}}}{N_{\text{can}}} - C_{\text{Al}_2\text{O}_3} - C_{\text{act}} \times \frac{T_{\text{Am}}}{T_{\text{act}}} \quad (4.27)$$

with C_{amb} being the ambient background in the absence of sample and neutron

Table 4.7: Experimental values for number of acquisition windows (T) and integrated counts in the SiMON detectors (N), for different samples.

	Am	Activity	Canning	Ambient
N	1.50008e+06	0	416812	0
T	61714	3787	17564	13975

beam. The Al_2O_3 contribution was simulated (because of the Sm presence shown in figure 4.21) and therefore has no extra background. Concerning a possible contribution from in-beam photons, mostly coming from (n, γ) reactions in the borated

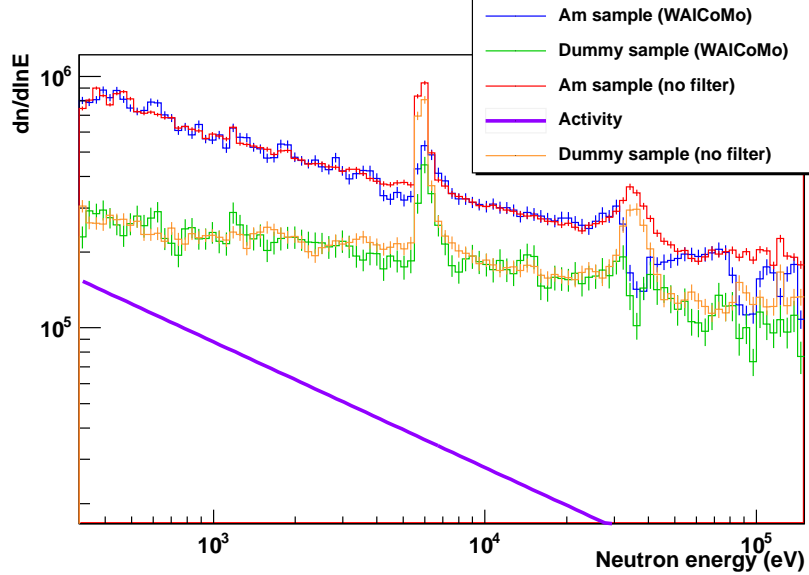


Figure 4.23: The total signal and background in the URR with the filters in the beam.

water after the spallation target), figure 4.24 shows the expected contribution, given the experimental information obtained using a natural lead sample (which only significantly interacts with photons), which was normalized to the sample's atomic number and density, and received neutron fluence. It is to be noted that the experimental information was not accurate enough to perform an actual subtraction of a well normalized photon contribution, and that the plot in figure 4.24 is for order of magnitude discussion only. However, both the study of spectra with filters and figure 4.24 show that this contribution to the total background is negligible, which is a significant improvement over the past data obtained at n_TOF, where no borated water was used to inhibit the emission of the 2.2 MeV gamma ray during the $^1\text{H}(n,\gamma)$ reaction. Also, the background level at low neutron energy is dominating the total signal. At thermal neutron energy it is about 90%, which will lead to greater uncertainties after subtraction (see section 5.2). Finally, the ^{27}Al resonances at 5.9 keV and 34.8 keV are not fully reproduced in the total signal by the canning background only. This comes from the scattering and capture contributions of the Al_2O_3 matrix, which will be fully taken into account in the unresolved resonance range by using the dummy sample, where the Sm contribution to the background can be neglected.

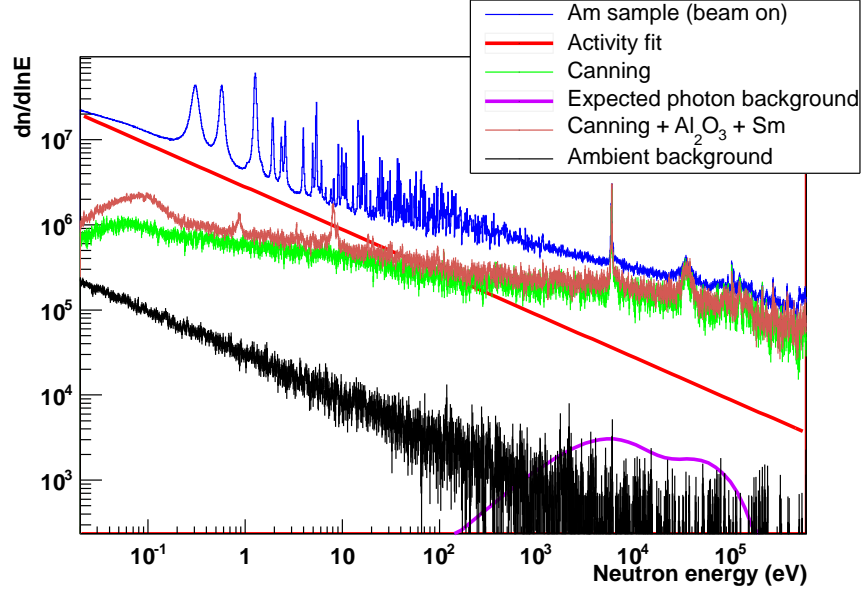


Figure 4.24: The background components of the total count rate.

4.11 Normalization

The capture yield is then obtained by dividing the net weighted capture count rate by the neutron flux and the compound nucleus excitation energy. However, the absolute value still has to be normalized. Indeed the geometrical interception of the neutron beam is not the same for the Am sample as the neutron detectors (SiMON and MicroMegs). Then the counted neutrons are different from the neutrons actually reaching the target. Also, the weighting functions were calculated thanks to simulated energy depositions in the C_6D_6 detectors, and thus an absolute normalization of the efficiency is still required. In order to account for both these steps, the ^{197}Au resonance of figure 4.17 was used once again. As the resonance parameters are assumed not to be a source of uncertainty, only the normalization is adjusted for a proper fit of the saturated 4.9 eV resonance. This normalization has to be applied back to the Am data. Finally, the beam interception factor is expected to vary with neutron energy, however neither numerical simulations nor attempts at measuring the beam profile provided the accuracy needed in this analysis. Therefore, in this work the beam interception is assumed to be energy-independent, and given by the normalization at 4.9 eV. It is to be noted that the application of an energy deposition threshold in the analysis induces an uncertainty. Indeed the part of the electromagnetic cascade located under the threshold might be different for ^{198}Au and ^{242}Am , leading to a bias in the applied normalization. No correction for this effect was applied, but it is expected that the gamma spectrum below a typical threshold of 300 keV will only account for a

negligible part of the total spectrum generated in the cascade. The numerical uncertainty on the normalization factor given by SAMMY was 1%. As a cross check of the consistency of the procedure, the results when using thick (250 μm) and thin (50 μm) gold sample were compared, and the difference was less than 1%. Also, the quality of the normalization was tested down to thermal energy, and the experimental value reproduces the standard cross section value of [78] (98.66 ± 0.14 barns) with only a 0.7% deviation. Finally, the normalizations for the two detectors were compared, and the two obtained capture yields are statistically consistent. They are shown in figure 4.25.

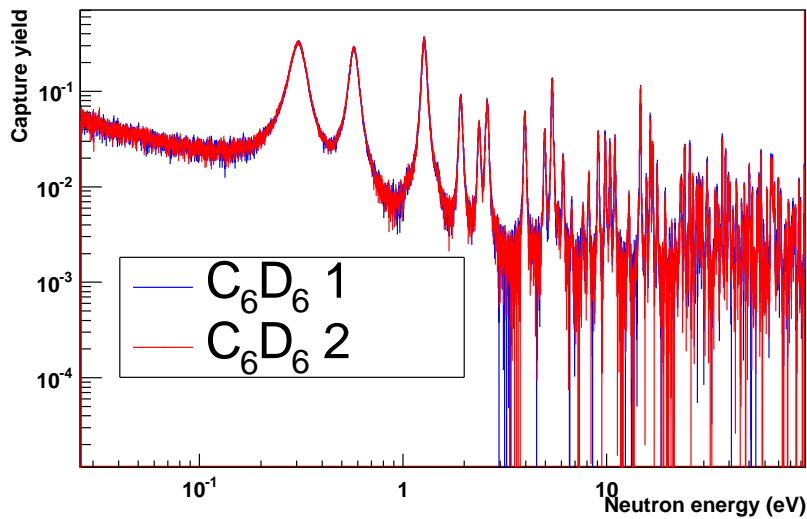


Figure 4.25: The capture yield extracted for the two detectors separately.

4.12 Neutron flux

The neutron flux for 2010 is shown in figure 4.26. It was obtained by linear combination of the data from the SiMON and MicroMegas detectors, using the appropriate detector in the appropriate energy range [79].

4.13 Capture yield

Once all the background components have been subtracted to the total count rate, the capture yield is obtained by dividing the weighted spectra by their excitation energy and the neutron flux. The normalization found with the ^{197}Au capture yield is then applied, together with the relative beam interception factor (see equation

Table 4.8: The neutron flux for the 2010 campaign.

Energy range	Detectors used
0.025 eV - 400 eV	Si+MGAS(^{10}B)
400 eV - 3 keV	Si
3 keV - 100 keV	Si+MGAS(^{235}U)
100 keV - 1 MeV	MGAS(^{235}U)

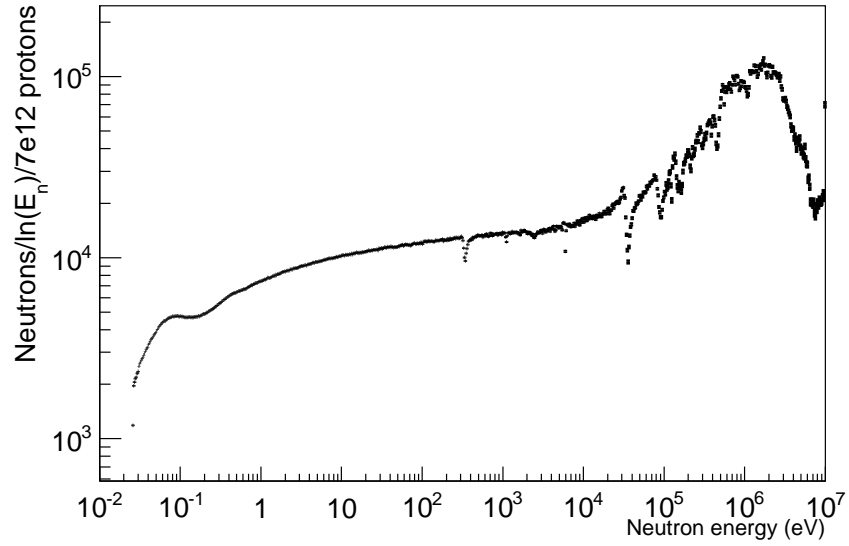


Figure 4.26: The 2010 neutron fluence [79].

3.9). The result is shown in figure 4.27. This capture yield will be given as an input for resonance analysis to the SAMMY [71] R-matrix code, with uncorrelated uncertainties.

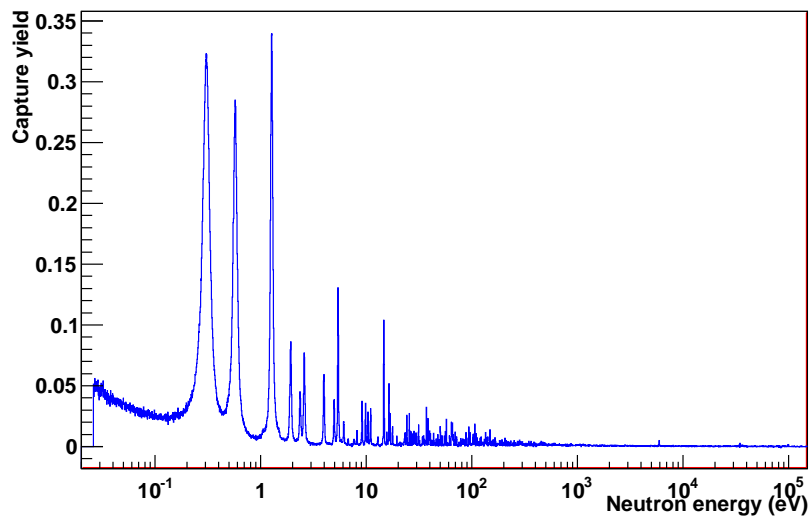


Figure 4.27: The neutron capture yield on the ^{241}Am target.

Chapter 5

Results

This chapter is focused on the physical parameters one can extract from the capture yield obtained in section 4.13. The resonances were assigned a central energy and partial widths, with the use of the R-matrix code SAMMY [71], which will be described in the first section of this chapter. The thermal cross section could then be deduced from the resonances parameters, and this will be detailed in the second section. Finally, the unresolved resonance range was analyzed, with details given in section 5.5.

5.1 The R-matrix code SAMMY

SAMMY [71] is an R-matrix calculation code developed by N. Larson, and is aimed at resonance fit and resonant cross section calculation, given a set of resonance parameters. It can calculate either yields or cross sections, and offers the choice of several R-matrix approximations, among which the Reich-Moore approximation which was detailed in section 2.3.4 and used for this work. It includes Doppler broadening corrections based on the Free Gas Model (FGM), which was used in this work, or the crystal lattice model. Also, the self-shielding and full multiple scattering corrections were included in all the calculations. Finally, SAMMY can also calculate and fit average cross sections, thanks to the FITACS module, which was used in the analysis detailed in section 5.5.

5.2 The thermal cross section

Once the resonances were adjusted individually (see section 5.3), the capture yield was fitted from 26.3 meV to 100 meV, with one bound state at the mirror energy of the first resonance, with the scattering width as a free parameter. The radiative width was taken as the average of the set of observed resonances, at 44.2 meV. The procedure was iterated until the parameters for the first resonance and the

bound state reached convergence, see figure 5.1. Finally the full cross section was calculated using the newly obtained resonance parameters (including the bound state) and the value at 25.3 meV was extracted. The results for the two detectors analyzed separately were giving consistent results.

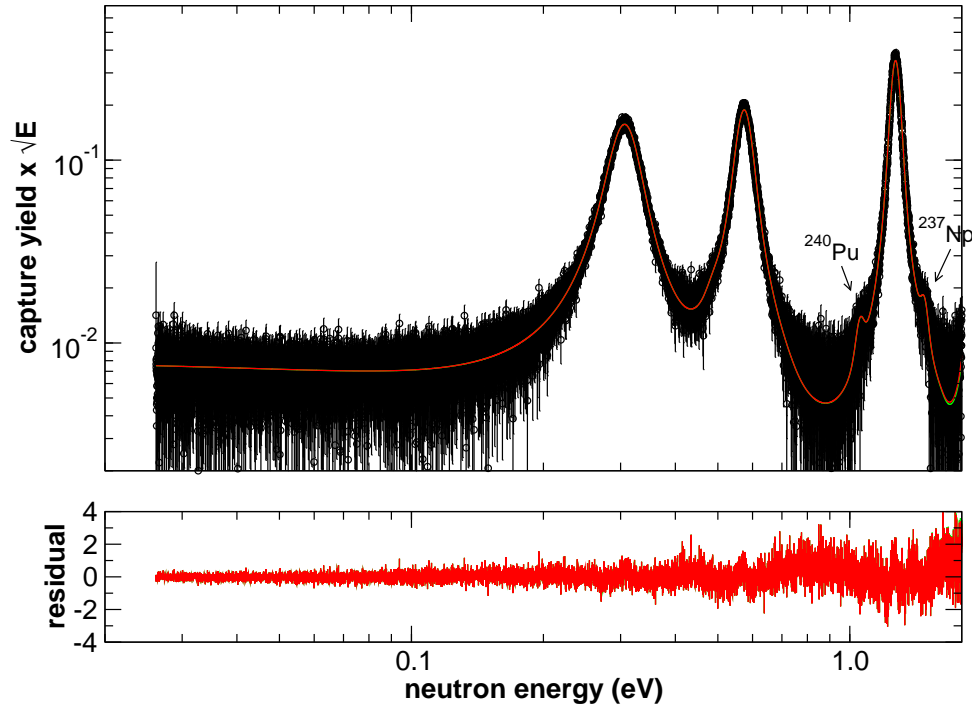


Figure 5.1: The ^{241}Am capture yield with a 300 keV threshold is fitted up to the first resonance by varying the bound state resonance parameters. The y axis is multiplied by \sqrt{E} for convenience, as it allows a better view of the thermal region.

However the main object of concern in this analysis is the extraction of the uncertainty to associate to the central value. There is no ideal way to estimate the uncertainty, given all the analysis steps, nonetheless it is possible to repeat the analysis separately for the two detectors and different energy deposition thresholds, and check if the yield is invariant. The deviations will provide a instructive insight on the uncertainty. Figure 5.2 shows a first comparison of capture yields at 26.3 meV for the two detectors with thresholds between 200 keV and 1 MeV on the first resonance, in order to check if the analysis (especially the weighting function procedure) still holds at large thresholds.

One can notice that the yields are in good agreement (within 2%) for thresholds below 500 keV, whereas for larger thresholds the calculated capture yield tends to be underestimated. This is most certainly a systematic bias of the weighting function procedure, which is not supposed to be used with large thresholds. However, when looking at yields normalized to the first resonance with 300 keV threshold,

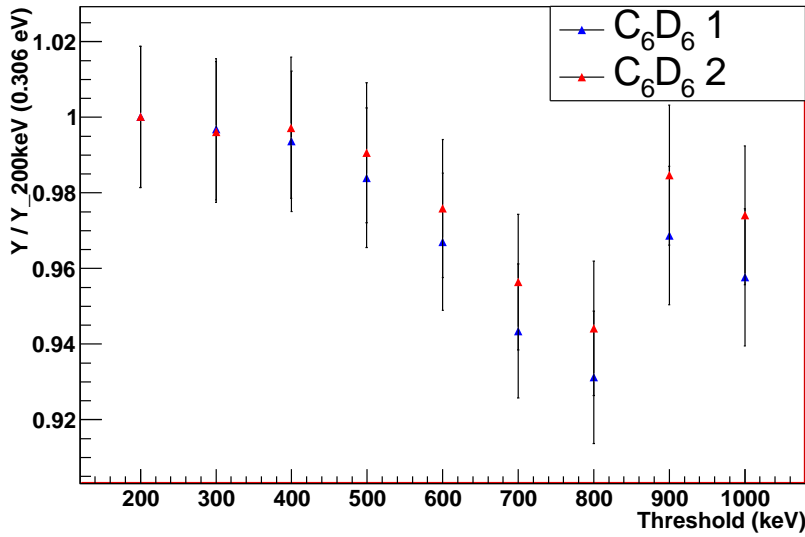
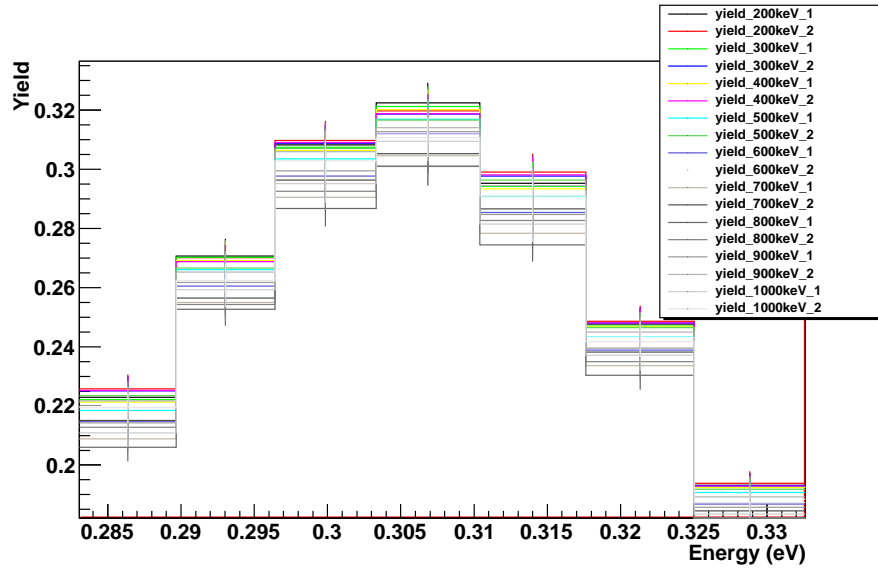


Figure 5.2: Upper panel: the capture yield on the first resonance for thresholds from 200 keV to 1 MeV, each normalized to the ^{197}Au capture yield with the same threshold. Lower panel: ratios to the 200 keV threshold capture yield at $E_n=0.306$ eV.

one is only sensitive to uncertainties in background normalization, which are dominant at thermal neutron energy. Figure 5.3 shows the low energy part of the capture yield for all thresholds, normalized to first resonance of the capture yield with 300 keV threshold, itself normalized to the 4.9 eV ^{197}Au resonance. The values at thermal energy show typical deviations of 10%, which are summed

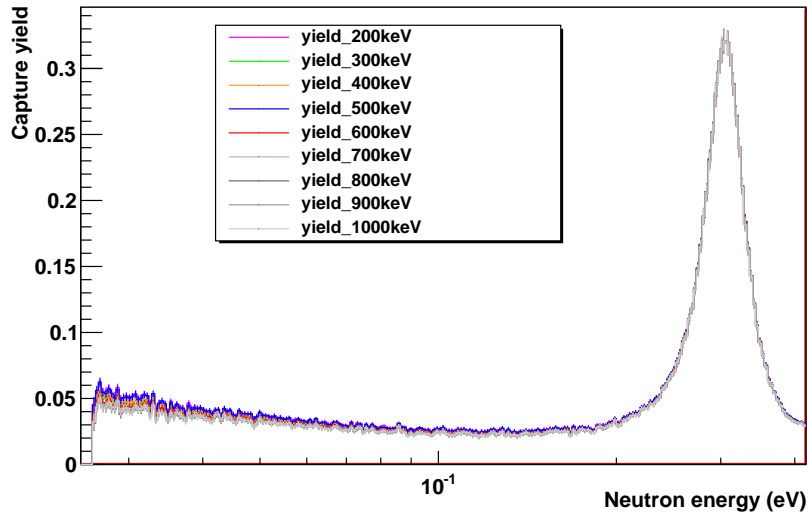


Figure 5.3: The capture yield at low energy for all thresholds from 200 keV to 1 MeV, normalized to the first resonance of the capture yield with 300 keV threshold.

up in figure 5.4, where the uncertainties due to counting statistics in the fit are negligible. The background/signal ratios for thresholds between 200 keV and 1 MeV vary from 0.83 to 0.93, mostly because of the high energy gamma rays (especially the 2235 keV photon produced by (α, p) reaction on the aluminium canning) emitted by the sample. This large background will inevitably lead to a large error propagation when subtracted to the total signal. This mostly explains the large uncertainty at low energy. Indeed, given the deviations of the thermal capture yield values with respect to the chosen threshold (approximately 10%), only a 1% uncertainty in background estimation (including statistics, weighting function and normalization) would be enough to explain a 10% uncertainty on the net signal, with a 90% background/signal ratio.

The main comment on figure 5.4 is that the general behaviour of the observed capture yield is not depending on the normalization technique, which strongly implies that the source of uncertainty does not come from the pulse height weighting and normalization to the ^{197}Au resonance, but more likely from the background subtraction. The definitive choice for the thermal cross section was to take the value given by the fit of the resonances, and associate a 10% error bar, which is representative of the spread of the experimental values when varying the deposited energy threshold. Finally, the thermal cross section extracted in this work is $\sigma = 678 \pm 68$ barns. Although it is in relative good agreement with some previous measurements (see figure 5.5), it is delicate to significantly exclude many other values, because of the large error bar associated with it. Also, the Wescott factor extracted in this analysis is 0.995.

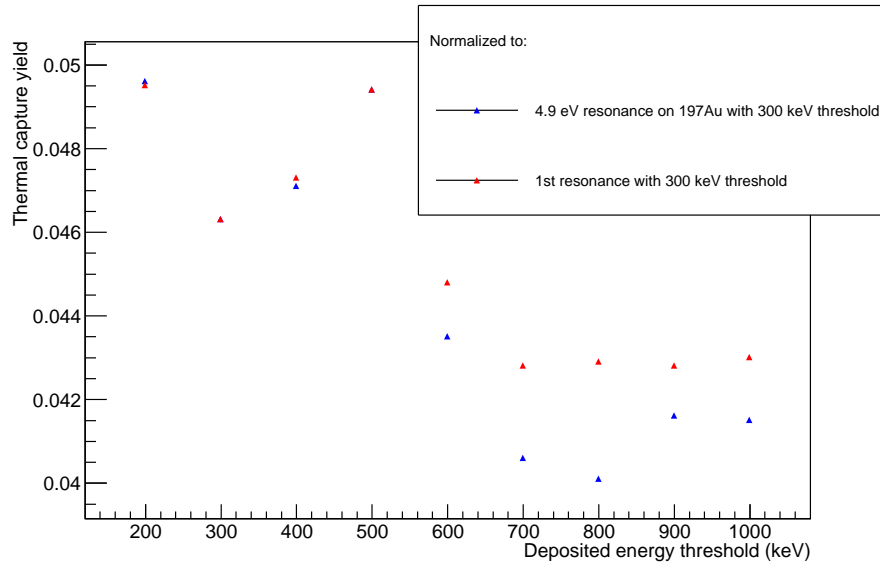


Figure 5.4: The thermal capture yields obtained with different thresholds and normalization technique.

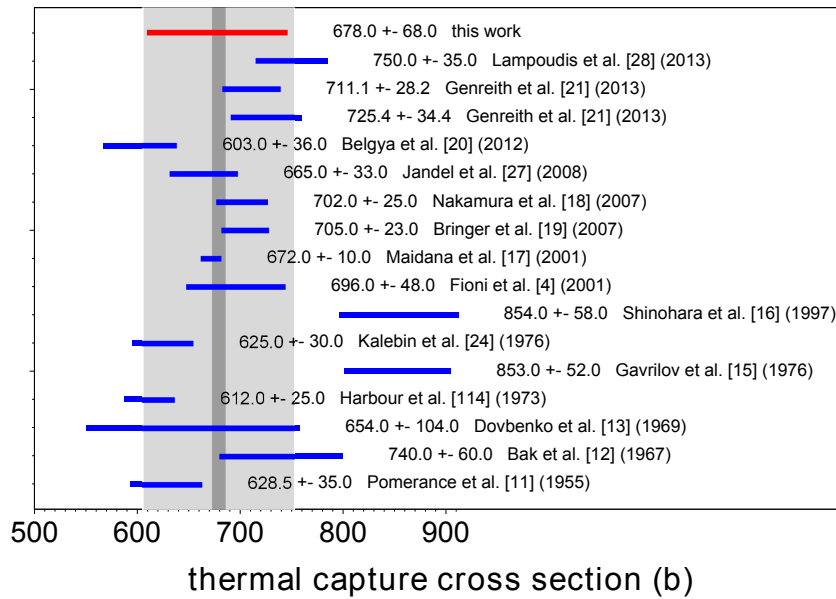


Figure 5.5: Experimental thermal cross section values compared to this work. The larger grey band indicates the average and standard deviation of the central values (691.2 and 78.1 b). The smaller grey band corresponds to the weighted mean and its uncertainty, excluding values without uncertainty (674.8 and 6.6 b).

5.3 The resolved resonance region (RRR)

Resonance shape analysis was conducted using the R-matrix code SAMMY [71]. It included full multiple scattering and self-shielding corrections, and used the free gas model for Doppler broadening. The variant of the R-matrix formalism used was the Reich-Moore approximation, detailed in section 2.3.4. This formalism has the immense advantage (compared to the multi-level Breit-Wigner approximation for example) to fully include interference between levels for non radiative channels. Concerning the fit procedure, resonances were fitted individually whenever possible, and overlapping resonances forming multiplets were fitted together. The gamma partial width Γ_γ was let free for the first three large resonances, where it is expected to be sensitive to small variations of the parameters (see table 5.1).

Table 5.1: The resonance parameters for the first three resonances. Only uncertainties due to counting statistics have been used in the data, and the uncertainties resulting from the fit correspond to the square root of the diagonal terms only. The correlation factor between Γ_n and Γ_γ from the fit was lower 0.25.

Energy (eV)	J (\hbar)	Γ_n μeV	Γ_γ (meV)
-0.306	3	275.3 ± 2.0	45.79
0.306	3	49.1 ± 0.1	45.35 ± 0.3
0.575	2	116.7 ± 0.3	44.41 ± 0.5
1.272	3	290.0 ± 0.9	47.16 ± 0.3

However, as the Γ_γ values are supposed to follow an almost constant distribution (more precisely a χ^2 distribution with a large number of degrees of freedom), it was fixed for the following smaller resonances, and taken as recommended by JEFF-3.1.2 [41]. The fission widths were fixed and also taken as recommended by JEFF-3.1.2 [41]. It was possible to perform the resonance shape analysis up to 320 eV, which is a significant improvement over the current status of the evaluated RRR (which ends at 150 eV in all evaluations). Figure 5.6 shows the full range of fitted resonances.

Table 5.2 gives the full list of resonance parameters obtained in this analysis (with new or heavily modified resonances, compared to JEFF-3.1.2 [41], marked with a *), which are to be used in order to extract statistical informations on the compound ^{242}Am nucleus.

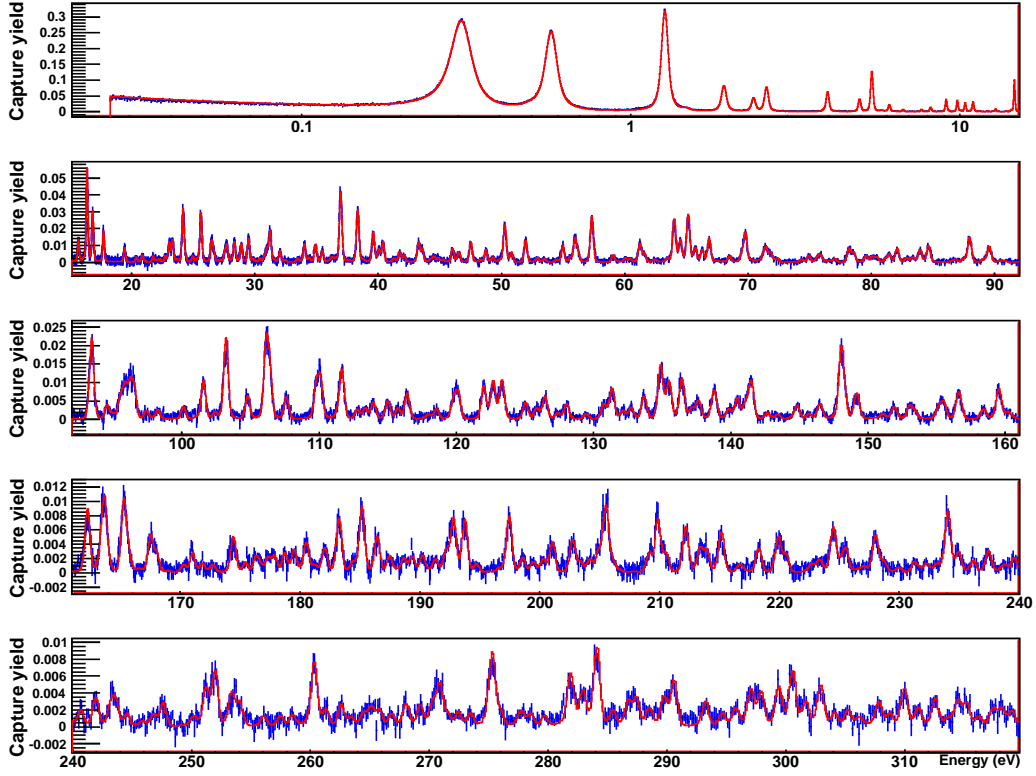


Figure 5.6: The resolved resonance range analyzed in this work.

Table 5.2: The resonance parameters obtained by this work.

Energy (eV)	J (\hbar)	Γ_n (meV)	$d\Gamma_n$ (meV)	Γ_γ (meV)
1.922	3	0.104	0.0006	45.79
2.365	2	0.093	0.0009	45.79
2.589	3	0.137	0.0009	45.79
3.971	2	0.261	0.0023	45.79
4.966	3	0.160	0.0018	45.79
5.412	2	0.936	0.0065	45.79
5.926	2	0.013	0.0021	45.79
6.116	3	0.115	0.0021	45.79
6.736	3	0.038	0.0017	45.79
7.660	2	0.065	0.0029	45.79
8.167	3	0.106	0.0027	45.79
9.107	2	0.489	0.0068	45.79
9.845	3	0.366	0.0056	45.79

Table 5.2: continued.

Energy (eV)	J (\hbar)	Γ_n (meV)	$d\Gamma_n$ (meV)	Γ_γ (meV)
10.07	2	0.055	0.0041	45.79
10.40	3	0.300	0.0049	45.79
10.99	2	0.502	0.0086	45.79
11.49	3	0.033	0.0035	45.79
12.19	3	0.024	0.0034	45.79
12.88	2	0.177	0.0069	45.79
13.90	3	0.036	0.0042	45.79
14.36	2	0.126	0.0081	45.79
14.68	3	2.062	0.0227	45.79
15.68	2	0.340	0.0107	45.79
16.39	3	1.103	0.0162	45.79
16.85	2	0.838	0.0163	45.79
17.72	3	0.388	0.0100	45.79
19.43	2	0.311	0.0120	45.79
20.38	3	0.041	0.0074	45.79
20.88	3	0.115	0.0072	45.79
21.75	2	0.147	0.0116	45.79
22.28	3	0.058	0.0075	45.79
22.73	2	0.164	0.0124	45.79
23.06	3	0.383	0.0135	45.79
23.33	2	0.603	0.0200	45.79
24.18	3	1.092	0.0236	45.79
24.38	3	0.076	0.0119	45.79
25.31	2	0.082	0.0148	45.79
25.63	3	1.124	0.0238	45.79
26.48	2	0.628	0.0279	45.79
26.69	3	0.204	0.0158	45.79
27.18*	3	0.057	0.0093	45.79
27.56	2	0.322	0.0226	45.79
27.74	3	0.411	0.0198	45.79
28.11*	3	0.051	0.0133	45.79
28.35	2	0.750	0.0260	45.79
28.90	3	0.477	0.0175	45.79
29.50	3	0.640	0.0205	45.79
29.90	2	0.107	0.0179	45.79
30.77	3	0.144	0.0159	45.79
30.99	2	0.518	0.0318	45.79
31.24	3	0.933	0.0280	45.79

Table 5.2: continued.

Energy (eV)	J (\hbar)	Γ_n (meV)	$d\Gamma_n$ (meV)	Γ_γ (meV)
31.57*	3	0.058	0.0121	45.79
32.04	2	0.484	0.0253	45.79
32.45*	3	0.069	0.0127	45.79
33.50	3	0.114	0.0164	45.79
34.02	2	0.851	0.0330	45.79
34.43	3	0.163	0.0162	45.79
34.93	2	0.846	0.0338	45.79
35.48	3	0.419	0.0209	45.79
36.01*	2	0.094	0.0244	45.79
36.26	3	0.177	0.0198	45.79
36.53	2	0.204	0.0287	45.79
36.97	3	2.930	0.0621	45.79
37.61*	3	0.087	0.0156	45.79
38.36	2	3.107	0.0785	45.79
38.76	3	0.079	0.0210	45.79
39.61	3	1.222	0.0373	45.79
40.06	2	0.766	0.0419	45.79
40.40	3	0.845	0.0350	45.79
41.27	2	0.166	0.0316	45.79
41.77	3	0.433	0.0256	45.79
42.12	2	0.429	0.0365	45.79
43.28	3	0.961	0.0403	45.79
43.59	2	0.880	0.0447	45.79
44.54	3	0.330	0.0289	45.79
44.90	3	0.211	0.0250	45.79
45.28*	2	0.176	0.0374	45.79
46.04	2	0.955	0.0525	45.79
46.58	3	0.484	0.0320	45.79
47.54	2	1.499	0.0583	45.79
48.31*	2	0.182	0.0321	45.79
48.76	3	0.683	0.0371	45.79
49.32	3	0.271	0.0280	45.79
50.28	2	2.896	0.0965	45.79
50.83	3	0.531	0.0340	45.79
51.98	2	1.923	0.0726	45.79
52.93	3	0.262	0.0286	45.79
53.50	2	0.311	0.0381	45.79
54.49	3	0.162	0.0319	45.79

Table 5.2: continued.

Energy (eV)	J (\hbar)	Γ_n (meV)	$d\Gamma_n$ (meV)	Γ_γ (meV)
55.00	2	1.580	0.0708	45.79
55.59	3	0.309	0.0374	45.79
55.98	2	2.280	0.0992	45.79
56.24	3	0.610	0.0513	45.79
57.35	3	3.421	0.1014	45.79
59.08	2	0.727	0.0669	45.79
60.06	3	0.236	0.0437	45.79
60.46	2	0.362	0.0559	45.79
61.26	3	1.472	0.0636	45.79
61.62	2	0.858	0.0662	45.79
62.44	3	0.180	0.0342	45.79
63.47	3	0.291	0.0355	45.79
64.04	2	5.586	0.1870	45.79
64.55	3	1.830	0.0745	45.79
65.18	2	6.411	0.2038	45.79
65.75	3	1.161	0.0752	45.79
66.31	2	1.534	0.0884	45.79
66.88	3	2.121	0.0836	45.79
68.54	2	0.767	0.0697	45.79
69.52	3	0.819	0.0750	45.79
69.82	2	4.102	0.1725	45.79
70.32*	3	0.163	0.0439	45.79
70.81*	3	0.165	0.0420	45.79
71.26	3	0.621	0.0882	45.79
71.50	2	1.768	0.1296	45.79
71.88	3	0.966	0.0715	45.79
72.38	3	0.372	0.0486	45.79
74.39*	3	0.266	0.0503	45.79
74.97	2	0.955	0.0871	45.79
75.66	3	0.540	0.0696	45.79
75.94	2	0.965	0.0950	45.79
76.61*	2	0.245	0.0778	45.79
77.08	3	0.339	0.0495	45.79
78.23	2	2.138	0.1349	45.79
78.60	3	1.043	0.0774	45.79
79.62	3	0.707	0.0675	45.79
80.12	2	0.906	0.1052	45.79
80.49	3	0.594	0.0705	45.79

Table 5.2: continued.

Energy (eV)	J (\hbar)	Γ_n (meV)	$d\Gamma_n$ (meV)	Γ_γ (meV)
81.22	2	0.524	0.0980	45.79
81.51	3	0.906	0.0855	45.79
82.13	2	2.306	0.1434	45.79
82.90	3	0.531	0.0673	45.79
83.38	2	0.696	0.0951	45.79
84.01	3	1.521	0.0958	45.79
84.67	3	2.100	0.1028	45.79
86.87	2	0.526	0.0853	45.79
87.50	3	0.376	0.0597	45.79
88.01	2	4.959	0.2237	45.79
89.19	3	0.364	0.0647	45.79
89.62	2	3.021	0.1752	45.79
90.46*	3	0.199	0.0493	45.79
93.46	3	5.937	0.2347	45.79
94.58*	3	0.907	0.0939	45.79
95.00	2	0.499	0.1197	45.79
95.54	3	1.502	0.1331	45.79
95.89	2	3.295	0.2487	45.79
96.25	3	2.494	0.1973	45.79
96.56	2	3.127	0.2367	45.79
97.44	3	0.569	0.0811	45.79
98.27	3	0.644	0.0740	45.79
100.14	2	1.130	0.1387	45.79
101.61	3	3.060	0.1650	45.79
102.46	2	0.748	0.1138	45.79
103.24	3	6.768	0.2793	45.79
104.82	3	1.900	0.1491	45.79
106.18	2	9.651	0.5181	45.79
106.47	3	3.212	0.2473	45.79
107.65	2	2.685	0.2311	45.79
109.83	3	2.779	0.2280	45.79
110.15	2	5.273	0.3873	45.79
111.41	3	0.615	0.2003	45.79
111.69	2	6.237	0.3828	45.79
112.82	3	0.831	0.0999	45.79
113.39	2	1.281	0.1564	45.79
114.00	3	1.509	0.1440	45.79
115.05	3	1.654	0.1465	45.79

Table 5.2: continued.

Energy (eV)	J (\hbar)	Γ_n (meV)	$d\Gamma_n$ (meV)	Γ_γ (meV)
115.78	2	1.386	0.1819	45.79
116.45	3	2.550	0.1863	45.79
118.00	2	0.638	0.1542	45.79
118.59	3	1.075	0.1303	45.79
119.83	2	2.758	0.2663	45.79
120.17	3	2.531	0.1859	45.79
122.05	2	5.010	0.3378	45.79
122.73	3	4.008	0.2323	45.79
123.37	3	3.998	0.2224	45.79
125.08	2	2.453	0.2307	45.79
125.89	3	1.095	0.1666	45.79
126.51	2	3.387	0.2499	45.79
127.43	3	0.619	0.1127	45.79
128.08	2	2.560	0.2566	45.79
129.50	3	0.557	0.1171	45.79
130.80	2	2.391	0.2609	45.79
131.39	3	3.571	0.2432	45.79
132.19	3	0.916	0.1594	45.79
132.78	2	1.927	0.2406	45.79
133.73	3	2.549	0.2038	45.79
134.93	2	9.964	0.6006	45.79
135.53	3	4.727	0.3044	45.79
136.48	2	7.565	0.5290	45.79
137.19	3	1.220	0.1645	45.79
137.69	2	2.987	0.3176	45.79
138.83	3	3.558	0.2271	45.79
139.90	3	1.157	0.1603	45.79
140.52	2	3.633	0.3345	45.79
141.10	3	1.684	0.2082	45.79
141.54	2	7.583	0.5065	45.79
142.72*	2	1.082	0.1774	45.79
143.47	3	0.605	0.1562	45.79
144.87	2	2.495	0.2124	45.79
145.74	3	0.701	0.1417	45.79
146.55	2	2.983	0.2608	45.79
148.14	3	13.182	0.6560	45.79
149.23	3	3.745	0.2965	45.79
151.13*	2	0.996	0.2096	45.79

Table 5.2: continued.

Energy (eV)	J (\hbar)	Γ_n (meV)	$d\Gamma_n$ (meV)	Γ_γ (meV)
151.95*	2	2.563	0.3350	45.79
153.07*	2	2.599	0.3114	45.79
153.47*	2	1.554	0.2649	45.79
155.17*	2	2.082	0.3212	45.79
155.55*	3	2.437	0.2774	45.79
156.67*	2	5.873	0.4280	45.79
158.48*	3	1.448	0.2237	45.79
159.59*	2	7.206	0.5099	45.79
160.26*	2	1.635	0.2591	45.79
162.32*	3	5.181	0.3400	45.79
163.45*	3	1.459	0.3866	45.79
163.72*	2	8.308	1.0450	45.79
164.02*	3	0.845	0.2589	45.79
165.34*	3	6.231	0.4455	45.79
165.74*	3	1.707	0.2787	45.79
166.49*	3	0.220	0.1353	45.79
167.59*	2	4.605	0.4230	45.79
168.10*	2	2.239	0.3018	45.79
170.36*	3	0.573	0.1356	45.79
171.09*	3	1.726	0.2115	45.79
171.90*	3	0.792	0.1756	45.79
172.74*	3	0.675	0.1677	45.79
174.49*	2	4.695	0.4850	45.79
176.35*	3	1.031	0.2505	45.79
176.65*	3	0.612	0.2625	45.79
175.51*	3	0.786	0.1399	45.79
177.39*	2	1.800	0.2956	45.79
177.93*	2	2.226	0.3192	45.79
178.79*	3	1.866	0.2530	45.79
179.56*	3	2.119	0.2264	45.79
180.58*	2	4.142	0.4473	45.79
181.30*	2	0.870	0.2639	45.79
182.12*	3	2.317	0.2522	45.79
183.32*	2	8.323	0.6909	45.79
184.50*	2	1.237	0.3878	45.79
185.24*	3	7.385	0.5195	45.79
186.50*	2	5.501	0.5373	45.79
187.53*	3	1.582	0.2235	45.79

Table 5.2: continued.

Energy (eV)	J (\hbar)	Γ_n (meV)	$d\Gamma_n$ (meV)	Γ_γ (meV)
188.72*	2	1.904	0.3038	45.79
189.43*	3	1.573	0.2316	45.79
190.28*	2	2.492	0.3388	45.79
191.36*	2	1.849	0.2951	45.79
192.26*	3	2.218	0.2973	45.79
192.87*	3	5.970	0.4547	45.79
193.83*	2	9.098	0.7718	45.79
194.81*	2	1.143	0.2829	45.79
197.53*	3	6.748	0.5124	45.79
198.65*	2	2.190	0.4003	45.79
199.53*	2	1.600	0.2940	45.79
200.34*	3	1.278	0.2293	45.79
201.14*	3	3.635	0.4210	45.79
202.83*	2	5.608	0.6521	45.79
203.47*	3	1.197	0.2575	45.79
204.25*	2	1.845	0.3298	45.79
205.60*	3	9.263	0.7976	45.79
206.16*	2	1.799	0.3666	45.79
204.98*	3	2.175	0.3124	45.79
209.21*	2	2.890	0.4201	45.79
209.95*	3	7.140	0.5959	45.79
210.65*	3	2.252	0.3551	45.79
212.28*	2	8.766	0.8107	45.79
213.45*	3	2.897	0.4141	45.79
214.01*	3	2.874	0.4741	45.79
215.25*	2	7.755	0.8018	45.79
216.77*	2	1.096	0.2811	45.79
218.37*	2	4.412	0.5029	45.79
220.01*	3	4.522	0.4738	45.79
220.66*	3	2.301	0.3648	45.79
222.78*	2	1.488	0.4857	45.79
223.44*	2	2.280	0.4211	45.79
224.60*	2	9.291	0.8809	45.79
225.34*	3	1.637	0.4234	45.79
225.69*	3	2.590	0.5829	45.79
227.12*	3	0.744	0.2572	45.79
228.12*	3	5.163	0.5483	45.79
228.78*	3	1.374	0.4362	45.79

Table 5.2: continued.

Energy (eV)	J (\hbar)	Γ_n (meV)	$d\Gamma_n$ (meV)	Γ_γ (meV)
230.02*	3	0.577	0.2183	45.79
231.37*	2	1.920	0.3995	45.79
232.38*	2	1.681	0.3811	45.79
233.23*	2	1.445	0.4243	45.79
234.15*	3	10.118	0.8067	45.79
235.04*	3	2.842	0.3963	45.79
236.30*	2	2.424	0.5535	45.79
237.55*	3	3.034	0.3976	45.79
238.86*	2	1.507	0.4516	45.79
239.71*	2	2.969	0.7166	45.79
240.78*	3	2.034	0.3974	45.79
242.04*	2	5.493	0.7165	45.79
243.31*	3	2.918	0.5186	45.79
243.74*	3	2.921	0.4986	45.79
244.67*	3	1.644	0.3238	45.79
245.96*	3	0.615	0.2706	45.79
246.91*	2	2.084	0.4927	45.79
247.71*	2	4.697	0.8776	45.79
250.29*	2	1.726	0.4788	45.79
251.32*	2	7.648	0.9632	45.79
252.09*	2	12.437	1.3395	45.79
253.49*	3	4.941	0.6782	45.79
254.16*	3	3.570	0.4948	45.79
256.17*	2	1.910	0.5007	45.79
257.60*	3	1.299	0.3683	45.79
258.58*	3	1.539	0.3679	45.79
260.43*	2	16.512	1.6024	45.79
261.41*	3	2.379	0.5622	45.79
262.70*	2	4.614	0.8427	45.79
263.50*	2	1.783	0.4954	45.79
264.58*	3	1.734	0.4663	45.79
265.22*	2	3.743	0.7979	45.79
265.89*	3	2.575	0.5871	45.79
266.95*	2	2.511	0.5237	45.79
268.09*	2	3.548	1.1039	45.79
268.30*	2	1.442	0.9280	45.79
269.36*	3	3.215	0.5739	45.79
270.37*	2	4.679	0.8257	45.79

Table 5.2: continued.

Energy (eV)	J (\hbar)	Γ_n (meV)	$d\Gamma_n$ (meV)	Γ_γ (meV)
271.00*	2	9.220	1.3141	45.79
271.64*	3	1.750	0.3966	45.79
272.56*	3	1.984	0.3479	45.79
273.59*	3	1.937	0.4719	45.79
275.40*	2	21.816	2.1859	45.79
276.13*	2	3.561	0.7957	45.79
277.85*	3	2.170	0.4014	45.79
278.65*	2	2.802	0.6934	45.79
279.82*	2	2.259	0.3937	45.79
282.00*	2	14.729	1.5980	45.79
283.02*	2	8.999	1.0827	45.79
284.21*	3	16.835	1.4848	45.79
285.56*	3	2.566	0.7619	45.79
286.84*	2	5.812	1.0612	45.79
287.54*	2	7.151	1.1283	45.79
288.62*	2	4.280	0.7197	45.79
289.86*	3	5.000	0.7094	45.79
290.72*	2	12.629	1.3890	45.79
293.36*	3	4.179	0.6068	45.79
294.78*	3	2.121	0.4481	45.79
295.90*	2	4.484	0.7907	45.79
297.17*	3	6.458	0.7973	45.79
298.04*	3	6.345	0.8079	45.79
299.53*	2	10.940	1.4760	45.79
300.70*	3	11.421	1.2003	45.79
301.79*	2	6.801	1.0814	45.79
303.06*	3	8.061	0.8034	45.79
304.23*	2	3.407	0.8024	45.79
305.36*	3	2.963	0.5665	45.79
306.28*	3	1.445	0.5014	45.79
307.94*	2	6.683	1.1291	45.79
308.84*	2	3.180	0.8035	45.79
310.09*	3	7.744	0.9637	45.79
311.25*	2	4.815	0.9718	45.79
312.70*	3	5.242	0.7387	45.79
313.80*	2	1.728	0.7502	45.79
314.62*	2	7.162	1.2923	45.79
315.34*	3	4.601	0.7624	45.79

Table 5.2: continued.

Energy (eV)	J (\hbar)	Γ_n (meV)	$d\Gamma_n$ (meV)	Γ_γ (meV)
316.33*	2	2.389	0.7682	45.79
317.57*	3	3.396	0.7195	45.79
318.28*	2	4.916	1.3758	45.79
319.13*	3	3.080	0.6021	45.79

The resonance integral above 0.5 eV was calculated thanks to the following formula:

$$I = \int_{E_c}^{\infty} \sigma_{n,\gamma}(E) \times \frac{dE}{E} \quad (5.1)$$

where $E_c=0.5$ eV. It should be noted that the traditional choice of 0.5 eV for the lower bound of the integral is, in the case of ^{241}Am , a source of uncertainty, since the first resonance is at 0.3 eV and the second one at 0.57 eV. This means that a very slight change in the resonance parameters will have a very significant effect on the resonance integral, if the lower bound is chosen at 0.5 eV. The resonance integral after 0.5 eV was found to be 1425.0 barns. For further comparison, Nakamura *et al.*[32] calculated the resonance integral above 107 meV, and found 3.5 kbarns. With the same lower bound, the resonance integral calculated by this work is 2870.5 barns. The decreased resonance integral values obtained by this work compared to previous evaluations is certainly mostly explained by the first three large resonances, which have been assigned smaller scattering widths than in most recent works.

5.4 Statistical analysis

Once the resonances have been assigned, it is possible to perform a statistical analysis of this new set of states. First, one can check if the resonances are all s -waves, *i.e.* carrying $l = 0$ angular momentum in the entrance channel. This test is carried out by a statistical approach, based on Bayesian probabilities, inspired by the work of Bollinger and Thomas [80]. The quantity of interest is the probability of a resonance being a p -wave, given the observed scattering width $g\Gamma_n$. It can be expressed using Bayes theorem, and the assumption that only s - and p - waves

are present in the observed set of states.

$$P(l = 1|g\Gamma_n) = \frac{P(g\Gamma_n|l = 1)P(l = 1)}{P(g\Gamma_n)} \quad (5.2)$$

$$= \frac{P(g\Gamma_n|l = 1)P(l = 1)}{P(g\Gamma_n|l = 0)P(l = 0) + P(g\Gamma_n|l = 1)P(l = 1)} \quad (5.3)$$

$$= \frac{1}{1 + \frac{P(l=0)P(g\Gamma_n|l=0)}{P(l=1)P(g\Gamma_n|l=1)}} \quad (5.4)$$

The first fraction in the denominator $\frac{P(l=0)}{P(l=1)}$ can be estimated by assuming a $(2J+1)$ dependence on the level density. With a target spin $I = 5/2^-$, the possible spin states for s -waves are 2^- and 3^- , whereas for p -waves they are 1^+ , 2^+ , 3^+ , 4^+ . Hence:

$$\frac{P(l = 0)}{P(l = 1)} = \frac{\sum_{J=2}^3 (2J + 1)}{\sum_{J=1}^4 (2J + 1)} = \frac{1}{2} \quad (5.5)$$

The second fraction in the denominator of equation 5.4 can be expressed using the assumption of a Porter-Thomas (PT) distribution for the reduced neutron widths. The detailed mathematical treatment has been discussed by Gyulassy et al. [81], and is based on a weighted combination of PT distributions with one a two degrees of freedom, respectively for $l = 0$ and $l = 1$ states. For a target spin $I = 5/2^-$, the ratio of interest is finally given by:

$$\frac{P(g\Gamma_n|l = 0)}{P(g\Gamma_n|l = 1)} = \quad (5.6)$$

$$\frac{\sqrt{\frac{2v_1 S_1 D_1}{S_0 D_0}} \exp \left[-\frac{g\Gamma_n}{2\sqrt{E}} \left(\frac{1}{S_0 D_0} - \frac{1}{2v_1 S_1 D_1} \right) \right]}{\frac{1}{2} + \frac{1}{2} \sqrt{\frac{\pi g\Gamma_n}{4v_1 S_1 D_1 \sqrt{E}}}} \quad (5.7)$$

where:

$$v_0 = 1, \quad v_1 = \frac{(kR)^2}{1 + (kR)^2} \quad (5.8)$$

$$S_l = \frac{\langle g\Gamma_n^l \rangle}{(2l + 1)D_l} \quad (5.9)$$

$$\Gamma_n^l = \frac{1}{v_l} \sqrt{\frac{1 \text{ eV}}{E}} \Gamma_n \quad (5.10)$$

with $k = 1/\bar{\lambda}$ being the reaction wave number, R being the channel radius, taken as the scattering radius, and D_l the average level spacing for states carrying l units of angular momentum in the entrance channel. At this stage, one has to take average spacings and strength functions from evaluations. Assuming $S_1 = 2.0 \times 10^{-4}$ (from [82]), this analysis yields no p -wave resonance in the observed set of ^{241}Am

resonances, *i.e.* all resonances have $P(l = 1|g\Gamma_n) = 0$.

The next step is to extract the average spacing D_0 and strength function S_0 . To that end, the Porter Thomas distribution is used once again, when expressing the number of $l = 0$ states $N(x_t)$ with $x = \frac{g\Gamma_n^0}{\langle g\Gamma_n^0 \rangle}$ greater than a certain threshold x_t .

$$N(x_t) = N_0 \int_{x_t}^{\infty} \sqrt{\frac{2}{\pi x}} \frac{1}{2} e^{-x/2} dx \quad (5.11)$$

$$= N_0 \left(1 - \operatorname{erf} \left(\sqrt{x_t/2} \right) \right) \quad (5.12)$$

with N_0 the total number of s -waves in the set. Assuming all the resonances are observed after a certain threshold x_t , one can fit this function to the experimental distribution in order to get N_0 and $\langle g\Gamma_n^0 \rangle$ (figure 5.7). The threshold for the fit was chosen to be $g\Gamma_n = 0.07$ meV.

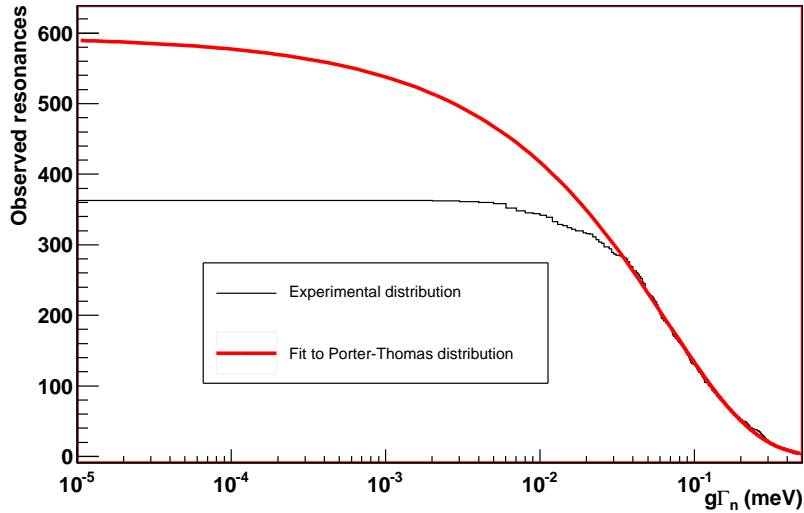


Figure 5.7: The observed distribution is fitted after a threshold of $g\Gamma_n=0.07$ meV.

Then one can extract D_0 and S_0 in a straightforward manner:

$$D_0 = \frac{N_0}{\Delta E} \quad \text{with } \Delta E=320 \text{ eV} \quad (5.13)$$

$$S_0 = \frac{\langle g\Gamma_n^0 \rangle}{D_0} \quad (5.14)$$

This procedure yields $D_0=0.53\pm 0.03$ eV and $S_0 = (1.20 \pm 0.03) \times 10^{-4}$, with a correlation coefficient of -0.90. Concerning the uncertainties, the fit performed in figure 5.7 was repeated using many different values for the $g\Gamma_n$ threshold. Indeed

one can expect to find a range of values for this parameter in which the result of the fit should be invariant. Figure 5.8 shows the results for D_0 and S_0 for all the possible values of the $g\Gamma_n$ threshold, where one can also notice the strong anti-correlation given by the fit.

The typical standard deviations observed in figure 5.8 were chosen as error bars on the result obtained with $g\Gamma_n=0.07$ meV.

5.5 The unresolved resonance region (URR)

After 320 eV neutron energy, the resolution was not good enough to perform any satisfactory fit of individual resonances. Therefore it marks the start of the unresolved resonance range. The upper limit for this analysis was chosen at 150 keV, and is a consequence of the recovery time of the C_6D_6 after the gamma flash, as shown on figure 5.9.

At short times of flight, the two detectors give a different capture yield (typically starting at 200 keV neutron energy), and cannot be trusted. At 150 keV, the fission cross section is 70 times lower than the capture cross section in all evaluations (around 18 mb against 1.25 b). Also, inelastic scattering is not an issue, because of the 300 keV effective threshold used for event selection. In order to get the unresolved capture yield, one must average the full resolution data to lose most of the resonance structure, but still keep the sensitivity to the global energy dependence. The binning chosen was 40 bins per decade. Finally, going from the average capture yield to the average cross section is not straightforward, since one has to include self-shielding and multiple scattering. The averaged version of equation 3.10 is assumed to be:

$$\langle Y(E_n) \rangle = f(E_n) \times n \times \langle \sigma_{n,\gamma}(E_n) \rangle \quad (5.15)$$

where $f(E_n)$ is a correction factor which accounts for both self-shielding and multiple scattering corrections. This function cannot in general be determined analytically, but a Monte-Carlo approach can be used. To that end, the SESH code [83] was used to generate artificial resonances, bases on the information on level densities and strength functions, and extract a numerical result for $f(E_n)$ (figure 5.10).

Figure 5.11 shows the comparison of the average cross section obtained by this work (together with the parameterization performed by the FITACS module included in SAMMY) and current evaluations, together with the data of Jandel [36]. The result of the calculation by FITACS is shown in table 5.3, using fixed valued of $D_0 = 0.53$ eV (see section 5.4) and $D_1 = D_0/2$.

It is difficult to explain the discrepancy between the results of the statistical analysis of section 5.4 and the fit performed by FITACS of the average cross section. However, many delicate steps can be underlined. First, the way FITACS calculates

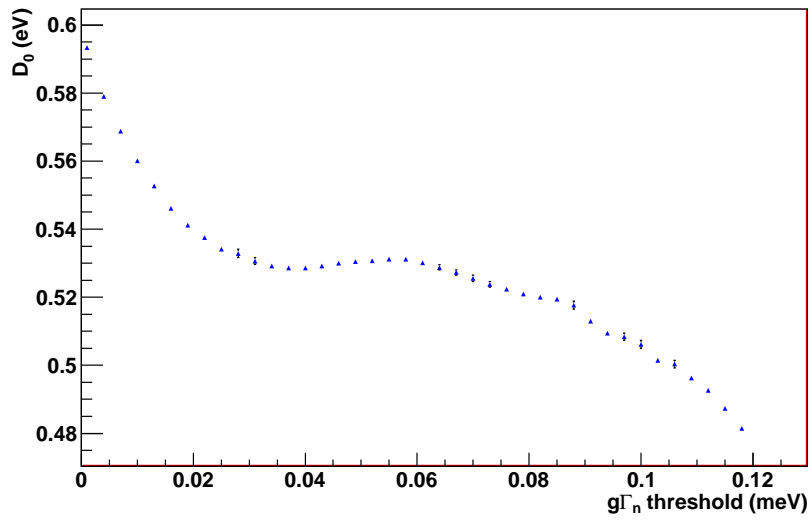
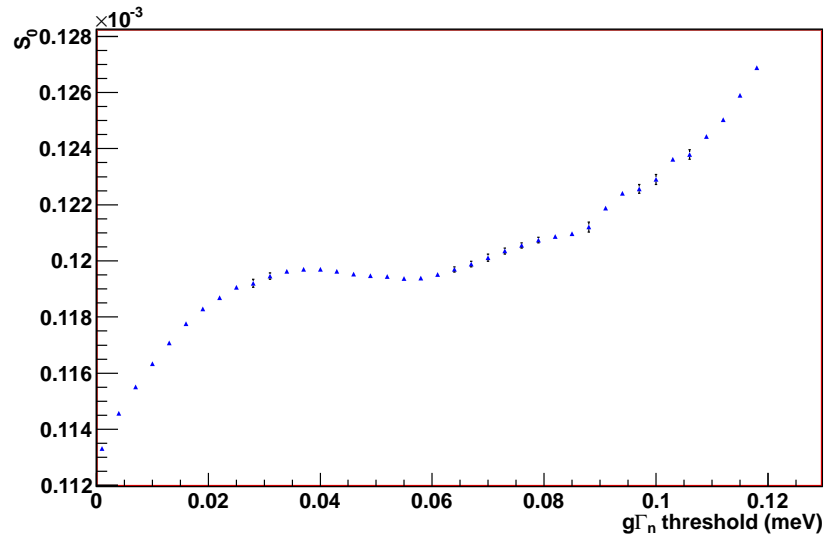


Figure 5.8: The result of the analysis for D_0 and S_0 for different $g\Gamma_n$ threshold values.

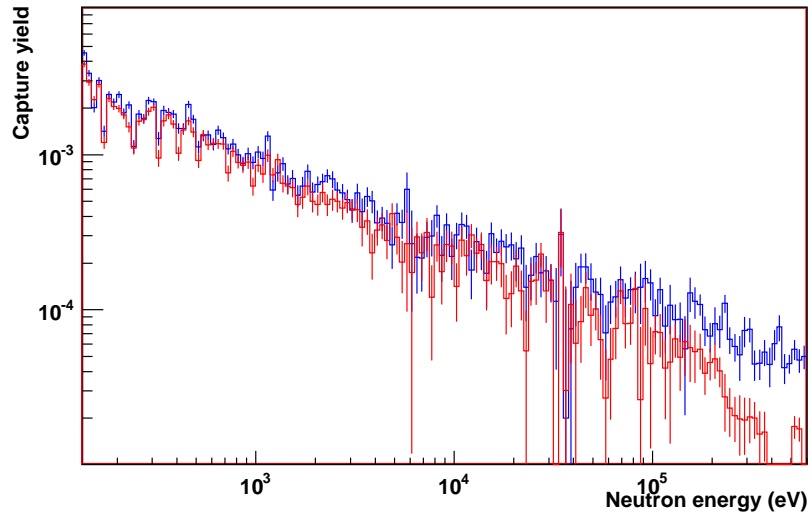


Figure 5.9: The average capture yield for each detector.

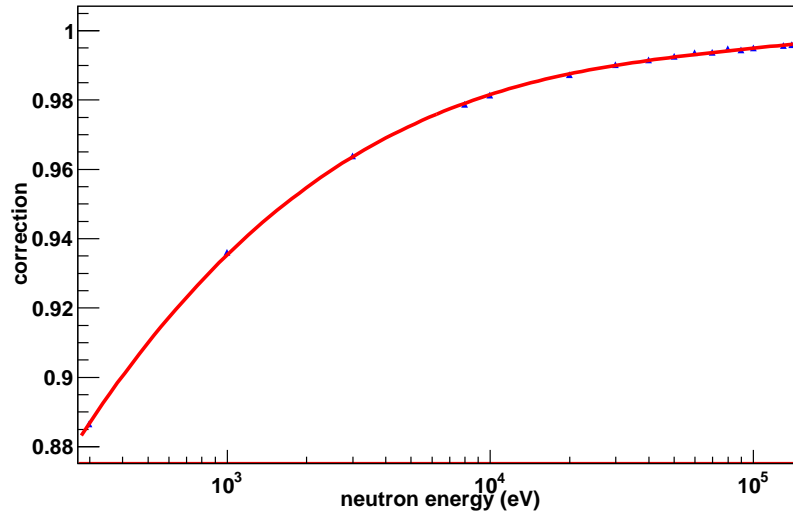


Figure 5.10: The numerical result for $f(E_n)$ and interpolation.

Table 5.3: The result of the average cross section fit by FITACS.

$l = 0$	$l = 1$
$S_0 = (1.44 \pm 0.02) \times 10^{-4}$	$S_1 = (1.14 \pm 0.10) \times 10^{-4}$
$\langle \Gamma_\gamma \rangle = 0.043 \pm 0.002 \text{ meV}$	$\langle \Gamma_\gamma \rangle = 0.045 \pm 0.002 \text{ meV}$

average radiative capture cross section is not completely rigorous, since it does not use the formal triple integral solution coming from the Gaussian Orthogonal Ensemble average, but an approximation inspired by the work of Moldauer [55] for taking into account widths fluctuations. Second, and possibly more importantly, the neutron strength function could show some moderate energy dependence. Finally, FITACS also calculates other parameters (such as the distant level parameter of the R-matrix theory) which are highly correlated to the result for the strength functions.

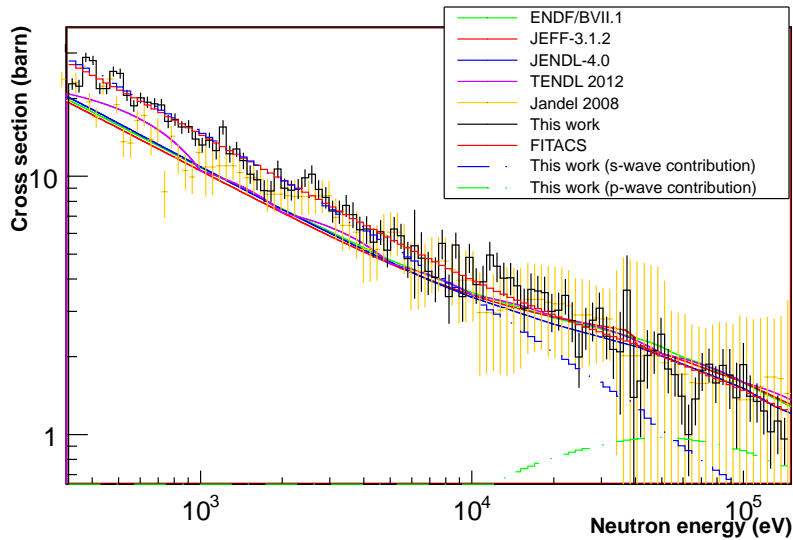


Figure 5.11: The final unresolved cross section is compared to previous data and evaluations.

It is clear that previous estimations and data underestimate the cross section below approximately 10 keV, whereas the agreement is satisfactory at higher energies. This does not seem to originate from an issue in normalization, since the capture yield of ^{197}Au showed consistency with energy, and the first resonances are not systematically larger than previous estimations. Concerning background, the filters did not show any time independent residual contribution, and the scattering on the Al_2O_3 matrix should be taken into account properly in the URR (although it was unusable in the RRR because of Sm resonances). Finally, this increase is consistent with the increase of strength function observed in the RRR. There could be some remaining uncertainty in the energy dependent beam interception factor, or statistical correction calculated by SESH (especially the input strength functions) but it would have to be both localized below 10 keV and quite significant to account for the discrepancy observed in figure 5.11.

Chapter 6

Summary and concluding remarks

The $^{241}\text{Am}(n,\gamma)$ cross section has been successfully measured at the n_TOF facility at CERN. The measurement used time of flight spectrometry and was performed with two optimized C_6D_6 detectors for gamma detection, together with the use of the pulse height weighting technique for efficiency normalization. Because of the very intense radioactivity of the sample, 2 mm lead plates had to be placed in front of the detectors in order to shield them from a very high count rate inducing failures of the current supply to the acquisition. The capture yield on a 32.2 mg ^{241}Am sample was measured from 26.3 meV to 150 keV neutron energy, since it was noticed that the recovery to the gamma flash was longer than previously expected. The thermal cross section was extracted by adjusting the bound state resonance parameters on the data below 100 meV, and was found to be 678 ± 68 barns. It is consistent with several previous measurements, but carries a large error bar, which is a consequence of uncertainty propagation with a large background/signal ratio. The resolved resonance region was analyzed up to 320 eV neutron energy, which is a significant improvement over the current status of evaluations, which stop the resonance analysis at 150 eV. Even below 150 eV, resonances had to be added or heavily modified to fit the present experimental data. A statistical analysis was performed on the newly obtained set of resonant states, which yielded an s -wave strength function $S_0=(1.20\pm 0.03) \times 10^{-4}$, which is larger than expected by previous evaluations, despite an average s -wave level spacing $D_0=0.53\pm 0.03$ eV in good agreement with other works. This increase in strength function is not systematically seen on the full energy range, for instance the first three largest resonances don't show a systematic increase in this work. This effect is better observed at larger neutron energy (where data is scarce), where the resonance widths obtained by this work tend to be larger than previously expected. It is consistently propagated to the unresolved resonance region, where the average cross section between 320 eV and 20 keV seems to have been underestimated by previous works and evaluations. After 20 keV, however, the cross section obtained by this work is consistent with existing data.

The main strengths of this measurement are its good energy resolution, due to the very long flight path used at n_TOF, and good statistics over the whole energy range, due to the large fluence provided by the CERN's spallation target. However, it was perturbed by the great radioactivity of the sample, which not only required the use of lead shielding, but also was the source of a large background/signal ratio for large bins in time (*i.e.* at low neutron energy), and inevitably led to big uncertainties, especially when estimating the thermal cross section. Also, the large neutron fluence provided by the spallation comes with the gamma flash, which prevented the continuation of the analysis past 150 keV. It should be noted that the resonance parameters provided in this thesis do not form an evaluation, and other sets of data, especially transmission and fission, should be included for a full resonance analysis.

Future work should focus on reducing the uncertainty on the thermal cross section, and using a time of flight technique will require to minimize the background as much as possible, as demonstrated in this work. This could be done by using a thinner sample or a larger neutron fluence, but a simpler option could be to use a 4π detector array, and select events only when they reach the total cascade energy. However, larger detector arrays are more sensitive to other kinds of background, such as neutron sensitivity. Also, transmission and fission data would be necessary to complete the resonance analysis performed by this work, up to 320 eV neutron energy. Finally, extending the analysis of the average cross section past 150 keV would be desirable, which could be achieved by reducing the detector response to the gamma flash.

Bibliography

- [1] E. Rutherford. The scattering of alpha and beta particles by matter and the structure of the atom. *Philosophical magazine*, 21:669–688, 1911.
- [2] J. Chadwick. The existence of a neutron. *Proc. Royal Soc. London A*, 136:692–708, 1932.
- [3] N. Bohr. Neutron capture and nuclear constitution. *Nature*, 137:344–348, 1936.
- [4] L. Meitner and O. Frisch. Disintegration of uranium by neutrons: a new type of nuclear reaction. *Nature*, 143:239–240, 1939.
- [5] O. Hahn and F. Strassmann. Über den nachweis und das verhalten der bei der bestrahlung des urans mittels neutronen entstehenden erdalkalimetalle. *NATURWISSENSCHAFTEN*, 27(1):11–15, 1939.
- [6] <http://research.archives.gov/description/593374>.
- [7] <http://www.ne.anl.gov/About/reactors/early-reactors.shtml>.
- [8] Ferenc Morton Szasz. *The day the sun rose twice: The Story of the Trinity Site Nuclear Explosion July 16, 1945*. University of New Mexico Press, 1984.
- [9] International Atomic Energy Agency. *From Obninsk beyond: nuclear power conference looks to the future*, 2006.
- [10] Helge Kragh. *Quantum Generations: A History of Physics in the Twentieth Century*. Princeton NJ: Princeton University Press, 1999.
- [11] Herbert P. Kitschelt. Political opportunity and political protest: Anti-nuclear movements in four democracies. *British Journal of Political Science*, 16(1):57, 1986.
- [12] http://2012books.lardbucket.org/books/general-chemistry-principles-patterns-and-applications-v1.0m/section_24/.
- [13] <http://holbert.faculty.asu.edu/eee460/>.

- [14] Stephanie Sala. PhD thesis, University of Provence, France, 1995.
- [15] CEA-DEN. L'énergie nucléaire du futur. quelles recherches pour quels objectifs? Technical Report ISBN 2-281-11307-8, 2005.
- [16] G. Fioni, M. Cribier, F. Marie, M. Aubert, S. Ayrault, T. Bolognese, J.M. Cavedon, F. Chartier, O. Deruelle, F. Doneddu, H. Faust, A. Gaudry, F. Gunsing, P. Leconte, F. Lelievre, J. Martino, R. Oliver, A. Pluquet, S. Rottger, M. Spiro, and C. Veyssiere. Incineration of Am-241 induced by thermal neutrons. *Nucl. Phys. A*, 693:546–564, 2001.
- [17] V. Berthou et al. *Journal of nuclear materials*, 320:156–162, 2003.
- [18] M. B. Chadwick, M. Herman, P. Oblozinsky, M. E. Dunn, Y. Danon, A. C. Kahler, D. L. Smith, B. Pritychenko, G. Arbanas, R. Arcilla, R. Brewer, D. A. Brown, R. Capote, A. D. Carlson, Y. S. Cho, H. Derrien, K. Guber, G. M. Hale, S. Hoblit, S. Holloway, T. D. Johnson, T. Kawano, B. C. Kiedrowski, H. Kim, S. Kunieda, N. M. Larson, L. Leal, J. P. Lestone, R. C. Little, E. A. McCutchan, R. E. MacFarlane, M. MacInnes, C. M. Mattoon, R. D. McKnight, S. F. Mughabghab, G. P. A. Nobre, G. Palmiotti, A. Palumbo, M. T. Pigni, V. G. Pronyaev, R. O. Sayer, A. A. Sonzogni, N. C. Summers, P. Talou, I. J. Thompson, A. Trkov, R. L. Vogt, S. C. van der Marck, A. Wallner, M. C. White, D. Wiarda, and P. C. Young. ENDF/B-VII.1 Nuclear Data for Science and Technology: Cross Sections, Covariances, Fission Product Yields and Decay Data. *Nuclear Data Sheets*, 112(12, SI):2887–2996, 2011.
- [19] E.M. Gonzalez. Accurate nuclear data for sustainable nuclear energy from the andes project. In *Nuclear Data 2013 conference proceedings*, 2013.
- [20] T. Yamamoto. Analysis of core physics experiments of high moderation full mox lwr. In *Proc. of the 2005 Symposium on Nuclear Data*, pages 7–13. JAEA-Tokai (Japan), 2006.
- [21] G. Aliberti, G. Palmiotti, M. Salvatores, T. K. Kim, T. A. Taiwo, M. Anitescu, I. Kodeli, E. Sartori, J. C. Bosq, and J. Tommasi. Nuclear data sensitivity, uncertainty and target accuracy assessment for future nuclear systems. *Ann. of Nucl. Energy*, 33(8):700–733, 2006.
- [22] H. Pomerance. Absorption cross sections for long-lived fission- product zr93, am241, and enriched stable platinum isotopes. In *Physics Division Semianual Progress Report*, pages 50–55. ORNL, 1955.
- [23] M. A. Bak, A. S. Krivohatskiy, K. A. Petrzhak, and E. A. Romanov, Ju. F. And Shljamin. Cross sections and resonance integrals of capture and fission of long-lived isotopes of americium. *Atomic Energy*, 23:316, 1967.

- [24] A. G. Dovbenko, V. I. Ivanov, V. E. Kolesov, and V. A. Tolstikov. Am-241 radiative neutron capture. *Report Obninsk Russia*, (6):42, 1969.
- [25] R.M. Harbour, K.W. Mac Murdo, and F.J. Mc Crosson. Thermal-neutron capture cross sections and capture resonance integrals of americium-241. *Nucl. Sci. Eng.*, 50:364, 1973.
- [26] V. D. Gavrillov, V. A. Goncharov, V. V. Ivanenko, V. P. Smirnov, and V. N. Kustov. Thermal fission and capture cross-sections and resonance integrals for Am-241, Am-243, Bk-249, Cf-249. *Atomic Energy*, 41:185, 1976.
- [27] J. V. Adamchuk. *Nuclear Science and Engineering*, 61:356, 1976.
- [28] T. S. Belanova, A. G. Kolesov, V. A. Poruchikov, G. A. Timofeev, S. M. Kalebin, V. S. Artamonov, and R. N. Ivanov. *Atomic Energy*, 38:29, 1975.
- [29] K. Wisshak, J. Wickenhauser, F. Kappeler, G. Reffo, and F. Fabbri. The isomeric ratio in thermal and fast-neutron capture of am-241. *Nucl. Sci. Eng.*, 81(3):396–417, 1982.
- [30] N. Shinohara, Y. Hatsukawa, K. Hata, and N. Kohno. Radiochemical determination of neutron capture cross section of 241-am. *J. Nucl. Sci. Technol.*, 34:613, 1997.
- [31] N. L. Maidana, M. S. Dias, and M. F. Koskinas. Measurement of the thermal neutron capture cross section and resonance integral of Am-241. *Radiochimica Acta*, 89:419–423, 2001.
- [32] Shoji Nakamura, Masayuki Ohta, Hideo Harada, Toshiyuki Fujii, and Yamana Hajimu. Thermal-neutron capture cross section and resonance integral of americium-241. *Nuclear Science and Technology*, 44:1500–1508, 2007.
- [33] Bringer et al. In *Int. Conf. on Nuclear Data for Science and Technology*, Nice, 2007.
- [34] T. Belgya, L. Szentmiklosi, Z. Kis, N .M. Nagy, and J. Konya. Measurement of 241am ground state radiative neutron capture cross section with cold neutron beam. Technical report, 2012.
- [35] Genreith et al. Nuclear data 2013 conference. 2013.
- [36] M. Jandel, T.A. Bredeweg, E.M. Bond, M.B. Chadwick, R.R. Clement, et al. Neutron capture cross section of Am-241. *Phys. Rev. C*, 78:034609, 2008.
- [37] C. Lampoudis et al. *European Physical Journal A: Hadrons and Nuclei*, 2013.

- [38] H. Derrien and B. Lucas. In *Conf. on Nucl. Cross-Sect. and Techn., Washington*, volume 2, page 637, 1975.
- [39] S. M. Kalebin et al. *Atomic Energy*, 40:303, 1976.
- [40] K. Shibata, O. Iwamoto, T. Nakagawa, N. Iwamoto, A. Ichihara, S. Kunieda, S. Chiba, K. Furutaka, N. Otuka, T. Ohsawa, T. Murata, H. Matsunobu, A. Zukeran, S. Kamada, and J. Katakura. JENDL-4.0: A new library for nuclear science and engineering. *J. Nucl. Sci. Technol.*, 48:1 – 30, 2011.
- [41] A. J. Koning, E. Bauge, C. J. Dean, E. Dupont, U. Fischer, R. A. Forrest, R. Jacqmin, H. Leeb, M. A. Kellett, R. W. Mills, C. Nordborg, M. Pescarini, Y. Rugama, and P. Rullhusen. Status of the JEFF Nuclear Data Library. *J. Kor. Phys. Soc.*, 59(2, Part 3, SI):1057–1062, 2011.
- [42] G. Vanpraet, E. Cornelis, S. Raman, and G. Rohr. Neutron capture measurements on ^{241}Am . *Radiation Effects*, 93:157–62, 1986.
- [43] L. W. Weston and J. H. Todd. Neutron Absorption Cross-Section Of Am-241. *Nucl. Sci. Eng.*, 61(3):356–365, 1976.
- [44] C. Lampoudis, S. Kopecky, A. Plompen, P. Schillebeeckx, P. Siegler, F. Gunsing, C. Sage, and O. Bouland. Transmission and capture measurements for ^{241}Am at GELINA. *J. Kor. Phys. Soc.*, 59(2):1785–1788, 2011.
- [45] A. Messiah. *Quantum mechanics*. Dover publications, 1999.
- [46] G.R. Satchler. *Direct nuclear reactions*. Clarendon Press-Oxford, Oxford university press, New York, 1983.
- [47] H. Feshbach. *Theoretical nuclear physics*. Wiley interscience publication, 1992.
- [48] A. Volya and V. Zelevinski. Continuum shell model. *Phys. Rev. C*, 74(064314), 2006.
- [49] A. Volya. Time dependent approach to the continuum shell model. *Phys. Rev. C*, 79(044308), 2009.
- [50] J.P. Mitchell et al. Low lying states in 8B. 2009. arXiv [nucl-ex].
- [51] P.L. Kapur and R.E. Peierls. *Proc. Royal Soc. London*, A166(277), 1938.
- [52] E.P. Wigner and L. Eisenbud. *Phys. Rev.*, 72(29), 1947.
- [53] A.M. Lane and R.G. Thomas. *Rev. Mod. Phys.*, 30(2), 1958.

- [54] J.E. Lynn. *The theory of neutron resonance reactions*. Clarendon press, Oxford, 1968.
- [55] Nuclear energy agency. *JEFF report 18: Evaluation and analysis of nuclear resonance data*. OECD data bank.
- [56] P. Descouvemont and D. Baye. The R matrix theory. *Rep. Prog. Phys.*, 73(036301), 2010.
- [57] C.E. Porter and R.G. Thomas. Fluctuation of nuclear reaction widths. *Phys. Rev.*, 104(2), 1956.
- [58] T.A. Brody, J. Flores, J.B. French, P.A. Mello, A. Pandey, and S.S.M. Wong. Random matrix physics: spectrum and strenght fluctuations. *Rev. Mod. Phys.*, 53(3), 1981.
- [59] H.A. Weidenmuller and G.E. Mitchell. Random matrices and chaos in nuclear physics: Nuclear structure. *Rev. Mod. Phys.*, 81, 2009.
- [60] C.E. Porter. *Statistical theories of spectra : fluctuations*. New York academic press, 1965.
- [61] The n_TOF collaboration. Cern n tof facility : performance report, cern-sl-2002-053 ect. Technical report, CERN, 2003.
- [62] C. Guerrero et al. *European Physical Journal A: Hadrons and Nuclei*, 49(27), 2013.
- [63] F. Carminati, C. Gelès, R. Klapisch, J.P. Revol, Ch. Roche, J.A. Rubio, and C. Rubbia. An energy amplifier for cleaner and inexhaustible nuclear energy production driven by a particle beam accelerator. Technical report, CERN/AT/93-47 (ET), 1993.
- [64] The TARC collaboration. Neutron-driven nuclear transmutation by adiabatic resonance crossing. Technical Report EUR 19117 EN, European commision - Nuclear science and technology, 1999.
- [65] J. Pancin. *Detecteur de Neutrons avec un Detecteur de Type Micromegas: de la Physique Nucleaire à l'Imagerie*. PhD thesis, Universite Bordeaux I, 2004.
- [66] S. Marrone, P.F. Mastinu, U. Abbondanno, R. Baccomi, E.Boscolo Marchi, N. Bustreo, N. Colonna, F. Gramegna, M. Loriggiola, S. Marigo, P.M. Milazzo, C. Moreau, M. Sacchetti, G. Tagliente, R. Terlizzi, G. Vannini, G. Aerts, E. Berthomieux, D. Cano-Ott, P. Cennini, C. Domingo-Pardo, L. Ferrant, E. Gonzalez-Romero, F. Gunsing, M. Heil, F. Kaepfeler, T. Papaevangelou, C. Paradela, P. Pavlopoulos, L. Perrot, R. Plag, J.L. Tain, and H. Wendler.

- A low background neutron flux monitor for the n_tof facility at cern. *Nuclear Instruments and Methods in Physics Research Section A: Accelerators, Spectrometers, Detectors and Associated Equipment*, 517(1 - 3):389 – 398, 2004.
- [67] C. Guerrero, U. Abbondanno, G. Aerts, H. Alvarez, F. Alvarez-Velarde, et al. The n_TOF Total Absorption Calorimeter for neutron capture measurements at CERN. *Nucl.Instrum.Meth.*, A608:424–433, 2009.
- [68] U. Abbondanno et al. The data acquisition system of the neutron time-of-flight facility n_tof at cern. *Nuclear Instruments & Methods in Physics Research, Section A: Accelerators, Spectrometers, Detectors, and Associated Equipment*, 538:692–702, 2005.
- [69] J. F. Briesmeister. *MCNP - a general Monte Carlo n-particle transport code*, volume LA-13709-M. 2000.
- [70] A. Ferrari et al. *Fluka: a multi-particle transport code*. CERN, 2011.
- [71] N. M. Larson. *Updated users' guide for SAMMY: multilevel R-matrix fits to neutron data using Bayes' equations.*, 2008.
- [72] H. Tagziria, J. Bagi, B. Pedersen, and P. Schillebeeckx. Absolute determination of small samples of pu and am by calorimetry. *Nucl. Instrum. Meth. A*, 691(0):90 – 96, 2012.
- [73] C. Guerrero. Safety manual for special use of a radioactive source : ^{241}Am at the cern n_TOF facility - 4386rp - ^{241}Am (3.8 GBq). Technical Report EDMS 1085674, n_TOF, CERN, 2010.
- [74] C. Sage, V. Semkova, O. Bouland, P. Dessagne, A. Fernandez, et al. High resolution measurements of the Am-241 (n,2n) reaction cross section. *Phys. Rev. C*, 81:064604, 2010.
- [75] A. Krasa and A. Plompen. *JRC-IRMM Technical Note Eur 24818*, 2011.
- [76] The n_TOF collaboration. Summary of ^{241}Am capture cross section with C_6D_6 detectors. Technical Report CERN-INTC-2009-025 INTC-P-269, CERN, 2010.
- [77] C. Massimi et al. *Journal of the Korean physical society*, 59(2):1689–1692, August 2011.
- [78] A. D. Carlson et al. International evaluation of neutron cross section standards. *Nuclear Data Sheets*, 110:3215–3224, 2009.
- [79] M. Barbagallo et al. High-accuracy determination of the neutron flux at n_tof. *European Physical Journal A: Hadrons and Nuclei (submitted)*, 2013.

- [80] L. M. Bollinger and G. E. Thomas. P-wave resonances of U238. *Phys. Rev.*, 171(4):1293, 1968.
- [81] M. Gyulassy et al. Report no. ucrl-50400, vol. 11. Technical report, 1972.
- [82] S. F. Mughabghab. *Atlas of Neutron Resonances and Thermal Cross Sections. Resonance Parameters and Thermal Cross Sections. Z=1-100*. Elsevier Publishing Company, 2006.
- [83] F.H. Fröhner. *SESH computer code, Report No. GA-8380*, 1968.

Résumé

Dans le contexte de la technologie nucléaire actuelle, la radiotoxicité du combustible usé est dominée par les actinides mineurs pour les temps caractéristiques dépassant 10^4 années. L'isotope ^{241}Am , en particulier, avec sa demi-vie de 432 ans, représente typiquement la moitié du contenu en actinides mineurs d'un combustible usé de réacteur REP. Ce travail de doctorat a consisté en la mesure et l'analyse de la section efficace $^{241}\text{Am}(n,\gamma)$ auprès de la collaboration n_TOF, au CERN. Après sélection des évènements exclusivement acquis en présence d'un blindage de plomb devant les détecteurs C_6D_6 , la calibration amplitude-énergie dut être ajustée avec le temps, en utilisant un photon issu de la réaction $^{27}\text{Al}(\alpha,p)^{30}\text{Si}^*$. L'extraction des histogrammes incluait l'application d'une fonction poids obtenue par simulation MCNP, une correction de temps mort, une calibration temps de vol-énergie, et une normalisation à l'énergie d'excitation du noyau composé. Après soustraction du bruit de fond, Les spectres furent normalisés relativement à la résonance à 4.9 eV de l' ^{197}Au . Enfin, l'analyse des résonances fut exécutée avec le code SAMMY. La valeur thermique extraite est de 678 ± 68 barns, l'incertitude étant avant tout liée au niveau de bruit de fond trop important. La région résolue fut étendue de 150 eV à 320 eV, pour un total de 192 résonances ajoutées ou fortement modifiées. La région non résolue fut analysée jusqu'à 150 keV, avec une section efficace moyenne plus grande que les précédentes évaluations en dessous de 20 keV.

Summary

In the context of the current nuclear technology, the radiotoxicity of the spent fuel of a typical PWR reactor is dominated by minor actinides for times greater than 10^4 years. In particular, ^{241}Am and its 432 years half-life is responsible for about half of the minor actinide content of a PWR spent fuel. This thesis work consisted in measuring and analysing the $^{241}\text{Am}(n,\gamma)$ cross section at the CERN n_TOF facility. After selecting exclusively the events obtained with lead shielding in front of the C_6D_6 detectors, the amplitude-energy calibration has to be adjusted with time, by using a photon coming from the $^{27}\text{Al}(\alpha,p)^{30}\text{Si}^*$ reaction. Histogram extraction included applying a weighting function (obtained by MCNP simulation), a dead time correction, and a normalization to the compound nucleus excitation energy. The background corrected spectra were normalized relatively to the 4.9 eV resonance on ^{197}Au . Finally, the resonance analysis was performed using the SAMMY code. The extracted thermal value is 678 ± 68 barns, the uncertainty being mostly due to the large background level. The resolved range was extended from 150 eV to 320 eV, with a total of 192 resonances that had to be added or heavily modified. The unresolved region was analysed up to 150 keV, yielding a larger average cross section than previously evaluated below 20 keV.